Understanding Complex Ordering
In
Transition Metal Oxides

Thesis submitted to

WEST BENGAL UNIVERSITY OF TECHNOLOGY

in partial fulfillment of the Degree of

DOCTORATE OF PHILOSOPHY

2013

Abhinav Kumar

School of Management and Sciences,
West Bengal University of Technology
Salt Lake, Kolkata-700098
West Bengal, India

Thesis Certificate

This is to certify that the thesis entitled "**Understanding Complex Ordering in Transition Metal Oxides**", submitted by **Abhinav Kumar** to the West Bengal University of Technology for the award of the degree of Philosophy, is a bona fide record of the research work done by him under my supervision in the duration of five and half years from August 2007 to January 2013. He has completed the work truthfully and successfully to the best of my knowledge. The contents of this thesis, in full or in part have not been submitted to any other Institute or University for the award of any degree or diploma.

Priya Mahadevan(Supervisor)

Associate Professor

Department of Condensed Matter Physics and Material Sciences

S.N. Bose National Centre for Basic Sciences

JD block, Sector-3, Salt Lake

Kolkata-700098

Dedicated to

My parents
who created me

Acknowledgments

Abhinav Kumar
S.N.Bose National Center for Basic Sciences,
Kolkata, India.

List of Publications

1. Charge ordering induced ferromagnetic insulator: $K_2Cr_8O_{16}$
   P. Mahadevan, Abhinav Kumar, D. Choudhury and D. D. Sarma
   Phys. Rev. Lett. 104, 256401 (2010).

2. Strong correlations and a weak-coupling gap across ferromagnetic-metal to ferromagnetic-insulator transition in $K_2Cr_8O_{16}$
   P. A. Bhobe, A. Chainani, R. Eguchi, M. Matsunami, Abhinav Kumar, P.Mahadevan,D. D. Sarma et. al.
   (Under preparation) .

3. Microscopic model for charge ordering in $K_2Cr_8O_{16}$
   Abhinav Kumar, A. K. Nandy and P. Mahadevan.
   (Under preparation).

4. Magnetism in $K_2Cr_8O_{16}$
   A. K. Nandy, Abhinav Kumar and P. Mahadevan and D.D. Sarma
   (Under preparation).

5. Origin of ferromagnetic insulating state in Cr doped VO_2
   Abhinav Kumar and P. Mahadevan
   (Under preparation).

6. Is Bi_2NiMnO_6 a multiferroic ?
   Abhinav Kumar and P. Mahadevan
   (Under preparation).

7. A model for ferroelectricity in $BaTiO_3$
   Abhinav Kumar, H. K. Chandra and P.Mahadevan
   (Under preparation).

8. Effect of quantum confinment on the conduction band minimum of semiconductors
   : Cherian Roby, Abhinav Kumar and P. Mahadevan
   Journal of Nanoscience and Nanotechnology Vol-9, 5673-5675 (2009)

Contents

List of Figures

List of Tables

Chapter 1

Introduction

1.1 Electronic structure of Transition Metal Oxides

Transition metal oxides are the building blocks of the technology of recent times. Remarkable development in the growth and characterization techniques have put transition metal oxides at par with the semiconductors, which are known for their technological application for a long time. A notable characteristic of transition metal oxides(TMO) is the enormous range of electronic properties. It can be a good insulator(TiO_2), a semiconductor($Fe_{0.9}O$), a metal(ReO_3) and a superconductor ($YBa_2Cu_3O_7$). Not only that, few TMO show a metal to insulator transitions with temperature(VO_2), pressure(V_2O_3) or composition(Na_xWO_3). Apart from electronic properties TMO have a wide range of other physical properties related to their optical and magnetic properties which form the basis of many other applications. Their magnetic properties varies from ferromagnetism($SrRuO_3$, $Sr_4Co_3ReO_{12}$ [1]) to antiferromagnetism(NiO) to ferrimagnetism(La_2NiMnO_6) to paramagnetism ($SrRhO_3$ [2]) to diamagnetism. The wide ranging chemical and physical properties of these compounds are a consequence of the strongly coupled spin, charge and orbital degree of freedom in these oxides. The wide range of properties make them candidates for the device application such as magnetic storage, magnetic reading, flat panel displays, fuel cells and many more. This also makes it difficult as well as interesting to understand the physics involved behind these properties in TMO.

The insulating state found in transition metal oxides could have several origins. Coulomb correlation effects at the transition metal site could localize the electrons and in some systems are responsible for the insulating state. These systems are classified as Mott-Hubbard insulators. Transition metal oxides have another scale which is the charge transfer energy that reduces to the bare onsite energy difference between the transition metal d states and the oxygen states. This becomes the dominant scale when the coulomb interaction strength is very large and could also result in the insulating state. These insulators are termed charge transfer insulators. In the presence of disorder one has another origin for the insulating state. These are termed as Anderson localization induced insulators.

The wealth of phenomena in these materials has driven the studies over the decades. A larger part of studies are about how to control and tune these properties. For example the manganites [3, 4], are examples which show a huge change in the resistivity with applied magnetic field for certain doping compositions, the phenomena called colossal magnetoresistive effect. There are other examples where a phase transition is engineered by an electric field or a magnetic field. The reason behind these transitions is that the 3d transition oxides comprise a set of systems where the spin, orbital and lattice degrees of freedom [5–9] works in a very competing and small energy scale, resulting in a phase diagram where sometimes a small change in the interaction strengths leads us to a completely different phase with entirely different properties.

To understand the electronic structure and various properties and phenomena in various TMO it is important to understand the main electronic interactions which are responsible for their remarkable properties, and how they get modified. Apart from the hopping interaction strengths which is responsible for the band width, W, the important parameters determining the electronic properties of TMO are the coulomb correlation strength U between two d electrons on the same atom and the charge transfer energy Δ defined as energy difference between the oxygen ion and the transition metal ion. This was put on a firm footing in the classic work by Zaanen, Sawatzky and Allen [10]. The Zaanen-Sawatzky-Allen plot has been shown in Fig.1.1 which shows the different phases depending upon the doping concentration and temperature for 3d transition metal oxides.

To understand and predict the behavior of electrons at a microscopic level in TMO is very important
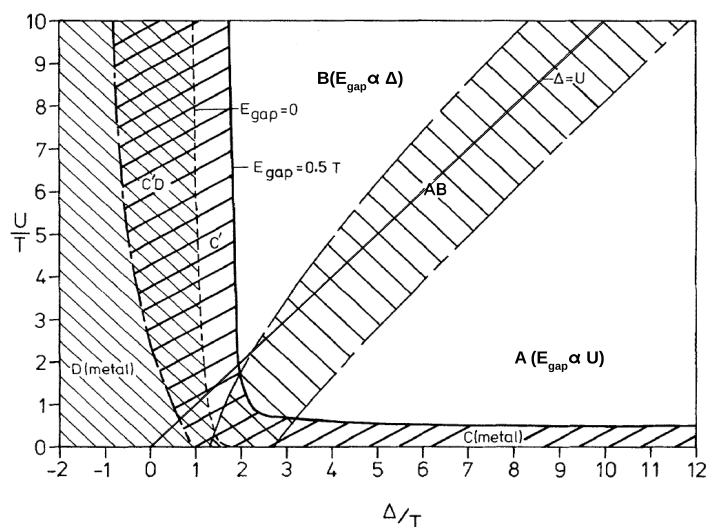
Figure 1.1 Zaanen-Sawatzky-Allen plot for classifying $3d$ transition metal compounds. The straight line U/Δ separates the Mott-Hubbard regime(A) and charge-transfer regime(B). Fig Ref: Zaanen, Sawatzky,Allen Phys. Rev. Lett. 55, 418(1985).

for both physicists and chemists. With the on going development of theoretical methods and the modern advances in computational facilities, computational material science has emerged as one of the foremost and very fertile research domain over the years.

1.2 Structural aspects of Transition Metal Oxides

When one is talking of the structure various aspects come to one's mind which includes the crystal structure and the various details such as the position, the bondlengths, the bond angles and so on. Usually, the local environment like bond lengths, bond angles, coordination numbers and local bonding control the structural stability. Transition metal oxides occur in various structures and there is strong correlation between the crystal structure and the observed properties. The interactions between nearest neighbors have the most important effects on electronic properties. Specially, the way metal and oxygen connected and make a unit like octahedra and how these units connected to each other. It could be a network of corner shared or edge shared octahedra which has important influence on electronic proper-

ties. Usually, edge sharing octahedra bring the metal closer to each other resulting in strong interactions between the metal ions. This is seen in rutile VO_2 where there are two types of octahedral connection. There is evidence of strong interaction along c-direction due to edge-sharing of octahedra. Distortions, defects or substitution introduces additional dimensions in the electronic properties of transition metal oxides. Like in VO_2, structural distortions have a significant role in metal to insulator transitions [11].

In all these structure types, the perovskite family is the most studied one. The interest in compounds belonging to this family of crystal structure arise due to its variety of properties and phenomena. The flexibility for chemical and structural manipulation in these compounds leads to various application in controlled way. Magnetism and orbital physics of various kinds are observed in these perovskites. It shows a rich phase diagram depending upon non-stochiometry and tilting or distortion of BO_6 octahedras which are connected via corner sharing oxygens. Order-disorder, charge doping and charge/orbitals inhomogeneity leads to a colossal response [12].

Work by Goldschmidt *et. al.*, on the structural details of perovskites, is the basis for further exploration of the perovskite family of compounds [13, 14]. Various distortions in these compounds and how they modify the magnetic and electric properties helped physicists and chemists to understand various mechanisms. In the next section, we will see the structural details and the mechanism of various kind of distortions in these compounds.

1.3 Perovskite structure

The general chemical formula for oxides belonging to the perovskite family is ABO_3. Usually, A sites are occupied by rare earth or alkali metals and B sites by Transition metals. The structure can be described in two ways. First, a cubic structure with A at the corners, B at body center positions and O at the face center positions as shown in Fig. 1.2a or alternatively as a cubic structure with A at body centered positions, B at corners and O at centre of edges of cube as shown in Fig. 1.2b.
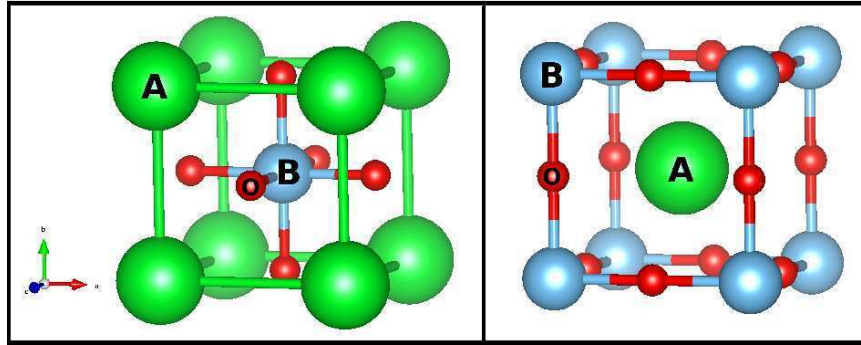
Figure 1.2 Two different types unit cells to understand Perovskite structure.

The two most common distortions in the perovskite family of compounds are rotations of the MO_6 octahedra which is known as $GdFeO_3$ type of distortion and the Jahn-Teller distortion.

1.3.1 GdFeO$_3$ distortion in perovskites

The most common distortions in this class of compounds are the tilts or rotation of the MO_6 octahedra around one or more axis. This happens when a smaller cation is placed at the position of A. For the ideal undistorted cubic structure, the ionic radii (r_A, r_B, r_O) related by the equation,

$a = \sqrt{2}(r_A + r_O) = 2(r_B + r_O)$

The smaller A ion reduces the lattice constant 'a' which reduce the B-O distance resulting in a rotation of the BO_6 octahedra and elongation of B-O bondlength as shown in Fig. 1.3. Goldschmidt [14] introduced a tolerance factor(t), defined by the equation

$$t = \frac{(r_A + r_O)}{\sqrt{2}(r_B + r_O)} \tag{1.1}$$

Although, for an ideal cubic perovskite structure 't' is unity, the cubic structure is also found for lower t-values $(0.85 < t < 1.0)$. In most cases, different distortions of the perovskite structure appear which deviate from cubic structure. The compound $CaTiO_3$ was originally thought to be cubic, but later, it was found that it is orthorhombic [15]. Lower values of t will lower the symmetry of the crystal structure. For example the compound $GdFeO_3$ with t = 0.81 is orthorhombic (r_A = 1.107 Å and r_B =

0.78 Å). As rotation or tilt of a octahedra restricts the allowed rotation or tilt of the other octahedra. Only 23 tilt systems have been found which belong to 15 unique space groups [16].
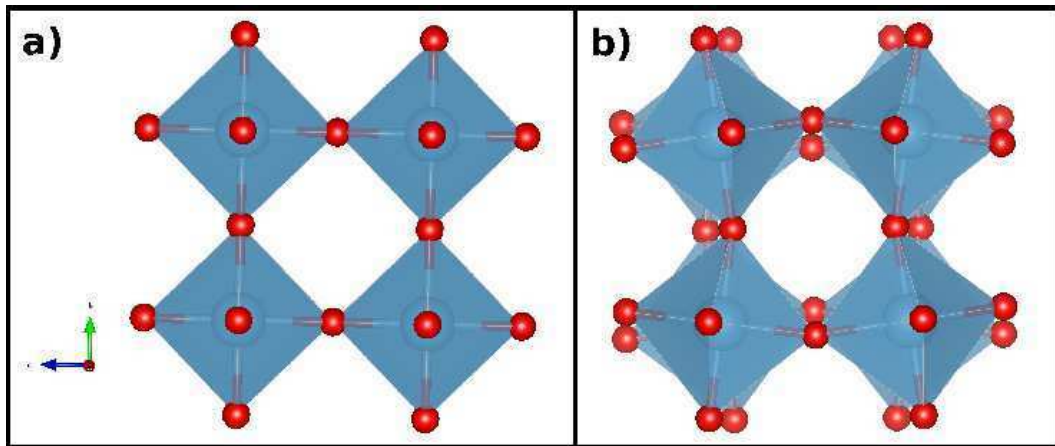
Figure 1.3 BO_6 octahedra in a) ideal cubic unit cell and b) in distorted unit cell with tilts and rotation of the octahedra.

Another kind of distortion in the perovskite structures is Jahn-Teller distortion which we will understand with help of crystal field model.

1.4   Crystal field theory

The crystal-field theory(CFT) [17] is a simple model to capture the effect of electrostatic potential on the energies of the d orbitals of a metal ion due to its environment. Usually this potential is the result of neighboring negative charges surrounding the metal ion. This is a semi-classical model in which we consider the neighboring ions as point charge and the electrons on the transition metal ion present in the center as a quantum mechanical object. In a spherically symmetric ligand environment, energies of all five d orbitals will be equal. However, in a real compounds, the surrounding negative charges are never spherically distributed. As the effect of point charges surrounding the transition metal ion the energy of orbitals increases due to repulsive force on orbitals. But, the increase in the energy of the particular orbital depends upon the orientation of that orbitals and also the orientation of ligand ions. This is the basis of crystal field model. For a isolated transition metal atom the five d orbitals are degenerate in

energy.
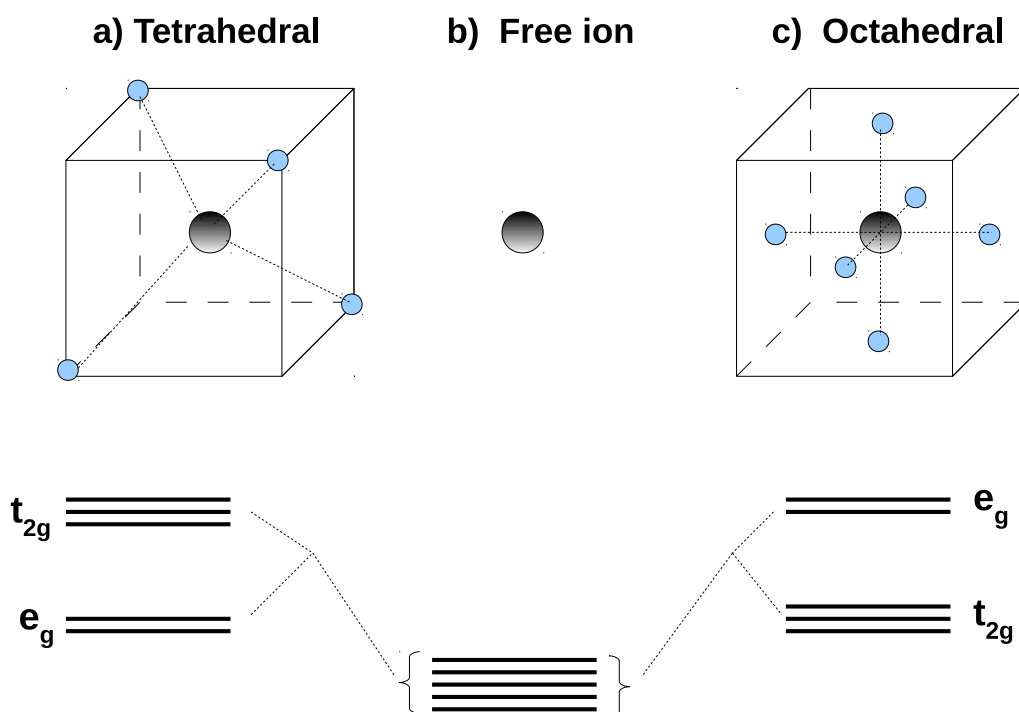
Figure 1.4 Schematic representation of the splitting pattern of d orbitals under various crystal-field symmetries tetrahedral, for free ion, for octahedral respectively.

The pattern of splitting is governed by the local geometry of the point charges(ligands). We show the level diagram for a few very common environments found in transition metal oxides in Fig. 1.4. In an octahedral symmetry, the d_{xy}, d_{yz} and d_{xz} orbitals are not pointing towards the point charges on ligands. They feel less repulsion compared to the $d_{x^2-y^2}$ and $d_{3z^2-r^2}$ orbitals which are pointing towards the point charges. Due to this energy of $d_{x^2-y^2}$ and $d_{3z^2-r^2}$ orbitals goes higher than that of d_{xy}, d_{yz} and d_{xz} orbitals. This results into splitting of d orbitals into two sets : three fold degenerate t_{2g} symmetry levels, found to be lower in energy and the doubly degenerate e_g levels that lie higher in energy (Fig. 1.4(c)). However, in a tetrahedral symmetry in Fig. 1.4(a), such an ordering will be reversed to a lower energy for the orbitals with e symmetry and a high energy for those d orbitals with

t_2 symmetry as now d_{xy}, d_{yz} and d_{xz} orbitals pointing toward the ligands.

In a simple CFT, we do not consider the effect of hopping. However, in real materials, the above point charge model yields unsatisfactory results for the degeneracy pattern for d orbitals, suggesting the corrections beyond the point-charge approximation are required. The more sophisticated model, to describe the effect of ligands is known as ligand field theory. Apart from the ligand field theory the electron-electron correlations and the Hund's exchange splitting between up and down spin channels also play an important role to determine the electronic structure of Transition metal compounds. So, in a d^n configuration, one may have two limiting cases, strong or weak crystal field. In a weak crystal-field limit($U > \Delta$), putting electrons in same orbital costs more energy. So, the system likes to go in high spin configuration like in the perovskite $LaMnO_3$ [18, 19]. It is an example of weak crystal-field limit. Here Mn^{3+} ($3d^4$) ion has the electronic configuration t_{2g}^3, e_g^1, In strong crystal field limit($\Delta > U$), low spin configuration is energetically more favorable. $SrRuO_3$ is an example [20] of strong crystal-field limit ($\Delta > U$) where Ru^{4+} ($4d^4$) ion prefers t_{2g}^4, e_g^0 electronic configuration over t_{2g}^3, e_g^1 .

1.4.1   Jahn-Teller Distortion

The Jahn-Teller theorem [21], named after Hermann Arthur Jahn and Edward Teller, states that degeneracy makes the symmetric configuration unstable, gives rise to a strong coupling between electron and phonon resulting in a structural distortion which lowers the symmetry of the crystal. The simplest example of the Jahn-Teller theorem can be seen for octahedral systems where it further introduces a splitting in levels of t_{2g} and e_g symmetry. A classic example of Jahn-Teller effect in a material is, $LaMnO_3$ [19]), a system with $3d^4$ or $t_{2g}^3 e_g^1$ electronic configuration. The electronically degenerate state with an electron in one of the e_g orbitals leads to lower its symmetry via structural distortions.

There are two types of distortion, represented by two vibrational modes, orthorhombic Q_2 mode (Fig. 1.5(a)) and tetragonal Q_3 mode (Fig. 1.5(b)). These lower the structural symmetry, resulting in a degeneracy lifting of the highest occupied e_g orbitals. For the experimentally observed Jahn-Teller distortion, the Q_3 mode is dominant over the Q_2 mode as it brings more stabilization in the energy of the $d_{3z^2-r^2}$ orbital than the $d_{x^2-y^2}$ (Fig. 1.5(c)). We can find the same effect for the electronically degenerate
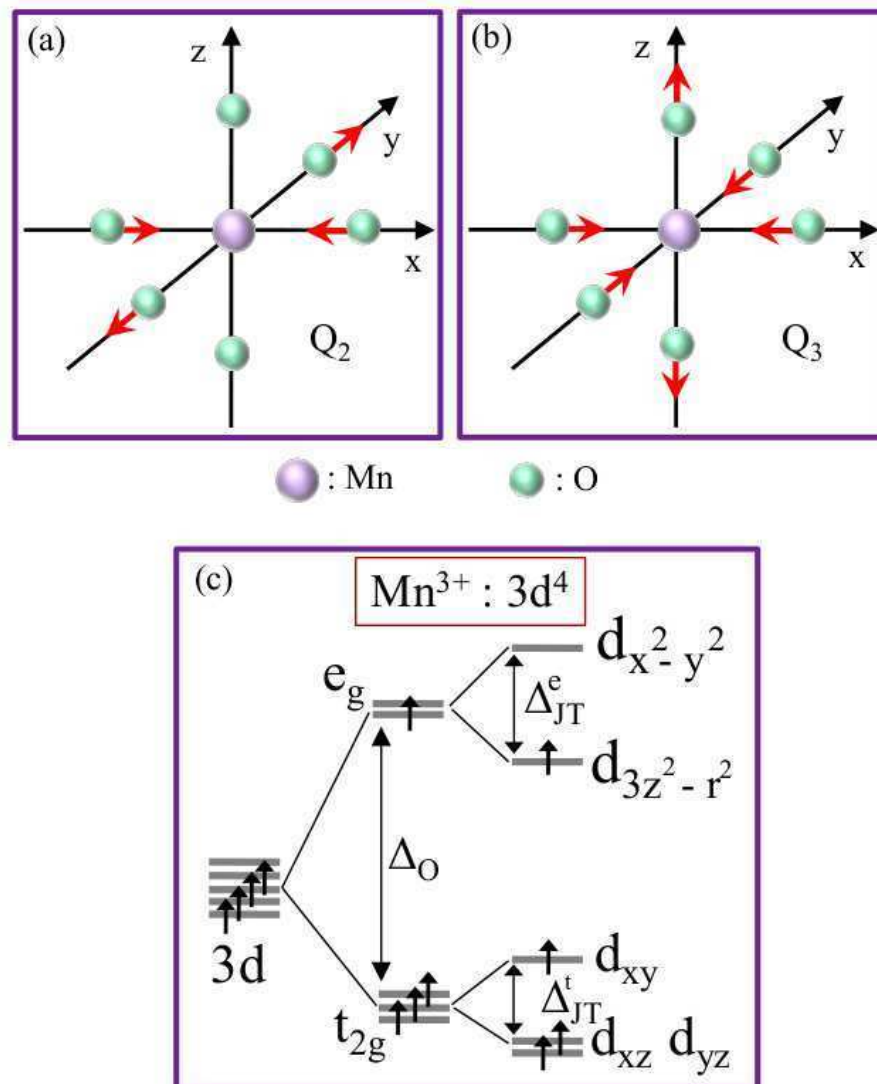
Figure 1.5 (a) and (b), schematically represent the vibrational modes, Q_2 and Q_3, respectively for an example of perovskite, $LaMnO_3$, while (c) describes the resultant Jahn-Teller splitting in the t_{2g} and e_g manifolds.

t_{2g} systems for example, in the electronic configuration $3d^1$ ($3t_{2g}^1$) in perovskites. however, the three-fold degenerate t_{2g} orbitals form relatively weaker π bonds, therefore these compounds are relatively less Jahn-Teller active. Weak Jahn-Teller active examples are Ti^{3+} ion in $LaTiO_3$ ($t_{2g}^1 e_g^0$) [22], V^{3+} ion in $LaVO_3$ ($t_{2g}^2 e_g^0$) [23], the configurations with partially filled t_{2g} levels are examples of weak Jahn-Teller active. ; the strong Jahn-Teller active configurations are partially filled e_g levels as $t_{2g}^3 e_g^1$ (Mn^{3+}

in LaMnO$_3$) [19] and t$_{2g}^6$e$_g^3$ (Cu^{2+} in KCuF$_3$) [24]; the configurations with half-filled or completely filled t$_{2g}$ and e$_g$ levels are Jahn-Teller inactive configurations as t$_{2g}^3$e$_g^0$, t$_{2g}^3$e$_g^2$, t$_{2g}^6$e$_g^0$, t$_{2g}^6$e$_g^4$.

1.5 Magnetism:

In popular terms magnetism is a force of attraction or repulsion. A magnet attract iron pieces. In more scientific language magnetism is the response of a material in external magnetic field. The first known magnet is 'lodestone' [25]. Before this magnets were used by Shusrut, a indian for surgical purpose [26]. It was also used for navigation purpose [27]by ancient Chinese. Afterward, people became more curious in search of magnetic materials and began to use them in their daily life.

Before moving to the various aspects of magnetism in materials, we will first discuss the source of magnetism in atoms/ions.

1.6 Magnetic Moments in Atoms/Ions

The fundamental quantity in magnetism is the magnetic moment. Magnetic moment can emerges in two ways, first, mobile electric charges which were characterized by the Maxwell's equations [28, 29] while the second emerged from the the electron spin [30–33], a pure quantum-mechanical object. The source of magnetic moment in atom or ion is the intrinsic spin of the unpaired electrons. Each atom can have two electrons with opposite intrinsic spins and having same remaining quantum numbers. The paired electrons do not contribute in the magnetic moment of ions or atoms.

We can associate a intrinsic magnetic moment with an electron in a atom [34] having the spin $\vec{s}$

$$\vec{\mu}_s = -g\mu_B\vec{s}, \tag{1.2}$$

where $\mu_B = \frac{eh}{4\pi mc}$, is known as Bohr magneton. Here, e and m are the charge and the mass of an electron respectively, c is the velocity of light and h is the Planck's constant. g is usually called the Landé g-factor, the magnitude for free electrons is 2.0. The negative sign represents the negative charge of an electron. But when we come to many electron systems or atoms, the coupling between the moments of

the unpaired electrons determines the coupling and hence the magnetic moment in the system. The two main factors to govern the coupling are coulomb repulsion between the electrons following the Pauli's exclusion principle and the spin-orbit coupling of two magnetic moments of electron orbital magnetic moment $\vec{L}$ and spin magnetic moment $\vec{S}$.

The effect of these referred to as the Hund's rules are given below.

1) The ground state of isolated ion or atom should have largest value of total spin S

2) The ground state of isolated ion or atom should have largest value of orbital angular momentum L which is permitted by first rule

3) The total angular momentum J is |L-S| for less than half-filled shells, and L+S for more than half-filled shell.

If we consider electrons with the same principle and azimuthal quantum numbers, *e.g.* 3*d* electrons, kinetic energy as well as potential energy of all electrons will be same, thus the only energy which governs the ground state is electron-electron repulsion. The largest value of spin, S corresponds to parallel spins of electrons and this results as a consequence of the Pauli exclusion principle. It can also be explained by exchange-hole effect [35, 36] which says parallel spin electrons avoid each other more effectively due to the antisymmetric nature of the spatial part of their wavefunction.

The electron in an atom may have an orbital magnetic moment

$$\vec{\mu}_o = -\frac{e}{2mc}(\vec{r} \times \vec{p}) = -\frac{e}{2mc}\vec{l},$$ (1.3)

where $\vec{r}$, $\vec{p}$ and $\vec{l}$ are position, momentum and angular momentum vector per electron respectively, arising from the orbital motion in atoms. This orbital moment contributes in the explanation of Hund's second and third rule. Atoms may have several terms with maximum spin. Once, it is determined how the spins are assigned, the second Hund's rule states that the lowest energy state has the largest total orbital momentum, which can be viewed as electrons revolving in same direction and so, spatial distance between them will be more which leads to minimum repulsion. The third Hund's rule, which, however, is not related with the electron-electron repulsion but with the coupling between spin ($\vec{S}$) and orbital ($\vec{L}$). Within L-S coupling, the atomic moments become eigenstates of the total angular moment

$\vec{J} = \vec{L} + \vec{S}$. The third rule asserts, unless the shell is exactly half-filled where L = 0 and J = S, the term with smallest J will be the lowest energy when the shell is less than half-filled while the largest J will be the lowest when the shell is more than half-filled.

The first two rules are almost always true but the third law is a weak law and only applicable in certain circumstances. The order of the three rules reflects also as a hierarchy of energy scales. The first rule is guaranteed by energy and is as large as 1eV. The second is the energy range by 0.1 - 0.3eV. The third energy scale is very weak and presence of the other scales results in Hund's third law being disobeyed.

1.7   Magnetism in Solid

When atoms or ions form solids, the magnetism is defined as the long range ordering of magnetic moments of individual ions. They can order parallel(ferromagnetic) resulting in a net magnetic moment, anti-parallel(antiferromagnetic) leading to zero net magnetic moment or in a random orientation(paramagnetic) which is usually, a high temperature state having no net magnetic moment. This ordering can be modified by external parameters like temperature, magnetic field, pressure etc. Ferromagnetic materials have not only a large magnetization, but also retain its magnetization even after the removal of the external field. A few examples are Iron, Cobalt, Nickel etc.

The ordering between the two magnetic moments in a solid must be determined by the interactions between them. As magnetic moments can be treated as magnetic dipoles the very first interaction which comes into mind is dipole-dipole interaction. In a crystal, consider two such magnetic atoms with moment of $1\mu_B$ each, separated by distance of 1Å the energy associated with dipole interaction will be of the order of 0.05 eV which is equivalent to about 1 K in temperature.

In real materials such as magnetite (Fe_3O_4) [37, 38], very high magnetic ordering temperature ($\sim$ 860 K) suggests different origin other than the magnetostatic interaction between dipoles. Exchange interaction lie at the heart of the long range ordering phenomenon. The coulomb force between two electrons can act in many ways. In addition with the Pauli exclusion principle and the Coulomb re-

pulsion between electrons, the electron-electron repulsion also gives exchange interaction. It is completely quantum mechanical in origin. Magnetism in materials is manifested by the electronic structure in combination with the hopping of electrons(kinetic exchange). This kinetic process is restricted by the Pauli principle, responsible for the long range magnetic ordering or spontaneous magnetization in materials. Another manifestation of the electron-electron interaction is electron correlation. It is now well accepted that the interplay between electron correlation and band formation (result of hopping interaction) plays an important role in magnetism and other related novel phenomena in solids.

To understand the energetics involved in determining the ordering of magnetic moments, it is useful to discuss briefly about correlation effects first.

1.7.1 Correlation Effects

In simple words, any electronic phenomenon which can not be explained by independent-electron approximation which is nothing but band theory for crystalline solids can be regarded as electron correlation. If we consider density functional theory, where density is the basic variable expectation value of a product of two electron densities one at position $\mathbf{r_1}$ with density $n(\mathbf{r_1})$ and another electron at position $\mathbf{r_2}$ with density $n(\mathbf{r_2})$, $< n(\mathbf{r_1})\mathbf{n}(\mathbf{r_2}) >$, as product of individual averages i.e. $< n(\mathbf{r_1}) >< \mathbf{n}(\mathbf{r_2}) >$. If we approach the problem from a wave function based approach we can not factorize the wavefunction of many electron system into individual wave functions. Thus, the correlation effect is beyond the factorization approximation as considered in Hartree or Hartree-Fock theory.

Bloch theorem [39] assumes an electron behaves like a free particle and so, can be approximated as plane-wave in a periodic lattice. However, when the number of electrons in a solid increases, the mutual electron-electron ($e^- - e^-$) interaction becomes more significant.Therefore this affects the movement of electrons which are no more free particles as they feel the repulsion of other electrons. In d electrons in transition-metal oxides there are two competing forces : Electron correlations which tend to localize electrons individually at the atomic sites while hybridization with oxygen p tends to delocalize electrons. The competition between these two makes correlated materials excellent resources for studying various electron properties [40–42].

In a simple picture, $\tau \propto \frac{1}{W}$. where τ is the average time spent on an atom corresponds to the band width, W, which is the result of hopping interactions. Therefore, the narrow band corresponds to the longer time that an electron resides in an atom. Thereby, it feels the presence of other electrons. For example, many materials such as partially filled d bands in transition metals V, Cr, Fe etc. and their oxides, or rare-earth metals such as Ce, are examples of narrow band material. The narrow bands enhances the correlation between the electrons, making them 'strongly correlated' materials. As compared to non-interacting particles in band theory, the correlation gives rise to profound changes in the physical properties, quantitatively as well as qualitatively. Nickel Oxide (NiO) is one example which has the ground state with an unfilled valence d-shell. The standard methods of density functional theory(DFT) predicts a metallic state or as a Slater insulator, with a very small gap [43–45]. However, both the gap and the magnetic moment are significantly underestimated when compared to the experimentally measured values. To get the experimentally observed band gap and moment [46], one also needs to take into account strong electron correlations bring this narrow band system close to the Mott regime, therefore, NiO is a Mott insulator/charge transfer insulator [42, 47]. Correlated materials are often very sensitive to the external parameters. Correlation also play an important role in the cuperates in which one has high temperature superconductivity [48]. In particular, the interplay between the spin, charge and orbital degrees of freedom of the correlated d and f electrons and with the lattice degrees of freedom gives varieties of unusual phenomena at low temperatures.

1.7.2   The Mott-Hubbard Model

An accepted model for electron correlations in the transition metal oxides is the Mott-Hubbard model [49]. It was initially formulated by Mott and further investigated by Hubbard. This Mott-Hubbard Hamiltonian consists of two terms, the kinetic energy or hopping term which is responsible for band width, $\hat{H}_{tb}$, and the correlation energy term, $\hat{H}_U$:

$$\hat{H} = \hat{H}_{tb} + \hat{H}_U, \tag{1.4}$$

$$\hat{H}_{tb} = -\sum_{i,j,\sigma} t_{ij} \hat{c}_{i\sigma}^{\dagger} \hat{c}_{j\sigma} + h.c., \tag{1.5}$$

$$\hat{H}_U = U \sum_i \hat{n}_{i\uparrow} \hat{n}_{i\downarrow}, \tag{1.6}$$

where, $\hat{c}_{i\sigma}^\dagger$ ($\hat{c}_{i\sigma}$) represents the creation (annihilation) operator for electrons with spin σ at site i, and $\hat{n}_{i\sigma}$ = $\hat{c}_{i\sigma}^\dagger \hat{c}_{i\sigma}$, represents the number operator. t_{ij} is the hopping amplitude, involves in the band formation. The hopping amplitude is the measure of the overlap between neighboring wavefunctions. A strong overlap results in a large bandwidth given by $W = 2nt$ where n is the number of nearest neighbors. It is worth discussing the two limiting cases of large t limit ($t \gg U$), we can drop the second term from Mott-Hubbard Hamiltonian and the model becomes identical to the tight-binding model and the electrons are delocalized over the whole crystal and this results in a metallic state. However, in the large U limit ($U \gg t$), the double occupancy of a site becomes energetically unfavorable and therefore, the hopping interaction term will be very small and can be dropped from the Hamiltonian. The band therefore splits into two bands, lower and upper Hubbard bands, separated by an energy U. In the half-filled system the lower Hubbard-band is completely filled while the upper Hubbard band is always empty and this results in an insulating state.

The physics of the transition metal oxides of interest lies in the region in between the two extreme cases. The competition between the hopping interaction and the correlation results into various complicated many-body phenomena. One of important correlated phenomenon that is actively investigated is the metal-insulator transition [50]. Fig. 1.6 illustrates a schematic phase diagram for the metal-insulator transition which depend on the band-width W which is governed by hopping strength t, electron correlation U and the filling, n. The shaded region represents the insulating region. From Fig. 1.6 we can think of two types of metal-insulator transitions. One is the band controlled transition, where, the metal-insulator transition takes place through the variation of the ratio $\frac{U}{t}$ keeping the number of electron or filling of band fixed. Second, the filling controlled transition, where, for a fixed value of $\frac{U}{t}$, the metal-insulator transition occurs by adding or removing electrons through chemical doping.

A common consequence of the Mott-Hubbard model is the ordering of spin, charge and orbitals [51–53]. In solids, where atoms are arranged in a lattice, such ordering is stabilized by complex interactions between the electronic degrees of freedom and the lattice. The spin ordering or the magnetism in materials is a direct manifestation of the electron interactions. As we mentioned earlier that the
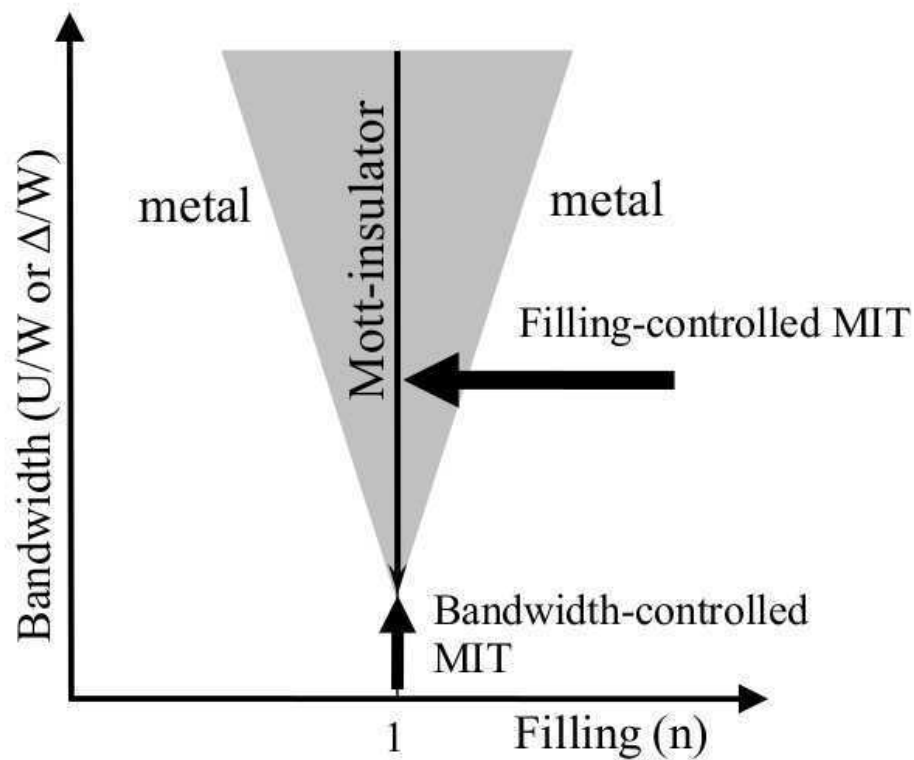
Figure 1.6 The schematic metal-insulator phase diagram within the Hubbard model in the electron correlation strength (U/W or Δ/W) and band filling (n) plane. There are two routes for the metal-insulator transition (MIT), which are shown as the bandwidth-controlled MIT and the filling-controlled MIT. This figure is redrawn from Ref. [50]

interatomic exchange interaction lies at the core of magnetism in solids.

Such exchange interactions are mediated by different mechanisms depending on the system and we now discuss some of the most important mechanisms are described below.

1.8   Direct Exchange

If the electrons on neighboring atoms interact directly such exchange is known as **direct exchange**. The direct exchange is the result of direct overlap of electronic wave functions of the neighboring atoms. Fig. 1.7(a), shows a simple picture of direct exchange where the antiparallel spin alignment is favored, as it allows the electrons to hop to the neighboring site. In this simple picture, energies corresponding
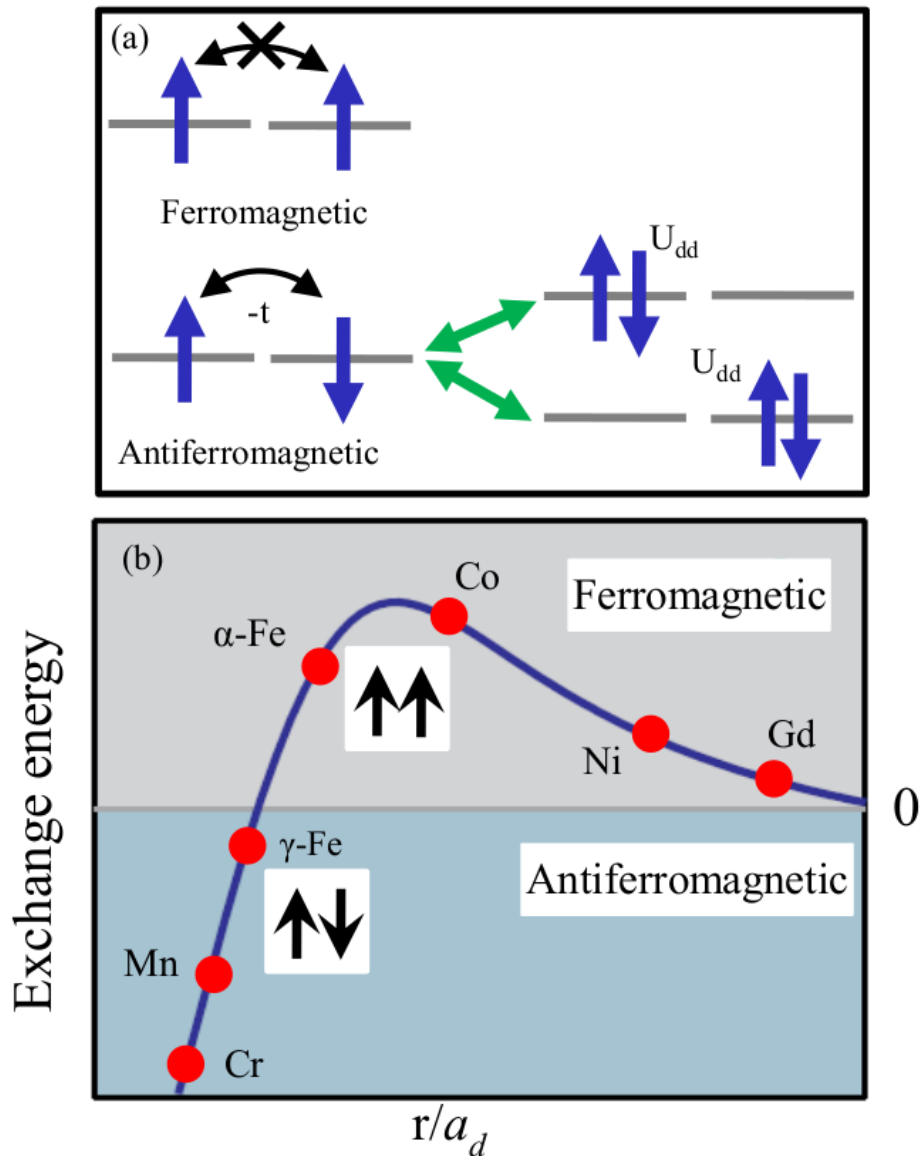
Figure 1.7 A simple picture of direct exchange, (a), favors the antiparallel alignment of the spins (lower) as it allows the electrons to hop to the neighboring site and costs an energy of U_{dd}. While, in the parallel alignment of the spins (upper) hopping is suppressed by the Pauli exclusion principle. The Bethe-Slater curve in (b) yields that elements above the horizontal axis are ferromagnetic, below that axis are antiferromagnetic.

to the antiparallel and parallel states are $-\frac{4t^2}{U_{dd}}$ and 0 respectively(neglecting the onsite energy), resulting in a singlet-triplet splitting of $J = -\frac{4t^2}{U_{dd}}$. Here t is the hopping interaction strength which is a function of the separation between sites and the relative orientation as well as nature of the orbitals which are

involved in the hopping process. In the direct exchange process, one can view the spin Hamiltonian as the Heisenberg Hamiltonian,

$$H_{Heis} = -\frac{1}{2} \sum_{i \neq j} J_{ij} \mathbf{S}_i \cdot \mathbf{S}_j, \tag{1.7}$$

The values of J_{ij} may be negative or positive, corresponding to the antiferromagnetic or ferromagnetic ground state respectively. Bethe-Slater curve (Fig. 1.7(b), taken from Ref. [54]) represents J_{ij} for transition metals as a function of $\frac{r}{a_d}$, where r is the distance between sites and a_d is the radius of the 3d electron shell. The curve shows how interatomic distance can vary the exchange interaction not only the magnitude but also sign. However, too large interatomic distance result in vanishingly small coupling strength, resulting in paramagnetism.

Very often direct exchange fails to determine the long range ordering in solids because in magnetic compounds usually the separation between magnetic ions are large and so direct overlap of wavefunctions are unlikely. Thus in many magnetic materials it is necessary to think of a different mechanism which is not direct.

1.9 Super exchange

There are a large number of antiferromagnetic insulators present in nature most of them are transition metal compounds in which the transition metals are separated by large anions. In this case the direct hopping will be negligible. The kinetic exchange in these compounds mediated through the anions and in fact enhanced by the covalent mixing between anions and transition metal orbitals. This has been shown by Anderson [55]. Enhanced kinetic energy is responsible for large ordering temperatures of such compounds.

We can understand the superexchange mechanism, by simple schematic diagram shown in Fig. 1.8(b). Consider two $d_{3z^2-r^2}$ orbitals, separate by an intermediate anion p_z orbital, as in Fig. 1.8(a). If the spins on transition metals are anti-parallel or antiferromagnetically aligned as shown in Fig. 1.8(b) in the first step the electron with up spin can hop from anion p orbital to the transition metal site with down spin.
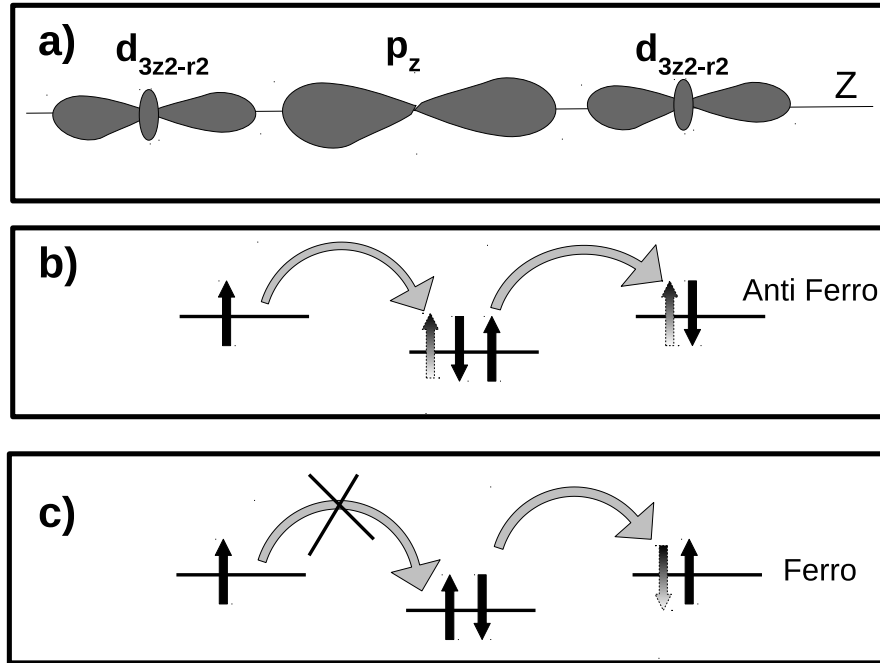
Figure 1.8 A simple picture of super-exchange where the orbital on the central site is different from the orbitals on the sides. Typically, two d orbitals are coupled via an intermediate oxygen p orbital as in 4(a). For antiparallel alignment of the spins on two d orbitals, (b) describe the ways that two consecutive hopping processes are possible, while in (c) for ferromagnetic case, the Pauli principle forbids the second hopping process.

In the second step the up spin electron from the transition metal in left can hop to the anion. The two step process can be viewed as virtual hopping of up spin electron from left to the right and similarly virtual hopping of down spin from right to left. Note that in this exchange process the total spin of all configurations will always remain unaltered. Through this process, the antiferromagnetic spin arrangement is favored and the energy difference between the ferromagetic and antiferromagnetic arrangement is given by,

$$J_{afm} = \frac{4t_{pd}^4}{(U_{dd} + \Delta_{pd})^2} \left(\frac{1}{U_{dd}} + \frac{1}{U_{dd} + \Delta_{pd}} \right),$$ (1.8)

where $\Delta_{pd} = \varepsilon_d - \varepsilon_p$, the charge transfer energy; U_{dd}, the Coulomb repulsion between two electrons in a d-orbital and t_{pd}, the hopping interaction between electrons on d and p orbitals.

So far, in the above discussion, we have assumed all the hopping along a line or the transition metal

anion transition metal angle is 180° as shown in Fig. 1.8(a). The physics of super exchange reverse

and favor ferromagnetism when two transition metals with the d orbitals say, ($d_{3x^2-r^2}$ and $d_{3y^2-r^2}$) form

a 90° angle with the connecting oxygen with the p orbitals (p_x and p_y), as shown in Fig. 1.9(a). The
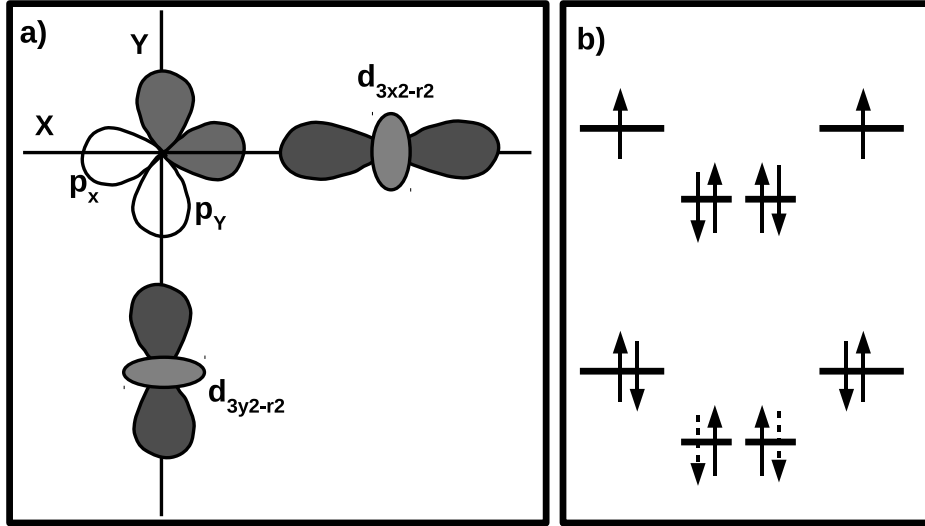
Figure 1.9 In a 90° arrangement of d - p - d group as in (a), one finds that the d orbitals are coupled to the orthogonal p orbitals, the ferromagnetic super-exchange in (b) is mediated via the Coulomb exchange on the connecting oxygen.

hopping in this geometry is different than the linear geometry due to involvement of two p-orbitals

in the process. The entire process is shown schematically in Fig. 1.9(b). The two orbitals on oxygen

allow a one way hopping which results in weak ferromagnetic coupling between transition metals. So,

superexchange is mediated via the Coulomb exchange on the connecting oxygen and is ferromagnetic

in nature. The exchange coupling has the form,

$$J_{fm} = -\frac{4t_{pd}^4}{(U_{dd}+\Delta_{pd})^2}\frac{2J_O}{4(U_{dd}+\Delta_{pd})^2-J_O^2}. \tag{1.9}$$

It is significantly weaker than J_{afm}. However, in real materials, the structural distortion makes the

cation-anion-cation angle deviate from both 180° nor 90°. When that angle differs from 90°, hopping

between d orbitals is allowed via the same p orbital and hence, the antiferromagnetic superexchange processes start to compete with the ferromagnetic superexchange.

1.10   Magnetism in metal: Double Exchange Model

The double exchange model first proposed by Zener in 1951 [56] to explain the ferromagnetism in metals, such as Ni and Fe. Moreover, double-exchange process is commonly encountered in mixed valence systems [57] where itinerant electrons interact with local spins and favor ferromagnetism in such compounds. It can be easily understood by the schematic diagram shown in Fig.1.10.
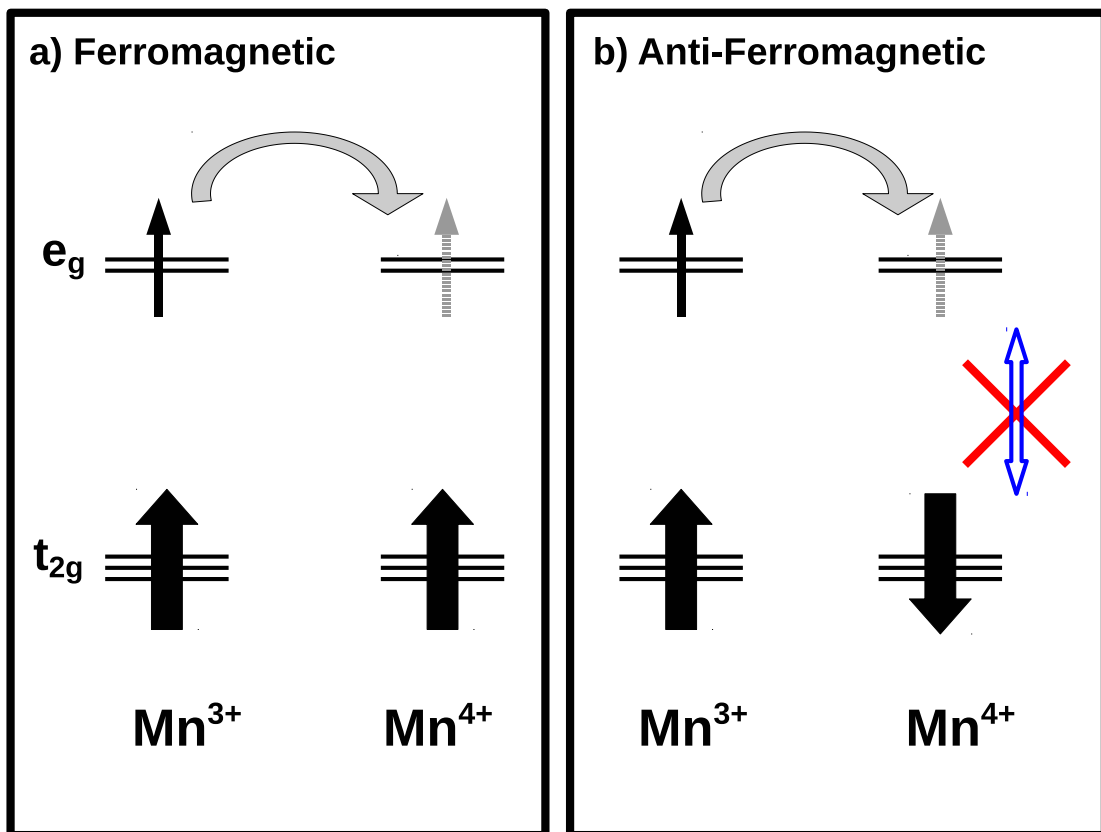
Figure 1.10 The double-exchange mechanism in hole doped manganite perovskite. coupling between the localized spins on Mn^{3+} and Mn^{4+} ions and the itinerant electrons in a) ferromagnetic alignment (b) antiferromagnetic alignment of localized spin. The ferromagnetic alignment of the localized spins stabilized through Hund's exchange coupling.

In the earlier exchange mechanisms, we have considered systems with an integer number of electrons per site. In a mixed valence system, the average number of electrons per cation site is non-integral, so even for strong correlations, U, electrons can hop between sites without any cost of U. So, this mechanism asserts that the conducting electrons will remember their spin orientations (effect of strong Hund's exchange J_H) when moving around. These compounds are usually metallic and ferromagnetic for example, in $La_{1-x}Sr_xMnO_3$ [58]. La in perovskite $LaMnO_3$ is trivalent (La^{3+}) so Mn goes to Mn^{3+} oxidation state with configuration of $t_{2g}^3 e_g^1$. When Sr is doped in the system it goes as Sr^{2+} and so, Mn goes into Mn^{4+} oxidation state with configuration of $t_{2g}^3 e_g^0$. The e_g electrons, which are usually strongly hybridized with the O-p orbitals can be treated as itinerant electron in the system. In this system the t_{2g} electrons which are less hybridized with O-p orbitals and found deepen in the valence band can be viewed as core-spin. The strong Hund's exchange J_H couples the itinerant e_g spin of $\sigma = \frac{1}{2}$ with the t_{2g} localized spin of $S = \frac{3}{2}$. The mechanism is illustrated in Fig. 1.10, where the delocalization of the e_g electrons occur when the core-spins are ferromagnetically aligned. The anti ferromagnetic alignment is not favored by intraatomic Hund's exchange J_H.

1.11   Model for Ferromagnetic Insulators

There are several ways to get ferromagnetic insulators like charge ordering, orbital ordering. Here we discuss two important routes to get a ferromagnetic insulators.

1.11.1   Goodenough-Kanamori-Anderson rule

Usually, magnetism in insulators is described by the super exchange mechanism which leads to antiferromagnetism. One of the principles that can be used for designing a ferromagnetic insulator is based on superexchange mechanism. The superexchange strength and the spin alignment not only depend upon the angle M-O-M as discussed earlier under section superexchange model, but also depends on the filling of the d orbitals on the metal atom. On the basis of various observations, a set of semi-empirical rules were developed over years by Goodenough and Kanamori. The main features of Goodenough-

Kanamori-Anderson rules [59–61] are summarized as,

(1) the superexchange will be antiferromagnetic when both orbitals on metal sites are either half-filled or when both are empty, shown in Fig. 1.11(a) and (b) respectively,

(2) the superexchange will be ferromagnetic when either (i) when one orbital is empty and the other half-filled or, (ii) one orbital is half-filled and the other full as shown in Fig. 1.11(c) and (d) respectively.
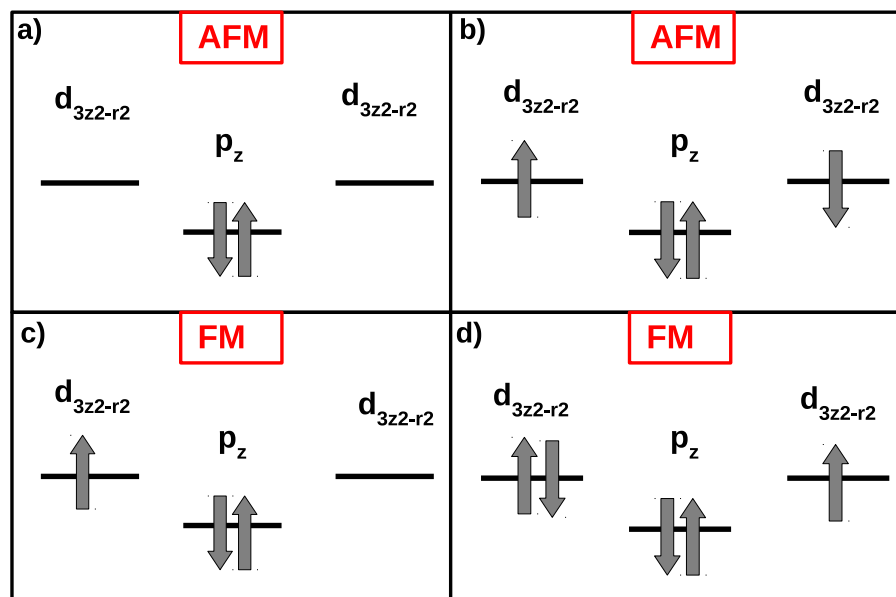
Figure 1.11 The Goodenough-Kanamori-Anderson rules: In a $180°$ geometry of d - p - d group, (a) and (b) yield the antiferromagnetic alignment of spins on d orbitals, while in (c) and (d) the favored alignments are ferromagnetic.

It can be explained by schematic diagram shown in Fig 1.11. We have considered four possibilities and the resultant spin alignment according to Goodenough-Kanamori rule. The last two schemes favor ferromagnetic alignment. These two situations can be used to get ferromagnetism in Insulators. This route is possible if we place an atom with filled e_g levels at one transition metal site of a doubled perovskite structure and another atom with empty e_g levels we can stabilize ferromagnetism in insulators. One example where this has been realized Bi_2NiMnO_6, which will be discussed in chapter-5 of the thesis.

1.11.2   Kugel-Khomskii Model

Another route to get ferromagnetism in insulators lies in physics of orbital ordering. Effects of the orbital ordering on the spin configuration was first discussed by Kugel and Khomskii, popularly known as Kugel-Khomskii model. In few compounds, the partially filled levels (e.g. t_{2g}, e_g etc.) make the orbital degree of freedom active and play an important role in the spin dynamics.

   Kugel-Khomskii showed in a seminal work that in the strongly correlated materials with degenerate t_{2g} or e_g symmetric orbitals, within a purely super-exchange mechanism through many-body effects could give rise to the orbital-ordering phenomena [62]. Associated with the spin (up or down) and
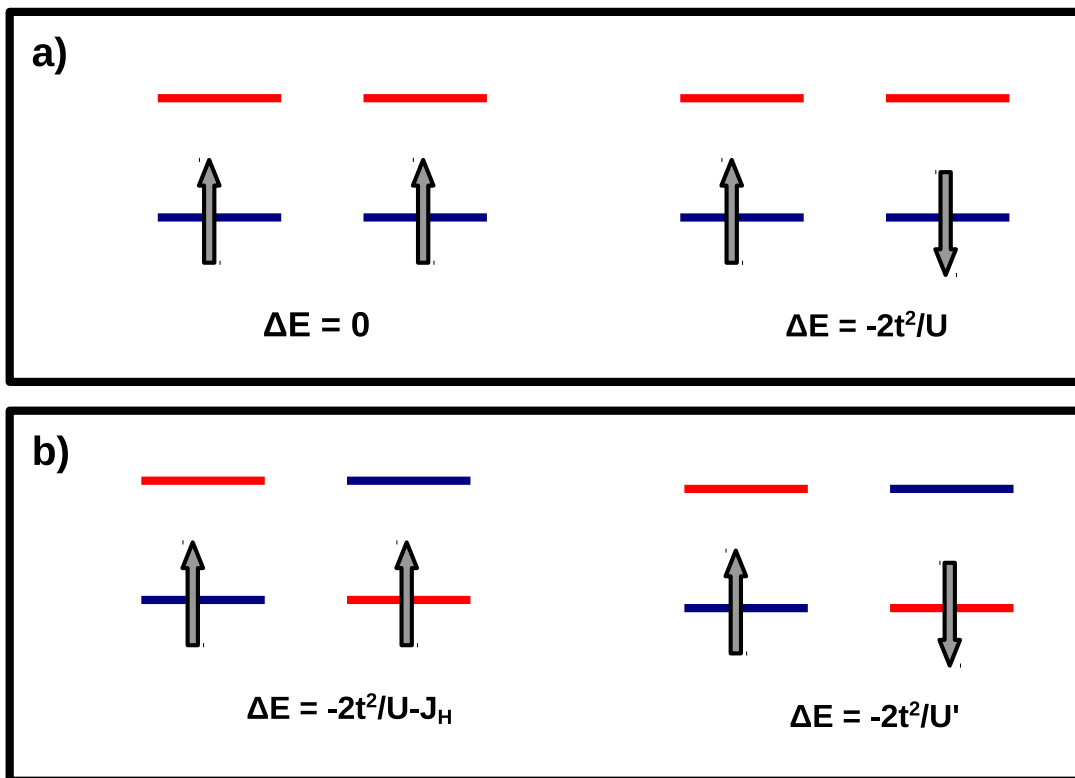
Figure 1.12 Super-exchange in the case of two-fold degenerate orbitals, two colors blue and red represent two different orbitals. (a) shows ferromagnetic and anti-ferromagnetic spin alignment and corresponding energies in ferro-orbital stacking and (b) shows ferromagnetic and anti-ferromagnetic spin alignment and corresponding energies in antiferro-orbital stacking .

orbital configurations, Fig. 1.12(a),(b) illustrate the energy gains calculated by using second order perturbation theory within super exchange model. U, U' and J_H are the intra and inter-orbital electron correlations and the Hund's exchange strength, respectively. From Fig. 1.12(b) it is clear that the parallel spin configuration with different orbital character is favored by Hund's coupling. One simple example is the magnetic ordering in LaMnO$_3$, where the orbital ordering in xy-plane results the ferromagnetic spin coupling in the plane, while ferro-orbital stacking leads to antiferromagnetic alignment in Z-direction.

1.12 Motivation of the Thesis

In this thesis we have studied various complex ordering that take place in transition metal oxides using a combination of ab-initio calculations as well as a mapping onto model Hamiltonians wherever possible. A substantial portion of this thesis is devoted to the study of ferromagnetic insulators and the microscopic considerations that results in ferromagnetism in an insulating state. In **Chapter-2** i have discussed the basic methods used in electronic structure calculations. Started with the many body Hamiltonian we have discussed different approximations and approaches which has been useful to understand the basic principles on which density function theory works.

Ferromagnetic insulators are rare. In most transition metal oxides, ferromagnetism is usually accompanied by metallicity . $K_2Cr_8O_{16}$ is one such example of a material which exhibits ferromagnetism even in its insulating phase with a metal to insulator transition taking place at a temperature of 95 K. In **Chapter-3** we have studied the electronic structure for the compound. We have proposed charge ordering as one route to explain the ferromagnetic insulating phase. K in the compound behaves like a perfect donor. We expected the doped electrons to occupy all Cr sites equally as there was nothing in the structure that distinguished between them. However, we found that few Cr sites were preferred over others, resulting in the existence of Cr^{3+} and Cr^{4+} sites in the ratio 1:3. The charge ordering we found was governed by a polaronic distortion and electron-electron interactions aided in stabilizing the insulating state. In **chapter-4**, we have presented the microscopic model to captured various aspects of

this charge ordering. A microscopic model has been constructed using Cr-d and O-p as its basis as well as constructed a basic model to understand the ferromagnetism. i have also compared the analogous compound $Rb_2Cr_8O_{16}$ which has the same structure but the ferromagnetic transition temperature is 100 K higher than that of $K_2Cr_8O_{16}$.

In **Chapter-5** we have studied the consequence of Cr doping in VO_2. VO_2 is a well known example of a system which has been studied for its metal-insulator transition. While the early work focused on the insulating monoclinic phase, recent studies have found interesting phase transitions in the rutile phase also. In this thesis we have studied Cr doping in the rutile phase of VO_2 which is found to be an insulating ferromagnet. An isovalent substitution of V by Cr would result in Cr adopting the 4+ valence state. However, we find a polaronic distortion taking place resulting in the formation of Cr^{3+} and V^{5+} motifs, with the other vanadiums remaining in the V^{4+} state. This leads to the insulating ground state which is also ferromagnetic.

In **Chapter-6** of this thesis we have examined a set of design principles to generate a class of ferromagnetic insulators. According to a rule originally postulated by Goodenough, in perovskite oxides two different transition metal atoms arranged in a rock salt structure one of which has half filled e_g levels and another with empty e_g levels will be a ferromagnetic insulator. This principle in addition to the introduction of Bi or Pb at the A-site of the perovskite was used to generate ferroelectric as well as ferromagnetic Bi_2NiMnO_6. Considering this compound, we first examined whether this compound was a ferromagnetic insulator. Interestingly we found that calculations using GGA for the exchange-correlation functional within density functional theory did not find any magnetic ordering. One had to go beyond GGA level calculations which we did by using an orbital dependent potential in the framework of GGA+U calculations. This was able to explain the ferromagnetic state. The origin of the stabilization of the magnetic state of ferromagnetism is understood in terms of microscopic considerations within a multiband Hubbard model. Having described the ground state magnetic structure we next examined whether the material was ferroelectric. Experimentally this was found to be ferroelectric as it showed an anomaly in the dielectric constant as a function of temperature . Our calculations reveal that this compound is not ferroelectric.

In **Chapter-7** we have studied the well known example of ferroelectric $BaTiO_3$. We have examined the microscopic considerations that result in ferroelectricity in the well-known example of BaTiO3.

Bibliography

[1] Abanti Nag, J. Manjanna, R. M. Tiwari and J. Gopalakrishnan, Chem. Mater., **20**, 4420(2008).

[2] K. Yamaura, E. Takayama-Muromachi, Phys. Rev. B, **64**, 224424(2001).

[3] S. Jin, T. H. Tiefel, M. McCormack, R. A. Fastnacht, R. Ramesh and L. H. Chen, Science **264**, 413 (1994).

[4] S. Jin, M. McCormack, T. H. Tiefel, and R. Ramesh, J. App. Phys., **76**, 6929(1994).

[5] M. Dawber, K. M. Rabe, and J. F. Scott, Rev. Mod. Phys. 77, 1083 (2005).

[6] V. Laukhin, V. Skumryev, X. Marti, D. Hrabovsky, F. Sanchez, M. V. Garcia Cuenca, C. Ferrater, M. Varela, U. Lüders, J. F. Bobo, and J. Fontcuberta, Phys. Rev. Lett. **97**, 227201 (2006).

[7] C. Thiele, K. Dörr, O. Bilani, J. Rödel, and L. Schultz, Phys. Rev. B **75**, 054408(2007).

[8] A. D. Rata, A. Herklotz, K. Nenkov, L. Schultz, and K. Dörr, Phys. Rev. Lett. **100**, 076401 (2008).

[9] J. H. vanSanten and G. H. Jonker, Physica **16**, 337 (1950).

[10] J. Zaanen and G. A. Sawatzky and J. W. Allen, Phys. Rev. Lett. **55**, 418 (1985).

[11] S. Biermann, A.I. Poteryaev, A. Georges, A.I. Lichtenstein, Phys. Rev. Lett. 94 026404 (2005)

[12] Y. Tokura, Physics Today 56, 50, July (2003).

[13] A. S. Bhalla, R. Guo and R. Roy, Mat. Res. Innovat. **4**, 3(2000), and references therein.

[14] Goldschmidt, V. M. Skr. Nor. Viedenk.-Akad., Kl. I: Mater.-

[15] H. D. Megaw Proc. Phys. Soc. **58**, 133(1946).

[16] C. J. Howard, H. T. Stokes, Acta Crystallogr. Sect. B ,**54** , 782(1998).

[17] Carl J. Balheusen, *An Introduction to Ligand Field Theory* (McGraw Hill, 1962).

[18] E. Pavarini and E. Koch, Phys. Rev. Lett. **104**, 086402 (20010).

[19] H. Sawada, Y. Morikawa, K. Terakura and N. Hamada, Phys. Rev. B **56**, 12154 (1997).

[20] H. -T. Jeng, S. -H. Lin and C. -S. Hsue, Phys. Rev. Lett. **97**, 067002 (2006).

[21] H. A. Jahn and E. Teller, Proc. Roy. Soc. London A **161**, 220 (1937).

[22] J. Hemberger, H. -A. Krug von Nidda, V. Fritsch, J. Deisenhofer, S. Lobina, T. Rudolf, P. Lunkenheimer, F. Lichtenberg, A. Loidl, D. Bruns and B. Buchner, Phys. Rev. Lett. **91**, 066403 (2003).

[23] Z. Fang and N. Nagaosa, Phys. Rev. Lett. **93**, 176404 (2004).

[24] E. Pavarini, E. Koch and A. I. Lichtenstein, Phys. Rev. Lett. **101**, 266405 (2008).

[25] E. du T. de Lacheisserie, D. Gignoux and M. Schlenker, *Magnetism: Fundamentals.* Springer, 3 (2005).

[26] H. P. Vowles, *Early Evolution of Power Engineering,* Isis (University of Chicago Press) **17**, 412 (1932).

[27] R. T. Merrill and M. W. McElhinny, *The Earth's magnetic field: Its history, origin and planetary perspective,* (second edition), San Francisco: Academic press, 1 (1983).

[28] J. C. Maxwell, Phil. Trans. R. Soc. Lond. **155**, 459 (1865).

[29] D. J. Griffiths, *Introduction to electrodynamics*, (third edition), Prentice Hall, 559 (1999).

[30] S. Goudsmit and R. de L. Kronig Naturwissenschaften **13**, 90 (1925).

[31] G. E. Uhlenbeck and S. Goudsmit, Naturwissenschaften **47**, 953 (1925).

[32] P. A. M. Dirac, Proc. R. Soc. London A **117**, 610 (1928).

[33] W. Pauli, Phys. Rev. **58**, 716 (1940).

[34] A. Galindo and C. Sanchez del Rio, Am. J. Phys. **29**, 582 (1961).

[35] R. J. Boyd and C. A. Coulson, J. Phys. B: At. Mol. Phys. **7**, 1805 (1974).

[36] D. Dill, *Notes on General Chemistry* (third edition), Chapter 3, 4, Boston University, (2008).

[37] E. J. W. Verwey, Nature (London) **144**, 327 (1939).

[38] E. J. W. Verwey and P. W. Haayman, Physica **8**, 979 (1941).

[39] F. Bloch, Z. Phys. **57**, 545 (1929)

[40] P. A. Lee and T.V. Ramakrishnan, Rev. Mod. Phys. **57**, 287 (1985).

[41] D. Belitz and T. R. Kirkpatrick, Rev. Mod. Phys. **66**, 261 (1994).

[42] N.F. Mott,*Metal Insulator Transitions*, (Barnes and Noble, New York 1974).

[43] J. C. Slater, Phys. Rev. **59**, 537 (1957).

[44] K. Terakura, A. R. Williams, T. Oguchi and J. Kubler, Phys. Rev. Lett. **52**, 1830 (1984).

[45] K. Terakura, T. Oguchi, A. R. Williams and J. Kubler, Phys. Rev. B **30**, 4734 (1984).

[46] G. A. Sawatzky and J. W. Allen, Phys. Rev. Lett. **53**, 2339 (1984).

[47] N. F. Mott, Proc. Phys. Soc. London, Sect. A **62**, 416 (1949).

[48] J. G. Bednorz and K.A. Muller, Z. Phys. B **64**, 189 (1986).

[49] J. Hubbard, Proc. Roy. Soc. A **277**, 237 (1964); *ibid.* **281**, 401 (1964).

[50] M. Imada, A. Fujimori and Y. Tokura, Rev. Mod. Phys. **70**, 1039 (1998).

[51] Y. Tokura, A. Urushibara, Y. Moritomo, T. Arima, A. Asamitsu, G. Kido and N. Furukawa, J. Phys. Soc. Jpn. **63**, 3931 (1994).

[52] Y. Tokura and Y. Tomioka, J. Magn. Magn. Mater. **200**, 1 (1999).

[53] J. M. D. Coey, M. Viret and S. von Molnar, Adv. Phys. **48**, 167 (1999).

[54] S. Chikazumi, *Physics of Ferromagnetism*, Oxford University Press, New York, 125 (1997).

[55] P. W. Anderson, Phys. Rev. **79**, 350 (1950).

[56] C. Zener, Phys. Rev. **82**, 403 (1951).

[57] P. -G. de Gennes, Phys. Rev. **118**, 141 (1960).

[58] W. E. Pickett and D. J. Singh, Phys. Rev. B **53**, 1146 (1996).

[59] J. B. Goodenough, Phys. Rev. **100**, 564 (1955).

[60] J. B. Goodenough, J. Phys. Chem. Solids **6**, 287 (1958).

[61] J. Kanamori, J. Phys. Chem. Solids **10**, 87 (1959).

[62] K. I. Kugel and D. I. Khomskii, Sov. Phys. Usp. **25**, 231 (1982).

Chapter 2

Theory of electronic structure calculations

2.1   Introduction

The behaviors of electron in the system is governed by quantum mechanics and statistical mechanics. Theoretical methods of quantum mechanics and statistical mechanics are main tool to understand the electronic structure of the matter. Any physical system made of atoms and atoms consist heavy positively charged particle *nuclei* and light negatively charged particle *electrons*. If N_n and N_e being number of nuclei and the electrons in the system respectively, then the problem can be described by the following Hamiltonian

$$H = -\frac{\hbar^2}{2m_e}\sum_{i=1}^{N_e}\nabla^2_{\mathbf{r_i}} - \frac{\hbar^2}{2M_I}\sum_{I=1}^{N_n}\nabla^2_{\mathbf{R_I}} - \sum_{i,I}\frac{Z_I e^2}{|\mathbf{R_I}-\mathbf{r_i}|} + \sum_{i>j}\frac{e^2}{|\mathbf{r_i}-\mathbf{r_j}|} + \sum_{I>J}\frac{Z_I Z_J e^2}{|\mathbf{R_I}-\mathbf{R_J}|} \tag{2.1}$$

where r_i is the position of the ith electron. R_I is the position of the Ith nucleus, Z_I is the atomic number of the nucleus, m_e is the mass of the ith electron and M_I is the mass of the Ith nucleus respectively. The first term of equation 2.1 is the kinetic energy term for the electrons while the second one is kinetic energy term for the nuclei. The last three terms are the potential energy terms describe the interaction between electrons and nuclei, between electrons and between the nuclei respectively. The exact solution of the Hamiltonian is not possible. The central issue in electronic structure calculations is how accurately we can solve the equation (1) specially the 3rd term which is electronic correlations.

The nucleus is much much heavier than the electrons, so, the motion of nucleus can be ignored when we are considering electronic motions. This is approximation is the Born-Oppenheimer [1] or adiabatic approximation. This makes the 2nd term which represents kinetic energy of nuclei very small and so we can ignore it safely. . The last term of Hamiltonian which is ion-ion interaction will be constant and we can drop the term from the Hamiltonian. So this approximation reduced the complex problem into a problem of N electrons only moving in the field of fixed ion cores. The equation (1) reduces to the following form

$$H = -\sum_{i=1}^{N} \frac{\hbar^2}{2m_e} \triangledown_{\mathbf{r_i}}^2 - \frac{1}{4\pi\varepsilon_0} \sum_{i,I} \frac{Z_I e^2}{|\mathbf{R_I} - \mathbf{r_i}|} + \frac{1}{2}\frac{1}{4\pi\varepsilon_0} \sum_{i,j} \frac{e^2}{|\mathbf{r_i} - \mathbf{r_j}|} \tag{2.2}$$

2.2   Single-particle approximation

Even with the simplification solving the many electron problem is very difficult and we need further simplifications. We need to map the problem onto a single particle in which we can reduce the problem into a problem of single particle moving into some kind of effective potential. We reduce the problem of interacting particle into problem of non-interacting particles. electron-electron interactions. The approaches towards the problem may be classified into two categories *wave function based* and *density functional theory based approach*.

2.2.1   Wave function based approaches

There are two basic single particle approaches Hartree like and Hartree-Fock like. Both are similar in the sense they both assume electrons are uncorrelated except that they must obey Pauli exclusion principle. In 1928 Douglas Hartree [2] Hartree first time approximate many electron wave function as a product of single-electron wave functions. The Hartree approximation is capable of solving the multi-electron Schrödinger equation of the wave function of the form $\psi(r_1, r_2, ..., r_n)$, where r_i is spatial coordinates. He solved the equation for each electron moving in a central potential due to other electrons and the nucleus. This approximation treated electron-electron repulsion in mean-field

way and neglects the exchange and correlation completely. This also does not take into account the nature of electron wave function which must be antisymmetric as electron is fermion. In 1930, next level of sophistication has been proposed by Fock [3] which takes into account the antisymmetric nature of electron wave function. In place of taking total wavefunction as a product of single electron wavefunction he took total wavefunction as slater determinant.

$$\psi(x_1, x_2, ..., x_N) = \frac{1}{\sqrt{N!}} \begin{vmatrix} \psi_1(\mathbf{r_1}) & \psi_1(\mathbf{r_2}) & \cdots & \psi_1(\mathbf{r_N}) \\ \psi_2(\mathbf{r_1}) & \psi_2(\mathbf{r_2}) & \cdots & \psi_2(\mathbf{r_N}) \\ \vdots & \vdots & \ddots & \vdots \\ \psi_N(\mathbf{r_1}) & \psi_N(\mathbf{r_2}) & \cdots & \psi_N(\mathbf{r_N}) \end{vmatrix}. \tag{2.3}$$

By using variational principle we can show that such one electron wave functions satisfy the Hartree-Fock equations like

$$[-\frac{\hbar^2}{2m_e}\nabla^2_{\mathbf{r_i}} + V_{ion}(r_i) + V_i^X + V_i^H(r_i)]\psi_i(r_i) = \varepsilon(i)\psi_i(r_i) \tag{2.4}$$

The determinant form of wavefunction above is helpful in obtaining the exchange term in addition to Hartree potential.

$$e^2 \sum_{j}^{occ} \int d^3r' \psi_j^*(r^j)\psi_j(r^j)\frac{1}{|\mathbf{r}-\mathbf{r'}|} \tag{2.5}$$

$$-\frac{1}{2}\sum_{j} \int d^3r' \psi_j^*(r')\psi_i(r')\frac{1}{|\mathbf{r}-\mathbf{r'}|}\psi_j(r) \tag{2.6}$$

that acts between electrons of the same spin. Applying this third term to the Hartree equation leads to the Hartree-Fock equation. The latter equation is written as follows:

$$H\psi(r) = [T_{elec} + V_{ion}(r) + V_{elec}]\psi_i(r) - \frac{1}{2}\sum_{j} \int d^3r' \psi_j^*(r')\psi_i(r')\frac{1}{|\mathbf{r}-\mathbf{r'}|}\psi_j(r) \tag{2.7}$$

The screening potential consist of both these Hartree and exchange term. The exchange term V_i^X is difficult to derive in practice due to its not non-local nature. Consequently the computational cost for Hartree-Fock approach is very high which restrict the method to small systems. In agreement with

the variational principle, the Hartree-Fock energy E_0^{HF} is higher than the exact ground state energy of many body system

2.2.2 Density Functional Theory

Density functional theory (DFT) is one of the most popular tools for predicting the ground-state properties of electronic systems (metals, semiconductors and insulators). The origin of DFT lies in the classic paper of Hohenberg and Kohn [4] in 1964. They assume density of particle in ground state as basic variable and all properties of the system can be considered to be unique functional of the ground state density. Modern days treatment of electron in condensed matter is based on the formulation of DFT by Kohn and Sham [5]. DFT becomes popular in 1970s and 1998 after remarkable success of Local Density approximations(LDA) and generalized-gradient approximation(GGA) functional within the Kohn-Sham approach.

In DFT one ignores the precise details of the many-electron wave function $\psi(\mathbf{r_1}, \mathbf{r_2}, \ldots, \mathbf{r_N})$ and considers the density of electrons in the system

$$\rho(\mathbf{r}) = N \int \psi^*(\mathbf{r}, \mathbf{r_2}, \ldots, \mathbf{r_N}) \psi(\mathbf{r}, \mathbf{r_2}, \cdots, \mathbf{r_N}) \, d\mathbf{r_2} d\mathbf{r_3} \ldots d\mathbf{r_N}$$

as the basic variable.

Although DFT is significant, it fails to properly describe the van der Waals forces in sparse materials. It also underestimates the band gaps of semiconductors and some other electronic properties of highly correlated systems and this is related to aspects of formalism that we discuss below. It is still a current focus of improvement in research.

2.2.2.1 Basic theorems of DFT and Kohn-Sham equation

Density functional theory is based upon two basic theorems first given and proved by Hohenberg and Kohn [4]:

Theorem I : For any system of interacting particle in an external potential V_{ext}, There is a one-to-one correspondence between the ground-state density $\rho(\mathbf{r})$ and the external potential V_{ext}, except for a

constant. An immediate consequence is that all properties of the system or the expectation value of all observables $\hat{O}$ are unique functional of the exact ground-state electron density:

$$\langle \Psi | \hat{O} | \Psi \rangle = O[\rho]$$

Proof: Suppose that there are two different external potentials V_{ext}^1 and V_{ext}^2 which are differ by more than a constant and they corresponds to the same ground state density $\rho(\mathbf{r})$. The two external potential will result into two different Hamiltonian, $\mathbf{H^1}$ and $\mathbf{H^2}$ and two different ground states ψ_1 and ψ_2, which are assumed to have the same ground state density $\rho(\mathbf{r})$. ψ_2 is not the ground state of $\mathbf{H^1}$, so

$$
\begin{aligned}
E_1 &= \langle \psi_1 | H_1 | \psi_1 \rangle \\
&< \langle \psi_2 | H_1 | \psi_2 \rangle = \langle \psi_2 | H_2 | \psi_2 \rangle + \langle \psi_1 | [H_1 - H_2] | \psi_1 \rangle \\
&< E_2 + \int dr \rho(r) \left[V_{ext}^1(r) - V_{ext}^2(r) \right]
\end{aligned}
$$

We can get similar equation for E_2 by following the same steps,

$$E_2 < E_1 + \int dr \rho(r) \left[V_{ext}^2(r) - V_{ext}^1(r) \right]$$

adding both the equations we will arrive at contradictory inequality

$$E_1 + E_2 < E_2 + E_1$$

Hence the assumption of identical density arising from two different external potentials is wrong. This automatically implies the following:

A given $\rho(\mathbf{r})$ uniquely determines the external potential $v(\mathbf{r})$ to within a constant.

$$\Downarrow$$

Since $V(\mathbf{r})$ is fixed, the Hamiltonian and hence in principle the wave-function is also fixed by the density.

$$\Downarrow$$

Since the wave-function is a functional of density, the energy functional $E_V[\rho]$ for a given external potential $V(\mathbf{r})$ is a unique functional of the density.

Upto now there is no prescription has been given to solve the problem. We are still facing the same problem of many electron moving in the potential due to the nuclei.

Theorem II : For any particular V_{ext}, A universal energy functional $E(\rho)$ can be defined in terms of the density ρ and the exact ground state energy is the global minimum value of this functional. The functional $E(\rho)$ alone is sufficient to determine the exact ground state energy and density.

Proof: Since all properties are uniquely determined if $\rho(r)$ is given, then each property can be written as a functional of $\rho(r)$. So we can write total energy functional

$$E_{V_{ext}}[\rho] \quad = \quad \underbrace{\langle \Psi | \hat{T} + \hat{V} | \Psi \rangle}_{F_{HK}} + \langle \Psi | \hat{V}_{ext} | \Psi \rangle \tag{2.8}$$

$$= \quad F_{HK}[\rho] + \int \rho(\mathbf{r}) V_{ext}(\mathbf{r}) \, d\mathbf{r} \tag{2.9}$$

The functional $F_{HK}[\rho]$ includes all internal energies, kinetic and potential, of the system of interacting electrons. Which must be universal as kinetic energy as well as potential energy of the system is functional only of density.

Suppose a system with ground state density $\rho_1(r)$. Then the Hohenberg-Kohn functional is equal to the expectation value of the Hamiltonian in the unique ground state, which has the wavefunction ψ_1

$$E_1 \quad = \quad \langle \psi_1 | H_1 | \psi_1 \rangle$$

now consider a different ground state density $\rho_2(r)$ which corresponds to a different wavefunction ψ_2 So,

$$E_1 = \langle \psi_1 | H_1 | \psi_1 \rangle < \langle \psi_2 | H_1 | \psi_2 \rangle = E_2$$

So it follows that if the functional F_{HK} is known, then minimizing the total energy of the system with respect to density function, one can find the exact ground state density and energy.

Now to reduce the expression2.8 to a single particle equation, one can write the energy functional as

$$F_{HK}(\rho) \quad = \quad T(\rho) + E_H(\rho) + E_{XC}(\rho)$$

Here, the second term is the mean field inter-electron coulomb energy or Hartree energy came from the electron-electron term in the functional. The third term in the expression is the non-classical many-body exchange correlation energy functional. So, the ground-state energy functional in the Kohn-Sham approach is

$$E_{V_{ext}}[\rho] = T_0[\rho] + V_H[\rho] + E_{XC}[\rho] + V_{ext}[\rho] \tag{2.10}$$

First term in the expression is non-interacting kinetic term. The corresponding Hamiltonian known as Kohn-Sham Hamiltonian is

$$\begin{aligned}
\hat{H}_{KS} \quad &= \quad \hat{T}_0 + \hat{V}_H + \hat{V}_{XC} + \hat{V}_{ext} \tag{2.11}\\
&= \quad -\frac{\hbar^2}{2m_e}\nabla_i^2 + \frac{e^2}{4\pi\varepsilon_0}\int \frac{\rho(\acute{\mathbf{r}})}{|\mathbf{r}-\acute{\mathbf{r}}|}d\acute{\mathbf{r}} + \hat{V}_{XC} + \hat{V}_{ext}
\end{aligned}$$

where the exchange-correlation potential is given by the functional derivative

$$\hat{V}_{XC} \quad = \quad \frac{\delta E_{XC}[\rho]}{\delta\rho} \tag{2.12}$$

For evaluating the energy functional $E_{V_{ext}}[\rho]$ 1) We need a self consistent method to get the ground state density correctly 2) The evaluation of T_s from $\rho(r)$ can not be done directly 3) The change functional $E_{(XC)}$ is unknown and must therefore be written in simple and sufficiently accurate form.

These difficulties were resolved by using Lagrange's multiplier technique and by minimizing the E_{KS} ($E_{V_{ext}}$ in Eq.2.10) with constraint of normalized density $\int \rho(\mathbf{r})\,d\mathbf{r} = N$.

$$\frac{\delta}{\delta \rho} \{E_{KS}[\rho] - \lambda N\} = 0 \qquad (2.13)$$

λ is the Lagrange multiplier. Using Eq.2.10, one gets,

$$\frac{\delta T_0[\rho]}{\delta \rho(\mathbf{r})} + V_{KS}(\mathbf{r}) = \lambda \qquad (2.14)$$

where

$$V_{KS}(\mathbf{r}) = v(\mathbf{r}) + \frac{e^2}{4\pi\varepsilon_0} \int \frac{\rho(\acute{\mathbf{r}})}{|\mathbf{r} - \acute{\mathbf{r}}|} d\acute{\mathbf{r}} + \frac{\delta E_{XC}}{\delta \rho(\mathbf{r})}$$

Kohn and Sham showed that solving Eq.2.14 is equivalent to solving the following set of single-particle Schrödinger-like equations for the variational wave-functions of fictitious non-interacting electrons

$$\left[-\frac{\hbar^2}{2m_e}\nabla^2 + V_{KS}(\mathbf{r}) \right] \phi_i = \varepsilon_i \phi_i \qquad (2.15)$$

where ϕ_i and ε_i are the single-particle wave-functions and eigenvalues, respectively, such that $\rho(\mathbf{r}) = \sum_i^N \phi(\mathbf{r})^* \phi(\mathbf{r})$. The Eq.2.15, therefore, represents the set of Kohn-Sham self-consistent equations. The solution of this equation start with a initial guess of $\rho(r)$.

Upto now we have done with first two problem through self-consistence solution of the above equation but we still have the third problem of exchange-correlation functional.

2.2.3   Exchange-correlation functional

The exact form of $E_{xc}(\rho)$ is unknown and the challenge in DFT is to approximate this term. This term contain 1) Exchange energy, arises from antisymmetric nature of wavefunction 2) Correlation energy, which contain kinetic term as well as coulomb term(arises from inter-electronic repulsion) and 3) a self-interaction correction. As the form of the exchange-correlation functional are not known, approximations have to be made which makes DFT an approximate theory. There are several approximations to the exchange correlation, namely local density approximation(LDA), generalized gradient approximation (GGA), Meta GGA and Hybrid functionals. In this section we focus in detail on the LDA and GGA.

2.2.3.1 Local density approximation (LDA)

A widely used approximation called the Local Density Approximation (LDA) is to postulate that there exist a exchange correlation energy density and the exchange correlation energy of a point in the space of the system is only related to that electron density at that point. We consider the density is homogeneous over a distance comparable to the inverse fermi vector k. We may approximate the exchange-correlation energy as the summation(integral) of the electron contribution from a volume which depends on the electron density $\rho(r)$.

$$E_{xc} = \int \rho(r)\varepsilon_{xc}[\rho(r)]d^3r \qquad (2.16)$$

From a theoretical point of view, ε_{xc} is parametrized by Hedin and Lundqvist [6]. In some of the work where LDA is applied instead of GGA, the Perdew and Zunger [7] parametrization is employed. LDA is found to be exact for transition metals due to the fact that the electron density varies smoothly. The reason that the LDA is exact is to fulfill the correct sum rule for the exchange correlation hole. The said hole is explained as electrons avoiding each other at a point r, thus obeying the Pauli exclusion principle.

The main deficiency of the LDA was the strong overbinding with bond energies in error by about one electron volt. On the one hand, this rendered LDA useless for most applications in chemistry. On the other hand, the problem was hardly visible in solid state physics where bonds are rarely broken, but rearranged so that errors canceled.

2.2.3.2 Generalized gradient approximation (GGA)

Generalized gradient approximation (GGA) was developed to improve accuracy of LDA. In LDA, the exchange correlation energy density is a function of the local electron density, whereas local variations of the electron density are also important. GGA takes into account the density of the electron and its gradient at each point in the space. several GGA functionals like Perdew-Wang 1991 [8] and Perdew, Burke and Ernzerhof (PBE) [9] are the most popular. It takes a form which includes the gradient density

$$E_{xc} \quad = \quad \int \varepsilon_{xc} f[\rho, \bigtriangledown \rho] \rho(r) d^3 r \qquad (2.17)$$

This equation depends only on the general feature of the real space construction where f is a parametrized analytic function, and $\bigtriangledown$ is the gradient density of the electrons. The equation above is only based on the systems of non-spin electrons. If we consider electrons with different spins, the system exhibits magnetism and now the equation above will take the form of spin densities,

$$E_{xc}[\rho \uparrow, \rho \downarrow] \quad = \quad \int \varepsilon_{xc} f[\rho, \rho, \bigtriangledown \rho \uparrow, \bigtriangledown \rho \downarrow] \rho(r) d^3 r \qquad (2.18)$$

GGA in most cases improves upon the LDA in the description of atoms and solids [10] and it also tends to improve the total energies and atomization energies [11, 12]. The local density approximation (LDA) underestimates the lattice constants by 1% while the GGA overestimates the lattice parameters by 1%. It also reduces the chronic overbinding of the local density approximations [13]. It tends to improve the energy band gap between valence and conduction bands in the cases of semiconductor and insulator materials[114]. The generalized gradient approximation is efficient in computational cost and is numerically accurate and quite reliable.

2.3 The basic methods to calculate electronic structure.

The methods of solving the Kohn-Sham equation and to obtained the eigenvalues and eigenfunctions can be categories in two categories. Methods which are based 1)on k-space approach, 2) Real space approach. For periodic solids, one usually exploits the translational periodicity and handles the solutions in k-space. For finite sized molecules and clusters also, k-space approach is used by constructing super-cell and imposes periodicity artificially in the system.

Regardless of whether it is k-space approach or real-space approach, one has to choose an appropriate basis set to expand the single-particle wave-functions. The choice of basis functions, different schemes, can be broadly grouped into two categories: (*i*) methods using energy independent basis

sets like tight binding method using linear combination of atomic orbitals (LCAO) type basis [14], pseudopotential method using plane wave basis [15], and (*ii*) methods using energy dependent basis set, like cellular method [16], augmented plane wave (APW) method [17] and the Korringa-Kohn-Rostocker (KKR) Green's function method [18], which use partial waves as basis set. In this thesis, we mainly used pseudopotential method with plane wave basis, as implemented in the Vienna *ab initio* simulation package (VASP) [19].

2.3.1 Pseudopotential Method

Pseudopotentials have been introduced to (1) avoid the core electrons explicitly to reduce the computational cost and (2) to avoid the rapid oscillations of the wavefunction near the nucleus, which normally require either complicated or large basis sets. the electrons in the outermost shell of atoms, the so called valence electrons, actively participate in determining the most of the chemical and physical properties of molecules and solids. This leads to the idea behind the pseudopotential theory. Basically in this method for.the valence wavefunctions one constructs pseudo wavefunctions which are identical to the true wave functions outside the augmentation region, which is called core region. From the pseudo wavefunction, a potential can be reconstructed. Here we will develop the basic concept of pseudopotential by a simple transformation of single-particle Kohn-Sham equation (2.15) for an atom where core and valence states are denoted as ψ^c and ψ^v respectively. A new set of single-particle valence states $\tilde{\phi}^v$ can be defined as

$$\psi^v(\mathbf{r}) = \tilde{\phi}^v + \sum_c \alpha_c \psi^c(\mathbf{r}) \tag{2.19}$$

where α_c are determined from the condition that ψ^v and ψ^c are orthogonal to each other *i.e* $\langle \psi^v | \psi^c \rangle = 0$ which gives $\alpha_c = -\langle \psi^c | \tilde{\phi}^v \rangle$. Eqn. (2.15) then can be manipulated, with the help of Eqn. (2.19), to

$$\left[T_S + V_{KS} + \sum_c (\varepsilon^v - \varepsilon^c) | \psi^c \rangle \langle \psi^c | \right] \tilde{\phi}^v = \varepsilon^v \tilde{\phi}^v \tag{2.20}$$

with ε^c as the eigenvalue of the core state. Considering $V_R = \sum_c (\varepsilon^v - \varepsilon^c) | \psi^c \rangle \langle \psi^c |$ which is a repulsive potential operator (as $\varepsilon^v > \varepsilon^c$, making ε^v - ε^c positive), Eqn. (2.20) can be written as

$$[T_S + V_{PS}] \tilde{\phi}^v = \varepsilon^v \tilde{\phi}^v \tag{2.21}$$

The operator

$$V_{PS} = V_{KS} + \sum_c (\varepsilon^v - \varepsilon^c)|\psi^c\rangle\langle\psi^c| \tag{2.22}$$

represents a weak attractive potential, provides the balance between the attractive potential V_{KS} and the repulsive potential V_R, and is called a pseudopotential. While the new states $\tilde{\phi}^v$ obey a single-particle equation with a modified potential, but have the same eigenvalues ε^v as the original valence state ψ^v, are called pseudo-wavefunctions. Through the pseudopotential formulation, we have constructed a new set of valence states, which experience a weaker potential near the atomic nucleus, but the proper ionic potential away from the core region. Since it is this region in which the valence electrons interact to form bonds that hold the solid together, the pseudo-wavefunctions preserve all the important physics relevant to the behavior of the solid.

Since then several methods have been used to generate more accurate as well as more efficient pseudo-potentials.

Good construction of pseudopotential requires a core radius around the outermost maximum of the AE wavefunction, because only then the charge distribution and moments of the AE wavefunctions can be produced by the PS wavefunctions. Therefore, for elements with strongly localized orbitals like first-row, 3d and rare-earth elements, the resulting pseudopotentials require a large plane-wave basis set. To get ride of this problem we can increase the core radius significantly beyond the outermost maximum in the AE wave-function. But this is not a satisfactory solution because the transferability of pseudopotential is always adversely affected when the core radius is increased, and for any new chemical environment, additional tests are required to establish the reliability of such soft PS potentials.

The success of this approach is partly hampered by rather difficult construction of the pseudopotential. Later Blöchl [20] has developed the projector-augmented- wave (PAW) method, which combines idea from the LAPW method with the plane wave pseudopotential approach, and finally turns out computationally elegant, transferable and accurate method for electronic structure calculation of transition metals and oxides. Below we have outlined the idea behind the PAW method.

2.3.2   The Projector-Augmented-Wave Formalism

The draw back of pseudopotential method is the lost information of wavefunctions near nuclei which can influence the calculation of certain properties, such as hyperfine parameters. Another problem is that one don't know when the approximation give reliable results. P. E. Blöchl in 1994, developed the projector-augmented- wave (PAW) method [21], which offers augmented plane wave method as a special case and the plane wave pseudopotential method as a well defined approximation. At the root of the PAW method lies a transformation that maps the true wavefunctions with their complete nodal structure onto auxiliary wavefunctions that are numerically convenient. Later Kresse and Joubert [22] modified this PAW method and implemented it within the plane wave code of VASP.

In this formalism, the AE wavefunction Ψ_n is derived by linear transformation of the PS wavefunction $\tilde{\Psi}_n$.

$$|\Psi_n\rangle = |\tilde{\Psi}_n\rangle + \sum_i \left(|\phi_i\rangle - |\tilde{\phi}_i\rangle \right) \langle \tilde{p}_i | \tilde{\Psi}_n \rangle \tag{2.23}$$

The all electron partial waves ϕ_i are the solutions of the radial Schrödinger equation for the isolated atom. The PS partial waves $\tilde{\phi}_i$ are equivalent to the AE partial waves outside a core radius r_c^l. To meet the boundary condition these two wavefunctions match both in value and slope at the boundary r_c^l. The projector function $\tilde{p}_i$ for each PS partial wave localized within the core radius, obeys the condition $\langle \tilde{p}_i | \tilde{\phi}_j \rangle = \delta_{ij}$. From Eq.2.23, the AE charge density in PAW method can be written as,

$$\rho(\vec{r}) = \tilde{\rho}(\vec{r}) + \rho^1(\vec{r}) - \tilde{\rho}^1(\vec{r}) \tag{2.24}$$

where $\tilde{\rho}$ is the soft pseudo-charge density calculated directly from the pseudo wavefunctions on a plane wave grid. The on-site charge densities ρ^1 and $\tilde{\rho}^1$ are treated on radial support grids localized around each atom. It should be mentioned that the charge density $\tilde{\rho}^1$ is exactly the same as ρ^1 within the augmentation spheres around each atom. In PAW approach, an additional term, called compensation term is added to both auxiliary densities ρ^1 and $\tilde{\rho}^1$ so that the multi-pole moments of the terms $\rho^1 - \tilde{\rho}^1$ in Eq.2.24 vanish. Thus the electrostatic potential due to these terms vanishes outside the augmentation spheres around each atom, just as is accomplished in LAPW method.

2.3.3   The tight-binding method (LCAO method)

One of the standard methods for solving the periodic potential problems met in the theory of the electronic structure is the LCAO(Linear combination of Atomic Orbitals) or bloch or Tight binding method.

The tight-binding Hamiltonian for a periodic system is given by

$$\mathbf{H} \;=\; \sum_{il_1\sigma}\varepsilon_{l_1}a^{\dagger}_{il_1\sigma}a_{il_1\sigma}+\sum_{ij}\sum_{l_1,l_2,\sigma}(t^{l_1l_2}_{ij}a^{\dagger}_{il_1\sigma}a_{jl_2\sigma}+h.c.) \qquad (2.25)$$

where, first term represents the onsite energy term. The second term is hopping term representing hopping of a electron with spin σ from the orbitals labeled l_1 with onsite energies equal to ε_{l_1} in the ith unit cell to those labeled l_2 in the jth unit cell, with the summations l_1 and l_2 running over all the orbitals considered on the atoms in a unit cell, and i and j over all the unit cells in the solid. Thus, orbitals in a solid can be represented by two indices, i and l_1, henceforth referred to as the set (i,l_1). The hopping interaction strength $(t^{l_1l_2}_{ij})$ depends on the nature of the orbitals involved as well as on the geometry of the lattice [14]. The hopping integrals fall off rapidly with distance [23], so, it is sufficient to consider those terms in the Hamiltonian which allow the electron to hop to orbitals on nearest neighbor atoms. Further, since the Hamiltonian is independent of the spin (σ), for the rest of the discussion we can drop the spin indices of the operators. The Hamiltonian can written in the momentum space by a Fourier transformation of the operators given by

$$a^{\dagger}_{il_1} \;=\; \frac{1}{\sqrt{N}}\sum_{k}a^{\dagger}_{kl_1}e^{i\mathbf{k}.\mathbf{r}_{il_1}}$$

so that,

$$\begin{aligned}
\mathbf{H} \;=&\; \sum_{il_1}\varepsilon_{l_1}a^{\dagger}_{il_1}a_{il_1}+\sum_{<ij>}\sum_{l_1,l_2}(t^{l_1l_2}_{ij}a^{\dagger}_{il_1}a_{jl_2}+h.c.)\\
=&\; \frac{1}{N}\sum_{il_1}\sum_{kk'}\varepsilon_{l_1}a^{\dagger}_{kl_1}a_{k'l_1}e^{i\mathbf{k}.\mathbf{r}_{il_1}}e^{-i\mathbf{k'}.\mathbf{r}_{il_1}}\\
&\;+\frac{1}{N}\sum_{<ij>}\sum_{l_1,l_2,k,k'}(t^{l_1l_2}_{ij}a^{\dagger}_{kl_1}a_{k'l_2}e^{i\mathbf{k}.\mathbf{r}_{il_1}}e^{-i\mathbf{k'}.\mathbf{r}_{jl_2}}+h.c.)
\end{aligned}$$

An advantage of this representation is that we can write the Hamiltonian as distinct blocks for each $\mathbf{k}$ value, thereby simplifying the problem. In order to realize this, we first define a set of vectors $\mathbf{R}^{l_1l_2}_{\alpha}$ for the orbital (i,l_1), that connect it to the orbitals (j,l_2) on nearest neighbor atoms, $\mathbf{r}_{jl_2}=\mathbf{r}_{il_1}+\mathbf{R}^{l_1l_2}_{\alpha}$. As a

result of the periodicity of the lattice, the set of vectors $\mathbf{R}_\alpha^{l_1 l_2}$ are the same for every (i, l_1) independent of the unit cell index, i. As the hopping integrals, between orbitals (i, l_1) and (j, l_2) depend only on the vector $\mathbf{R}_\alpha^{l_1 l_2}$ connecting the two orbitals involved, the hopping strength $t_{ij}^{l_1 l_2}$ in the Hamiltonian can be replaced with $t_\alpha^{l_1 l_2}$. Therefore, the Hamiltonian becomes,

$$
\begin{aligned}
\mathbf{H} &= \frac{1}{N} \sum_{il_1} \sum_{kk'} \varepsilon_{l_1} a_{kl_1}^\dagger a_{k'l_1} e^{i\mathbf{k}.\mathbf{r}_{il_1}} e^{-i\mathbf{k}'.\mathbf{r}_{il_1}} \\
&+ \frac{1}{N} \sum_\alpha \sum_{i,l_1,l_2,k,k'} (t_\alpha^{l_1 l_2} a_{kl_1}^\dagger a_{k'l_2} e^{i\mathbf{k}.\mathbf{r}_{il_1}} e^{-i\mathbf{k}'.(\mathbf{r}_{il_1}+\mathbf{R}_\alpha^{l_1 l_2})} + h.c) \\
&= \frac{1}{N} \sum_{il_1} \sum_{kk'} \varepsilon_{l_1} a_{kl_1}^\dagger a_{k'l_1} e_{il_1}^{i(\mathbf{k}-\mathbf{k}').r} + \frac{1}{N} \sum_\alpha \sum_{i,l_1,l_2,k,k'} (t_\alpha^{l_1 l_2} a_{kl_1}^\dagger a_{k'l_2} e^{i(\mathbf{k}-\mathbf{k}').\mathbf{r}_{il_1}} e^{-i\mathbf{k}'.\mathbf{R}_\alpha^{l_1 l_2}} + h.c) \\
&= \sum_{l_1} \sum_{kk'} \varepsilon_{l_1} a_{kl_1}^\dagger a_{k'l_1} \delta(k-k') + \sum_\alpha \sum_{l_1,l_2,k,k'} (t_\alpha^{l_1 l_2} a_{kl_1}^\dagger a_{k'l_2} \delta(k-k') e^{-i\mathbf{k}'.\mathbf{R}_\alpha^{l_1 l_2}} + h.c.) \\
&= \sum_{l_1} \sum_k \varepsilon_{l_1} a_{kl_1}^\dagger a_{kl_1} + \sum_\alpha \sum_{kl_1 l_2} (t_\alpha^{l_1 l_2} a_{kl_1}^\dagger a_{kl_2} e^{-i\mathbf{k}.\mathbf{R}_\alpha^{l_1 l_2}} + h.c.)
\end{aligned}
$$

From the above expression, we can see that the Hamiltonian involves terms connecting different orbitals which may be on the same or on different atoms at a $\mathbf{k}$ point. Thus, the problem reduces to solving the Hamiltonian at each $\mathbf{k}$ point in the Brillouin zone. This has to be performed numerically, with the size of the Hamiltonian matrix equal to the total number of orbitals in the unit cell or sum of all orbitals in each atom in unit cell.

The eigenfunctions of the Hamiltonian, $\mathbf{H}$, can be written as linear combinations of the atomic orbitals, $\phi_j(r)$, located on various atoms of the unit cell, given by,

$$
\Psi_i(r) = \sum_j x_{ij} \phi_j(r)
$$

Löwdin transformation : The different atomic orbitals involved are not necessarily orthogonal to each other, specially which are situated on different atoms. However, since the formalism of second quantization requires an orthogonal basis for the proper definition of fermion creation and annihilation operators and their associated Fock space, the Löwdin transformation [24] has been used to remedies this problem. It transforms the involve orbitals into an orthogonal basis set.

Bibliography

[1] M. Born and J. R. Oppenheimer, "Zur Quantentheorie der Molekeln", Ann. Physik **84**, 457 (1927).

[2] D. R. Hartree, "The wave mechanics of an atom with non-coulombic central field: parts I, II, III", Proc. Cambridge Phil. Soc. **24**, 89, 111, 426 (1928).

[3] V. Fock, "Naherungsmethode zur Losung des quanten-mechanischen Mehrkorperprobleme", Z. Phys. **61**, 126 (1930).

[4] W. Kohn and L. J. Sham, Phys. Rev. **140**, A1133 (1965).

[5] P. Hohenberg and W. Kohn, Phys. Rev. **136**, B864 (1964).

[6] L. Hedin and B. I. Lundqvist. J.Phys.C, **4**, 2064 (1971).

[7] . Perdew and A. Zunger. Phys.Rev.B, **23**, 5048 (1981).

[8] J.P. Perdew and Y. Wang, Phys. Rev. B **45**, 13244 (1992).

[9] J. P. Perdew, K. Burke, and M. Ernzerhof, Phys. Rev. Lett. **77**, 3865 (1996).

[10] J. Perdew, K. Burke, and M. Ernzerhof. Phys. Rev. Lett, **77**, 18 (1996).

[11] Y. Zhang and W. Yang. Phys. Rev. Lett, **80**, 890 (1998).

[12] B. Hammer, L. B. Hansen, and J. K. Norskov. Phys. Rev. B, **59**, 7413 (1999).

[13] Z. Wu and R. E Cohen. Phys. Rev. B, **73**, 235116, (2006).

[14] J. C. Slater and G. F. Koster, Phys. Rev. **94**, 1498 (1954).

[15] J. C. Phillips and L. Kleinman, Phys. Rev. **116**, 287 (1959).

[16] E. P. Wigner and F. Seitz, Phys. Rev. **46**, 509 (1934).

[17] T. L. Loucks, *Augmented Plane Wave Methods*, (Benjamin, New York, 1967).

[18] J. Korringa, Physica **13**, 392 (1947); J. Korringa, Phys. Rev. **238**, 341 (1994).

[19] G. Kresse and J. Hafner, Phys. Rev. B **47**, 558 (1993); G. Kresse and J. Furthmuller, Phys. Rev. B **54**, 11169 (1996)

[20] P. E. Blöchl, Phys. Rev. B **50**, 17953 (1994).

[21] P. E. Blochl. Projector augmented-wave method. Physical Review B, 50(24):1795317979, Dec 1994.

[22] G. Kresse and D. Joubert, Phys. Rev. B 59, 1758 (1999).

[23] Walter A. Harrison, *Electronic Structure and Properties of Solids* (Dover, 1989).

[24] Per-Olov Löwdin, J. Chem. Phys. **18**, 365 (1950).

Chapter 3

$K_2Cr_8O_{16}$: electronic structure

3.1 Introduction

Correlation effects in transition metal oxides play an important role in modifying their properties. The undoped $3d$ transition metal oxides are examples of strongly correlated systems and they are usually insulators [1]. Metallicity and Ferromagetism in these oxides are rare with most of them exhibiting either antiferromagnetic or ferrimagnetic ordering. Few special conditions must be satisfied to stabilize ferromagnetism and metallicity in these oxides. A well known $3d$ oxide used for magnetic recording, CrO_2 is an example of ferromagnetic metal. In this compound Cr is in its formal valence Cr^{4+} and the simple picture of strongly correlated systems suggests an insulating ground state [2]. The mechanism of ferromagnetism is believed to be of double exchange type arising from the presence of both localized and itinerant d electrons [3]. It is an example of negative charge transfer system. In this compound the d-bands split into two parts one below fermi surface which is localized and another which is spread on both sides of the fermi energy, represents the itinerant electrons, hybridized strongly with O-p states. This minimizes the effective correlation and results in a metallic ground state. However, the double exchange mechanism and its variants, used to explain ferromagnetism in the oxides require/imply metallicity. So, the ferromagnetic insulators are even more rare and when one finds such $3d$ compounds, one has to look for some other mechanism to explain the ground state in these oxides.

51

One such example is of $K_2Cr_8O_{16}$ in which experiments reported it to be a ferromagnetic insulator [4]. Experimentally they found a transition into a low temperature ferromagnetic insulating phase at 90 K, though the paramagnetic to ferromagnetic transition takes place at 180 K. This compound could be viewed as the 25% K doped analogue of a polymorph of CrO_2. Thus one has the surprising result that introducing a non-integral number of 0.25 electrons per CrO_2 structural motif gives us an insulating state, which in addition is also ferromagnetic.

As both aspects are unexpected, the first question that comes to mind, is whether we are working in the realm of experimental uncertainties, and the stochiometric compound is indeed metallic. Then the consequent ferromagnetism is not a puzzle any more. Recent first principle calculations [5] have examined the electronic and magnetic properties of this compound. In contrast to experiments [4], they find that the ground state is a half metallic ferromagnet with the fermi level crossing the majority spin band, while the down spin band has a semiconducting gap. They have examined the formation of an incommensurate long wavelength charge density wave and they do find two parallel one-dimensional fermi surfaces. Calculation of the non-interacting susceptibility reveals a maximum at q_z^* of $0.295 * \pi/c$ and $1.705 * \pi/c$ with some deviations as a function of q_x and q_y, consistent with the possibility of the formation of an incommensurate charge density wave. Experimental work must examine whether the broadening of the nesting vector is small enough to still allow this scenario to be realized. There are reports of analogous compounds in the literature. $K_2V_8O_{16}$ [6] has been found to have an analogous structure. It exhibits a similar transition from a low temperature insulating phase to a high temperature metallic phase. However, here the insulating state is antiferromagnetic. $Rb_2Cr_8O_{16}$ [6] has been found to be semiconducting with a T_c found to be 90 K higher than the K doped counterpart.

$K_2Cr_8O_{16}$ belongs to a family of oxides called hollandites [4]. These represent a family of compounds with the general formula $A_2B_8O_{16}$ where A represents univalent, large tunnel ions such as Na, K, Ba, Sr, Rb and Cs and B represents a trivalent or tetravalent cations in a oxygen octahedron such as Mn, Ti, Al, Cr, V and Si. The basic network of the Cr octahedra has been shown in Fig.3.1a. One unit cell, shown by solid line, consists of eight such octahedra which forms a tunnel in which the K ion is situated. The tunnel is enclosed of two planes of Cr atoms in one unit cell. Any Cr atom of the top

plane has as its neighbors two Cr atoms from the lower plane. Of the two Cr atoms, one is linked to the Cr of the top plane through an edge-shared oxygen octahedron, while the other is through a corner shared oxygen octahedron. As a result the distance between one pair of Cr atoms is 2.92 Å, while that between the other is 3.42 Å respectively. Thus, the structure consists of one-dimensional zig-zag chains of Cr-O networks running in the z-direction connected to each other by a bridging oxygen(O2) as shown in Fig.3.1. This was probably what motivated the scenario of a fermi surface nesting driven charge density wave hypothesis. The entire central portion of the structure is like a tunnel running in the z-direction and this is where the K atoms reside.
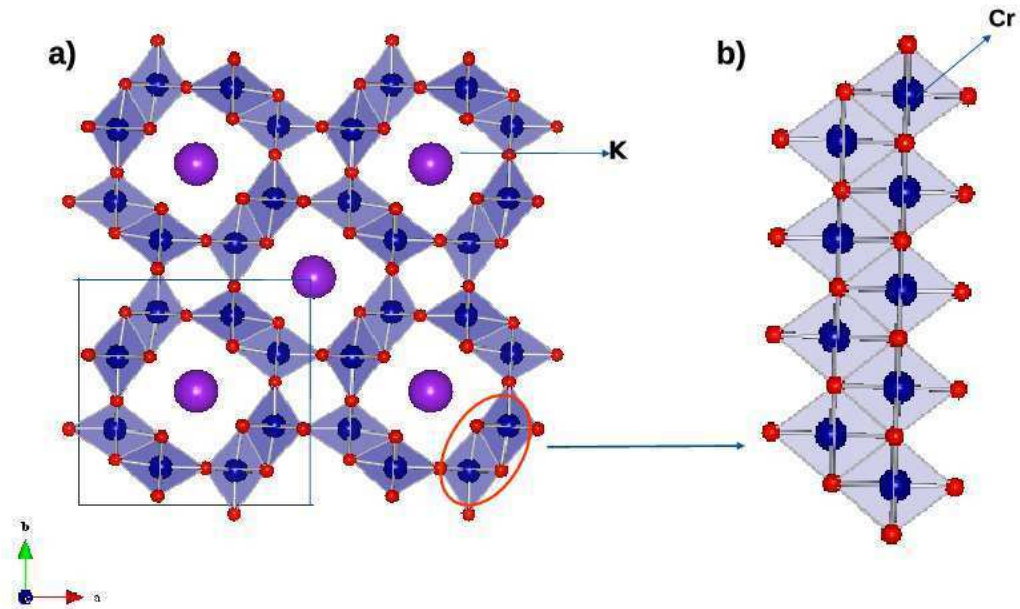
Figure 3.1 The network of Cr atoms (a) in the z=0 plane z=0.5 in the xy plane unit cell has been shown within solid lines. (b) Connection of two nearest Cr ions along Z direction has been shown.

3.2 Methodology

In view of the problems in interpretation, we examined the problem with a slightly different approach than considered by Sakamaki *et. al.* [5]. In usual x-ray diffraction experiments it is difficult to determine the oxygen positions accurately especially if large unit cells are involved. We carried out first principle electronic structure calculations starting with the experimental reported structure, but allowing for structural relaxations. In this relaxations, we varied the positions of different atoms keeping the volume of cell constant and minimizing the total energy. We have simulated the XRD pattern for the experimental tetragonal structure as well as the relaxed structure by using "Powder cell 2.3". Both are almost identical which satisfies the observation that determining the oxygen positions from X-ray diffraction alone is very difficult.

We have carried out first principle electronic structure calculations for K$_2$Cr$_8$O$_{16}$ within a plane wave pseudo potential implementation of density functional theory using PAW potentials [7]within VASP [8]. The generalized gradient approximation (GGA) [9] was used for the exchange and electron correlations were considered by including a Hubbard U of 4 eV on Cr (unless otherwise stated) within the GGA+U formalism [10]. Calculations in the absence of U were also performed for comparison. The self-consistency was performed with a Monk-horst pack k-points grid of 4X4X4. We started the calculations with the experimentally reported structure [4], although we allowed for atomic relaxations to find the minimum energy configuration. A cutoff energy of 400 eV was used for the plane wave basis states. In addition to the ferromagnetic arrangement of spins on the Cr site, we also considered various possible antiferromagnetic arrangements for the unit cell. We have shown two of them which are close in energy to the ferromagnetic in Fig.3.4(a) and 3.4(b) to examine if alternate magnetic arrangements have lower energy. The density of states were calculated using the tetrahedron method, considering spheres of radii of 2.3, 1.3 and 0.8 for K, Cr and O respectively.
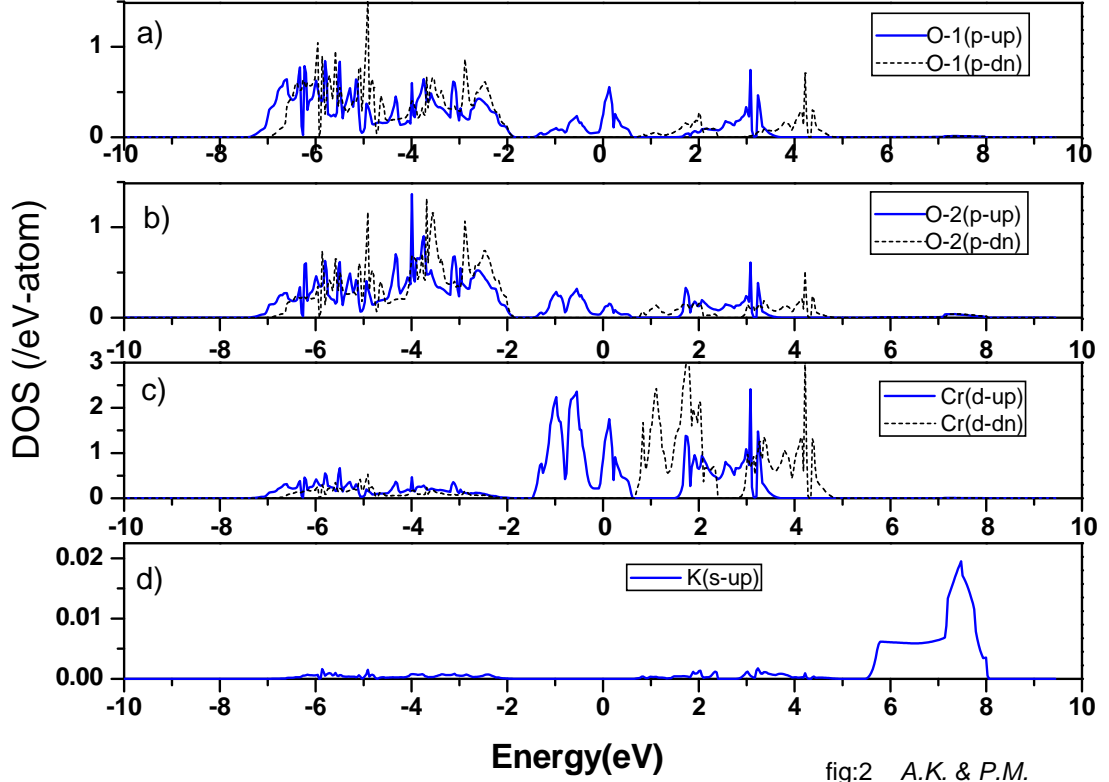
Figure 3.2 The calculated atom and spin projected partial density of states for (a) O1 *p*, (b) O2 *p*, (c) Cr *d* and (d) K *s* for *U*=0. Zero of energy corresponds to the Fermi energy.

3.3   Results and discussion

We first examined the electronic structure in the absence of a Hubbard *U* on Cr. The atom projected partial density of states for the relaxed structure for a ferromagnetic arrangement of spins on Cr is given in Fig.3.2. The optimized (experimental) inequivalent Cr-O bond-lengths are 1.88(1.87), 1.90(1.91), 1.93(1.93) and 1.97(1.97) Å. The system is found to be half-metallic in our calculations, consistent with the earlier theoretical work [5] but inconsistent with experiments [4]. Examining the density of states we find that the K atoms contributes in the energy interval 6-8 eV above the fermi level. At the fermi level(zero of the energy axis) one has primarily states with Cr *d* states with t_{2g} symmetry with significant O *p* admixture. Hence the doped electrons go on to occupy the Cr *d* states of t_{2g} symmetry.
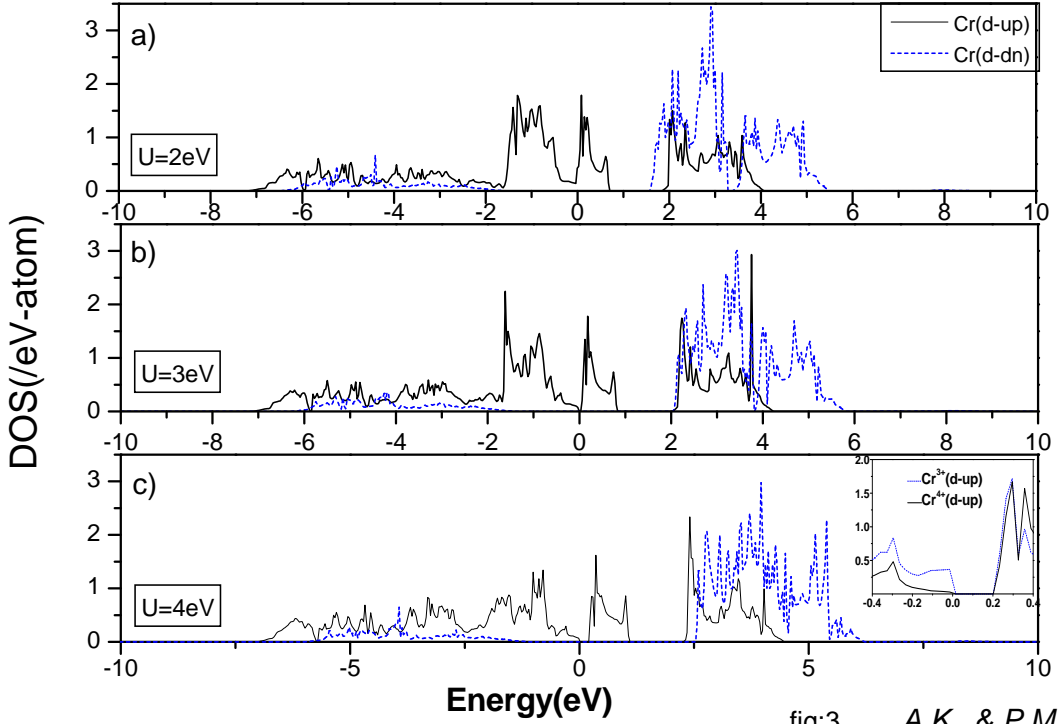
Figure 3.3 The calculated Cr^{3+} d spin projected partial density of states for (a) U=2 eV, (b)U=3 eV, and (c) U=4 eV with the optimized crystal structure of the U=4 eV calculation assumed. Zero of energy corresponds to the Fermi energy. The near fermi energy region of the up spin Cr^{3+} and Cr^{4+} partial density of states is shown in the inset of panel (c).

The states with e_g symmetry are found around 3 eV higher. In addition one finds an exchange splitting of $\sim$ 1 eV of the Cr d states. In order to examine how one-dimensional this system is, we have also plotted the contributions from the two types of oxygen in the unit cell. O1 represents the oxygens which are edge shared between neighboring CrO$_6$ octahedra, while O2 represents oxygens that are corner shared. As is evident from the earlier discussion, O2 connect the zig-zag Cr chains running in the z-direction. There is a significant contribution of O2 p states in the same energy window as the Cr d character.

After this we have applied electron correlation on the Cr d states, removed all symmetry constraints and optimized the structure. With an improved treatment of electron correlation effects at the Cr site,
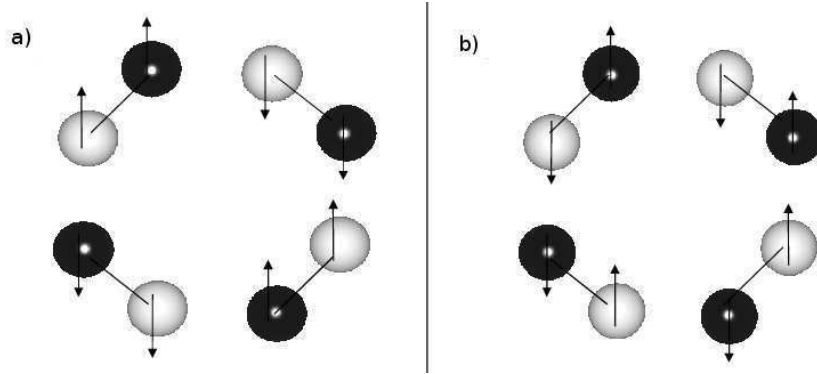
Figure 3.4 The spin arrangements in one unit cell for (a) AFM1 and (b) AFM2 .

included within the framework of GGA+U calculations [10], the system is insulating (Fig.3.3(c)). The eight Cr sites present in the unit cell, now become inequivalent with the charge being localized on two Cr atoms, than being equally distributed. This is evident from the inset of Fig.3.3(c), where one finds that charge is depleted from one Cr site labeled as Cr^{4+} and added to the ones labeled as Cr^{3+}. This charge ordering transition is initiated by a structural distortion of the CrO_6 octahedra with the bond-lengths being 1.96Å for the Cr^{3+} atom. The Cr^{4+} atom has shorter bondlengths, equal to 1.93Å with oxygen. The charge difference between the Cr^{3+} and Cr^{4+} sites is however only 0.18 electrons in the up spin channel, a much smaller value than the integral valence change expected at the purely ionic limit. A much smaller than integral valence change has been observed before in other charge ordered systems [11]. The earlier theoretical work [5] did not allow for structural relaxations and hence could not find the insulating state in their calculations. The structural distortions localize the electron at some Cr sites over others. However, they are not enough to drive the system insulating. Freezing the structure of the system to that obtained by relaxations for a *U* of 4 eV, we find that, as we vary *U* from 2 to 4 eV in steps of 1 eV, the system becomes insulating at around 3 eV. Thus structural distortions in addition to electron correlation effects drive the charge ordering transition here.

Earlier, in the context of other systems with large unit cells and low symmetry, it has been observed that it is difficult to get good refinements of the oxygen positions from x-ray diffraction alone [12]. We hope that the current work would motivate further experiments on this interesting compound. A real space view of the charge density corresponding to the states found in the energy window -0.5 eV to

Table 3.1 Energies in eV per formula unit for different magnetic configurations

Configuration	U = 0	U = 4 eV
Ferromagnetic	0	0
AFM1	0.964	0.924
AFM2	0.618	0.526

E_F in the calculation performed for U=4 eV are shown in Fig.3.5. This has been plotted for the z=0.5 and z=0 plane. The Cr^{3+} as well as Cr^{4+} atoms are identified in addition to the bridging oxygens O1 and O2, both of which are found to interact quite strongly with Cr. The nesting driven charge density wave scenario seems less likely and a combination of electronic and ionic effects are responsible for the charge ordering transition as in several other examples [13].
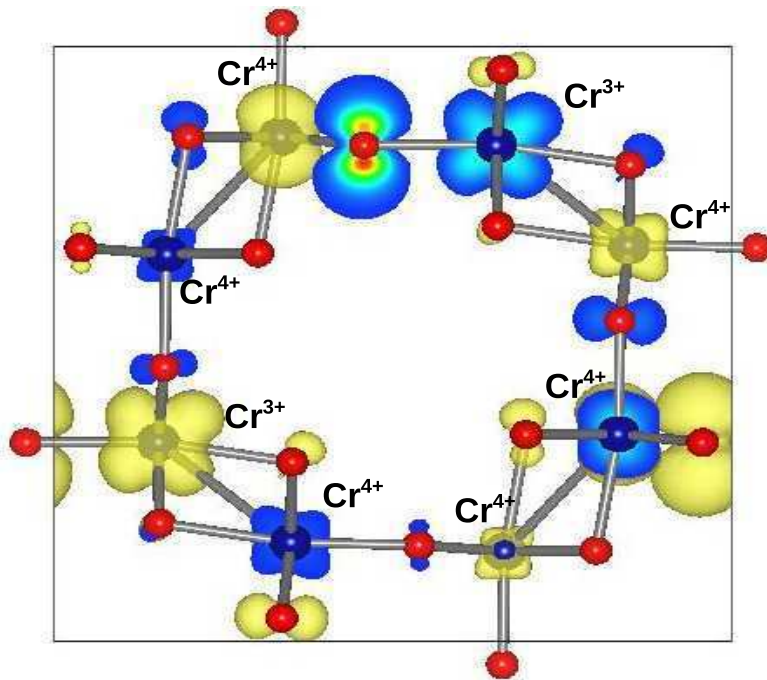
Figure 3.5 The calculated charge density of the feature between -0.5 eV and the fermi energy has been plotted. The Cr^{3+} and Cr^{4+} ions have been indicated.
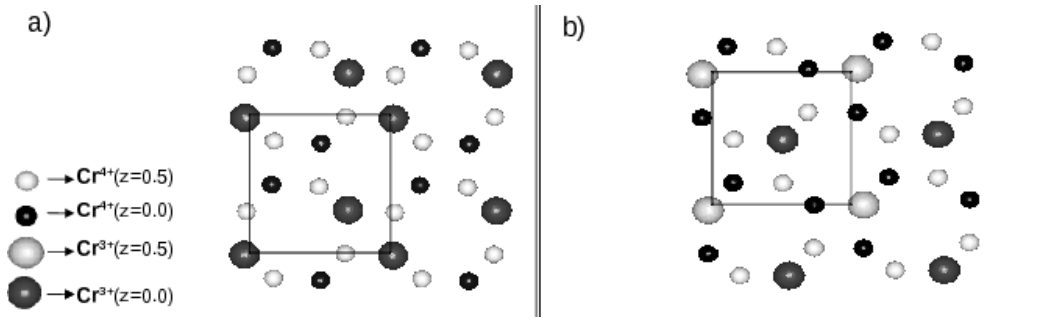
Figure 3.6 The network of Cr^{3+} and Cr^{4+} atoms in the z=0 and 0.5 planes for (a) farthest Cr^{3+} atoms and (b) observed arrangement of Cr^{3+} atoms in the unit cell.

The next question we asked was where does the energy gain come from for localizing the electrons when it would seem natural that delocalized electrons would have lower energy. One source of the energy gain comes by minimizing the repulsive electrostatic energy. Placing the two electrons donated by K on two Cr atoms farthest in the unit cell at a separation of 7.58 Å, we find, is not energetically the lowest energy configuration. This is evident from a view of the Cr network shown for the z=0 and z=0.5 planes in Fig.3.6. Taking the full periodicity of the unit cell, this configuration leads to cases where the Cr^{3+} atoms are separated by just 4.4 Å. Instead it is more favorable to place the Cr^{3+} atoms at a separation of 7.05 Å (Fig.3.6(b)). Another contribution to the energy gain comes from the intraatomic exchange interaction(Hund's exchange) obtained when one has increased localization of an electron at an atomic site.

The entire discussion till now has ignored the magnetism of the underlying lattice. Should ferromagnetism still be favored in the insulating state? The structural distortion that we find in the presence of U, reduces all point group representations to contain only a representations. A schematic representation of antibonding levels for $Cr^{+3.75}$, Cr^{+3} and Cr^{+4} arising from Cr d-O p interactions has been shown in Fig.3.7. The variation of Δ(difference between the highest occupied level of Cr^{3+} and the lowest unoccupied level of Cr^{+4}) with interaction strength $pd\pi$ is shown in upper panel of Fig.3.7. The onsite energies of Cr^{3+} and Cr^{4+} are not identical because of the accompanying structural distortion of the CrO_6 octahedra.

Considering just the highest t_{2g} orbital on Cr^{3+} and Cr^{4+} sites, the left and right-most panels of
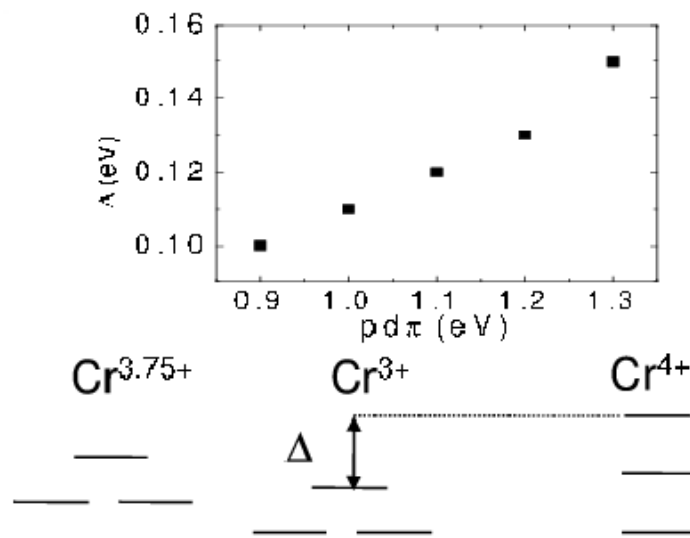
Figure 3.7 A schematic level diagram of the splitting of the partially occupied t_{2g} orbitals on Cr^{3+} and Cr^{4+} has been shown. Variation of δ with intraction strength has also been shown.
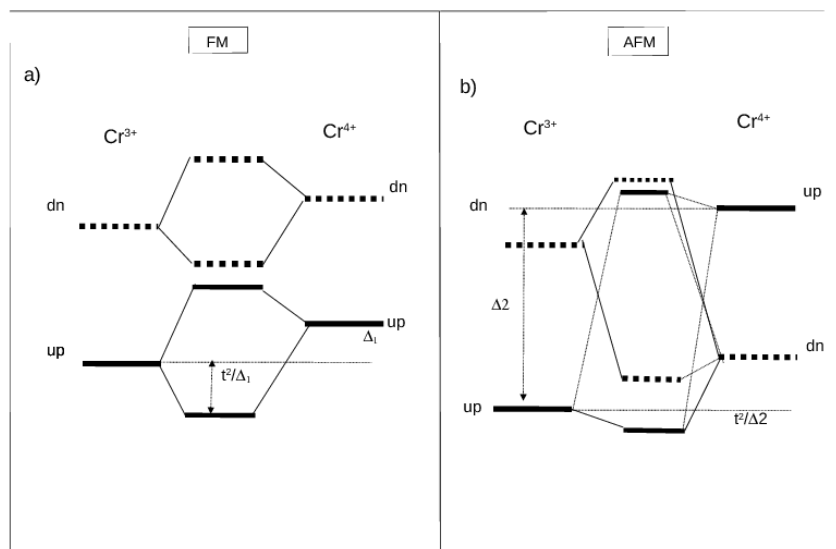
Figure 3.8 The energy level diagram for the levels formed by the interaction of Cr^{3+} and Cr^{4+} atoms in (a) FM and (b) AFM arrangements.

Fig.3.8(a) and 3.8(b) show the exchange split levels on both atoms. As a result of hopping interaction, these levels interact forming bonding and antibonding levels and the central panel represents the level ordering after the interaction for a ferromagnetic (Fig.3.8(a)) and an antiferromagnetic(Fig.3.8(b)) arrangement of spins. There is just one electron in these levels, and so ferromagnetism wins. This is consistent with our calculated results for competing magnetic configurations Table:3.1. We note that the undistorted lattice without charge ordering leads to a ferromagnetic metallic ground state, in contrast to the experimental results; the magnetism in such cases would be driven by the double exchange or a Stoner-type mechanism. On the other hand, the magnetism in the insulating state is derived from the ferromagnetic superexchange interaction, as explained above. This brings us to the experimental claim in Ref. 5, suggesting the existence of a metal-insulator transition (MIT) at $\sim$ 95 K, while the ferromagnetic order sets in at a considerably higher temperature ($\sim$ 180 K). This would require the ferromagnetic metallic state for 95 K $<$ T $<$ 180 K to have an origin other than the one proposed here, based on the charge-ordered insulating state. In this context, it is interesting to note that there is absolutely no reflection of the "MIT" at 95 K in the magnetization data (Fig. 1 in Ref. 5), suggesting that the nature and the origin of the ferromagnetic order is the same above and below 95 K. In order to resolve this puzzle, we had a closer look at the resistivity data as a function of the temperature (Fig. 3 in Ref. 5) by magnifying the figure and digitizing the data points. While the data resolution in the reported figure is not of sufficient quality to discuss T $>$ 230 K regime, we find that for T $<$ 230 K, the resistivity, $\rho(T)$, monotonically increases with decreasing T, suggesting an insulating state for all T less than 230 K and in particular, at the magnetic ordering temperature of 180 K. In order to understand transport properties further, we analyzed the resistivity data in terms of simple models and found that the low temperature ($<$ 50 K) resistivity is well-described by variable-range hopping (VRH); this is commonly found in the case of many oxides arising from oxygen vacancies introducing states in the mid-gap region. The higher temperature ($>$ 100 K) range is easily described as an inhomogeneous system with a macroscopic insulating state with small metallic impurities, presumably arising from CrO_2, as reported in Ref. [4]. The bandgap of the insulating phase is found to be about 54 meV.

This is in good agreement with our electronic structure calculation with U = 4 eV, exhibiting a
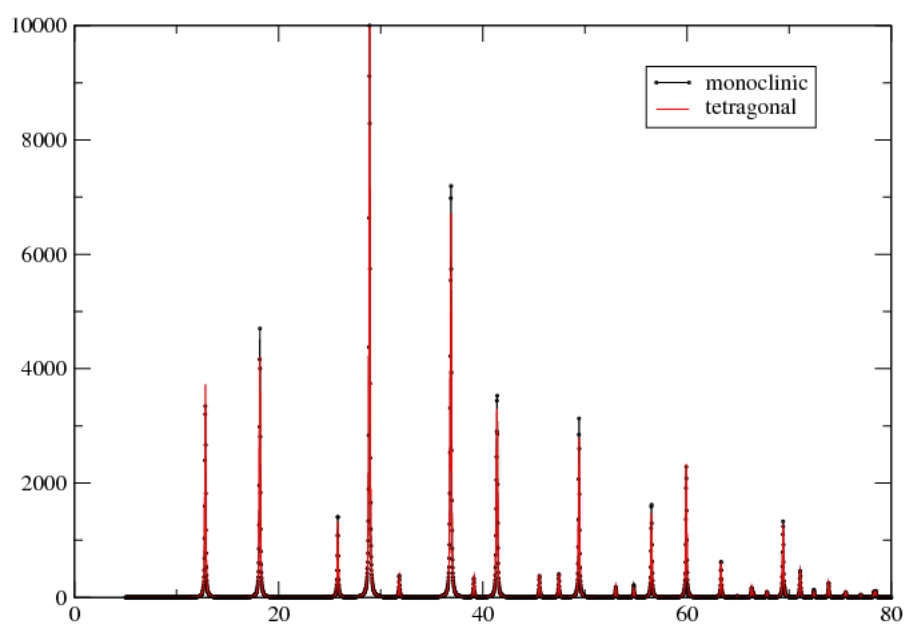
Figure 3.9 Comparison of simulated XRD pattern for both experimental(tetragonal) and relaxed(monoclinic) structures

bandgap of ~ 160 meV (see the inset to Fig.3.3c). In fact, a combination of these two models, one for the low T regime and the other for the high T regime, is able to describe almost all part of the transport data well, indicating the macroscopic system to be a gaped insulator with low density of in-gap states arising from inevitable oxygen vacancies with some clusters of metallic impurity. It appears that there is a slightly more rapid change in the transport data around 95 K, as already noted in ref. 5, but the small deviation from the above-mentioned model description of transport in this system would suggest that this is most likely due to a minority phase and is not an intrinsic property of the stochiometric compound, thereby establishing a charge-ordered, insulating ferromagnet in a nominally fractionally doped transition metal oxide.

In this work, we have studied a class of systems where doping of electrons leads to the localization of electrons on two of the eight equivalent Cr atoms present in the unit cell. Analysis of our results reveal that the energy gain for the charge ordering comes from considerations of minimizing the electrostatic interaction between charges, increased intraatomic exchange contribution due to a localization of the charge and the structural distortions accompanying the charge ordering transition that allow levels on neighboring atoms to couple via hopping. This charge ordering transition also allows the ferromagnetic state to be stabilized even in an insulator.

Bibliography

[1] Masatoshi Imada, Atsushi Fujimori, and Yoshinori Tokura, Rev. Mod. Phys. **70**, 1039 (1998).

[2] B.L. Chamberland, CRC Crit. Rev.Solid State Sci. **7**,1(1977)

[3] M.A.Korotin, V.I. Anisimov, D.I. Khomskii, G. A. Sawatzky, PRL **80**, 4305(1998)

[4] Kunihiro Hasegawa et. al. PRL **103**, 146403(2009)

[5] M. Sakamaki et. al. Phys. Rev. B **80**, 024416(2009)

[6] H. Okada, N. Kinomura, S. Kume and M. Koizumi, Mat. Res. Bull. **13**, 1047(1978)

[7] G. Kresse, and J. Joubert,Phys. Rev. B **59**, 1758 (1999).

[8] G. Kresse, and J. Furthm*ü*ller, Phys. Rev. B. **54**, 11169 (1996); G. Kresse, and J. Furthm*ü*ller, Comput. Mat. Sci. **6**, 15 (1996).

[9] J. P. Perdew, Y. Wang Phys. Rev. B. **45**, 13244(1992)

[10] S.L. Dudarev et.al. Phy. Rev. B. **57**, 1505(1998)

[11] S. Larochelle *et al.*, Phys. Rev. Lett. **87**, 095502 (2001); P. Mahadevan, K. Terakura and D.D. Sarma, **87**, 66404 (2001).

[12] S. Larochelle *et al.*, Phys. Rev. Lett. **87**, 95502 (2001); P. Mahadevan, K. Terakura and D.D. Sarma, **87**, 66404 (2001).

[13] M.D. Johannes and I.I. Mazin, Phys. Rev. B **77**, 165135 (2008).

Chapter 4

A microscopic model for $K_2Cr_8O_{16}$

4.1 Introduction

$K_2Cr_8O_{16}$ is an example of an unusual hollandite which exhibits ferromagnetism in the insulating state. Another aspect is that the magnetic ordering temperature(T_c=180K) is higher than its metal-insulator temperature(T_c=95K) [1]. As a result one has the insulating state developing in the already ferromagnetic state. This is different from the usual insulating ferromagnets where magnetism develops in the already insulating state. In previous chapter we have shown that the insulating state of $K_2Cr_8O_{16}$ arises from a charge ordering transition [2]. Potassium acts like a donor and the doped electrons prefer to occupy two Cr sites, instead of being equally distributing among all the 8 Cr ions, the choice being dictated by minimizing their electrostatic energy. The localization of the electron at a Cr site is brought about by a polaronic distortion which leads to an elongation of one of the Cr-O bonds associated with a CrO_6 octahedra. The earlier experiments [1] did not detect any structural change in the compound during M-I transition but, a recent more precise experimental work by Toriyama *et. al.* [4] found a $\sqrt{2} \times \sqrt{2} \times 1$ super lattice formation in the insulating phase [4]. They also found symmetry lowering from I4/m to P112$_1$/a. The structural change involved a lattice dimerization, leading to tetramer formation of crystallographically four different Cr ions connected by corner shared oxygens. They suggest that this tetramerization brings the gap and results in an insulating ground state. Therefore a Peierls-like

transition is responsible for the insulating ground state. The ensuring ferromagnetism in the system is described within the double exchange mechanism by Nishimoto *et. al.* [3] using a density matrix renormalization group method. As our analysis were based on ab-initio calculations which does not provide the microscopic consideration responsible for the changes in the electronic structure, we decided to carry out an analysis of the result in terms of a multiband Hubbard Hamiltonian whose tight-binding part was determined by fitting the ab-initio band structure.

4.2 Methodology

The electronic structure of $K_2Cr_8O_{16}$ has been studied within a plane wave implementation of density functional theory in VASP [6]. PAW [5] potentials were used in addition to the GGA approximation [7] for the exchange. Electron correlation effects were included within the GGA+U approximation using the scheme of Dudarev *et. al.* [8].It has a body centered tetragonal unit cell with 26 ions with (lattice constants a=b=9.7627, c=2.934). We have worked with a primitive unit cell with 13 ions per unit cell. The gamma-centered grid of $6 \times 6 \times 6$ has been used for our calculations. Energy cut off for the calculations is 400.0 eV. This experimental structure reported earlier will be referred as non charge-ordered structure from now. The charge ordered solution for this structure, which was described in the previous chapter, will be referred as charge ordered(small) structure.

The recently reported structure by Toriyama *et. al.* with tetramerization will be referred to as the experimental structure from now on. At first we started the calculations with the recent experimentally reported structure. The positions were optimized and the energy and other properties of this optimized experimental structure were studied. The possibility of mixed valency at the Cr site suggested that there might be charge ordered solutions possible. In order to examine for that we broke the symmetry of the initial structure and searched for charge ordered solutions. We have used U=4eV and relaxed the structure. A charge ordered insulating state was obtained as the ground state. In order to discuss changes in the electronic and magnetic structure between the charge ordered state and the experimental structure, spheres of radii 2.3,1.3 and 0.8 for K, Cr and O respectively were constructed about the atoms.

Magnetic moments, charge and the partial density of states were evaluated within these spheres. There are small changes in positions of ions with respect to those reported in the literature. An examination of the Cr-O bond-lengths reveals that the changes are primarily associated with a specific bond-length.

In the previous work [2] we have analyzed our ab-initio results and presented a model to capture our results. In this work we have gone a step forward and constructed a microscopic model to describe what are the different mechanisms responsible for MI transition in the compound. For that we have constructed a basis consisting of Cr-d and O-p with their radial part described by maximally localized wannier functions. This is done using the WANNIER90VASP interface [9–11] for extracting on site energies given and various interaction strengths, to see what are the changes in these microscopic parameters which make the system insulating.

We have also carried out Hartree-Fock calculations for the experimental P112$_1$/a structure which has just the tetramerization and we contrast the results with those of our theoretically optimized structure. We have used a home built code for these calculations. We have calculated the density of states by using the tetrahedron method. $8 \times 8 \times 8$ K points grid has been used for these calculations. The initial parameters were taken from non magnetic calculations at U=0eV.

4.3   Result and Discussion

In the previous chapter we have shown that K in this compound acts as a perfect donor. The extra electron donated by K prefers few of the Cr sites over others which leads to charge disproportionation. The high temperature structure for the metallic phase has all Cr sites equivalent. A comparison of the bond-lengths reveals that one of the Cr-O distances has changed for the Cr sites in the charge ordered structure resulting in four inequivalent Cr sites in the 26 atom unit cell as shown in Fig.4.1. It should be noted that the charge difference between the sites is very small and the charge ordering reflects in the magnetic moments shown in Table.4.1.

The different colors represent the inequivalent sites. Red, purple, orange and blue colored spheres in Fig.4.1 represents Cr1, Cr2, C3 and Cr4 respectively. We have called Cr2 as Cr^{3+} which has the
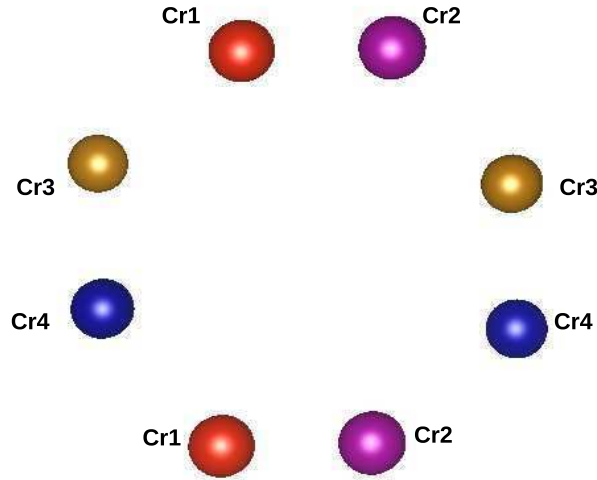
Figure 4.1 The different Cr sites withing small unit cell. The four colors represents four inequivalent Cr sites.

Cr sites	Magnetic Moments at U=4eV(μ_B)
Cr1	2.447
Cr2	2.718
Cr3	2.578
Cr4	2.469

Table 4.1 Magnetic moments for different Cr sites at U=4eV.

highest magnetic moment within our calculations and all other Cr sites as Cr^{4+} in our previous studies. The polaronic distortion as well as electron-electron interactions stabilize the charge-ordered state. The ab-initio results have been mapped on to a tight binding model which includes both Cr-d and O-p states in the basis. The analysis supplements the ab-initio results and helps us to understand the opening up of the gap under different conditions. The comparison between the calculated band dispersions obtained from ab-initio(VASP) and the microscopic model are shown in Fig.4.2. The onsite energies for both non charge-ordered and charge-ordered structures are given in Table.4.2. The four inequivalent sites of Cr are named as Cr1, Cr2, Cr3 and Cr4 in the table. We have given the onsite energies for two values

of U to see the effect of U on charge disproportionation. We first examine the energy level diagram for the non charge-ordered structure. One can easily distinguish between the levels with t_{2g} symmetry and those with e_g symmetry, as these are well separated in energy. Additional distortions lift the degeneracy within the t_{2g} and e_g manifold also. The level ordering remains unchanged as U is decreased from 4eV to 3eV. The extra electrons from K will be equally distributed among all the Cr sites resulting in a metallic ground state.

There are large changes in the onsite energies when one goes from the non charge-ordered structure to the charge-ordered structure. The lowest two levels of each of the Cr sites are occupied similar to the non charge-ordered structure. The energies of the third levels of the Cr sites are changed and are different for each of the Cr sites. Here we find the localization of the electron at site Cr2 is energetically more favorable as we had earlier observed from an analysis of the ab-initio results. The polaronic distortion which we found from our structural optimization is responsible for the opening up of a gap between the third energy level of Cr2 and the third energy level of the other Cr sites and hence one finds charge ordering. To see the effect of U, we have done the similar analysis for U=3eV for the same structure. The reduction of the gap between the third level of Cr2 and third level of other Cr sites shows that electron correlation U stabilizes the localization of the electrons at some Cr sites. However, the difference in the onsite energies for the third highest level suggests that even at this value of U one still has charge ordering.

There are several Cr-O bondlengths in the problem and so we extracted the interaction strength $pd\pi$ from the $p-d$ mapped model for different bond-lengths. We have plotted these interaction strengths as a function of bondlengths shown in Fig.4.3 and fitted it with Harrison's empirical law for scaling of hopping interaction strengths with bondlength. For pd interactions, the scaling is expected to scale with distance r, as $1/r^4$. The fitted value of the exponent is $\sim$ -3.85 which is in good agreement with the empirical HarrisonâĂŹs law.

Recently, X-ray absorption spectroscopy studies probing the Cr-$L_{2,3}$ edge by P.Bhobe *et.al.* [12] found signature of both Cr^{3+} and Cr^{4+} features in the spectrum, supporting the view of charge ordering. Now, let us examine the recent structure proposed by Toriyama *et.al.* [4]. They found this structural

Value of U(eV)	Onsite energies(in eV)				
	Non Charge-ordered	Charge ordered			
	Cr	Cr1	Cr2	Cr3	Cr4
4eV	3.595	3.397	3.958	3.590	3.435
	3.469	3.261	3.828	3.430	3.280
	1.416	1.667	0.856	1.315	1.840
	0.060	-0.132	0.540	0.034	-0.202
	-0.130	-0.313	0.166	-0.174	-0.269
3eV	3.572	3.499	3.741	3.561	3.552
	3.488	3.414	3.615	3.443	3.437
	1.542	1.605	1.243	1.446	1.779
	0.598	0.526	0.850	0.597	0.462
	0.398	0.315	0.545	0.359	0.363

Table 4.2 On-site energies of Cr sites for Charge disordered and Charge ordered(small) structure from wannier calculations.
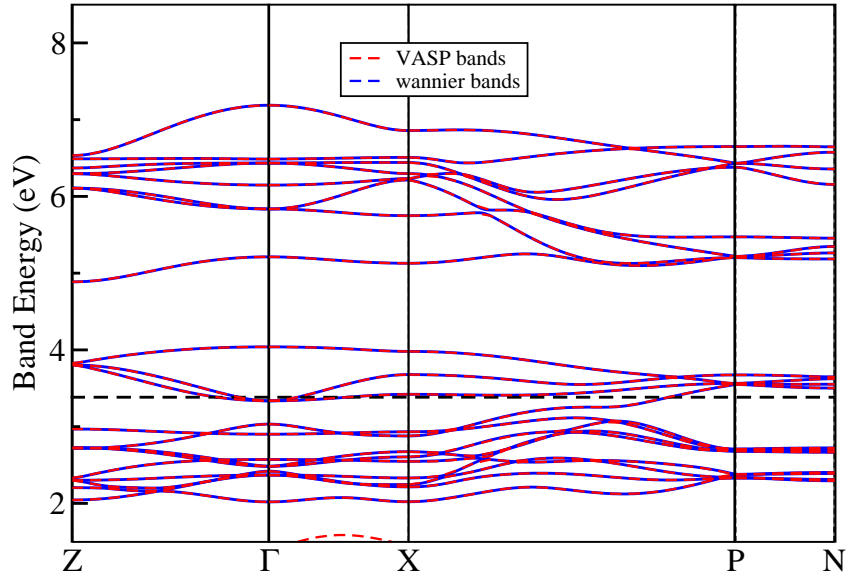
Figure 4.2 Band dispersion comparison.

transition to take place at the metal to insulator transition temperature in the compound going. They have done synchrotron X-ray diffraction experiments on single crystal. They found reflection of $\sqrt{2} \times \sqrt{2} \times 1$ super structure formation in the experiments. The unit cell for the insulating phase has been shown in Fig.4.4. We have also shown the unit cell for the metallic phase with dashed lines. The structural changes can be explained by the formation of tetramers within the units formed by four Cr ions connected via corner shared oxygens as shown in Fig.4.5. We have shown only the Cr network within the unit cell in Fig.4.5. The corner shared Cr ions are shown as a square like structure which has been encircled by a red line.

These are the units which are getting tetramerized as shown in the right side of the figure. The distances between two nearest Cr ions within the unit are 3.41 Å and 3.44 Å. There is bond alternation in half of the Cr-Cr chain connected via edge shared oxygens as circled in green in the figure. These has been explained the M-I transition arising from a Peierls mechanism and is driven by the tetramer
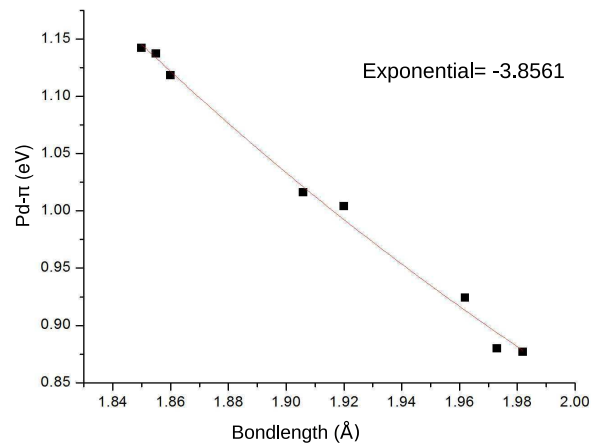
Figure 4.3 Interaction strength as a function of bondlength.
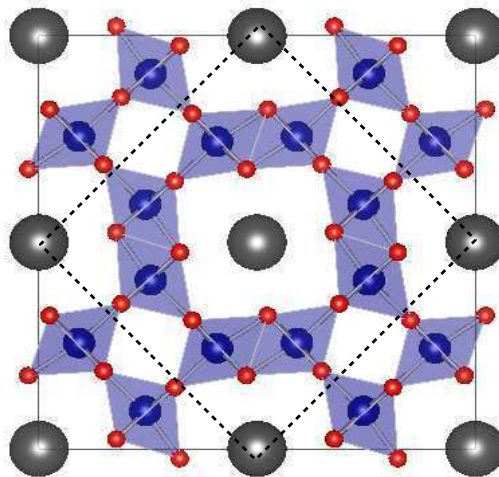
Figure 4.4 Unit cell for metallic and insulating phases of K_2Cr_8O16. The structure for metallic phase has been denoted within the dashed square.
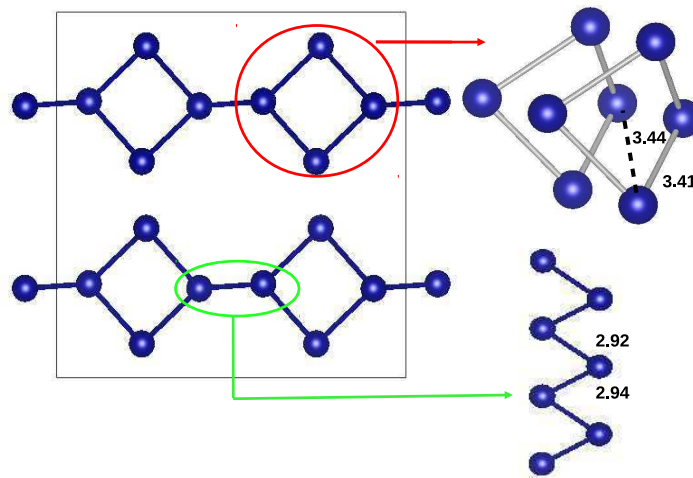
Figure 4.5 Tetramerization and dimerization in unit cell.

formation within the four Cr ions. Ferromagnetism in the system is described within a one dimensional double exchange model by Nishimoto *et.al* [3]. They have obtained a ferromagnetic ground state in the weak dimerization limit or the small gap limit.

So there could be two origins for the metal to insulator transition- Charge ordering in the system or the formation of tetramers in the four Cr units. For the charge ordering mechanism to work we need a $U > 3eV$ while for the peierls mechanism to open up the gap at lower value of U. So the value of U is very important to understand the mechanism responsible for the metal-insulator transition as we shall show with our detailed analysis.

To compare the two structures- charge-ordered and the experimental $P112_1/a$, we have calculated the partial DOS within VASP. The Cr-d and O-p are shown in Fig.4.6(a) and Fig.4.6(b) respectively. The red color is for the experimental structure while the black solid line represents that for the charge ordered structure. The partial DOS shows no significant difference between the two structures. Even the states near the fermi energy have almost the same weight for Cr-d and O-p for both the structures. We have simulated the X-ray diffraction patterns by the using software "Powder cell 2.3", for both the structures (Fig.4.7) and the pattern found shows very little intensity difference indicating how difficult
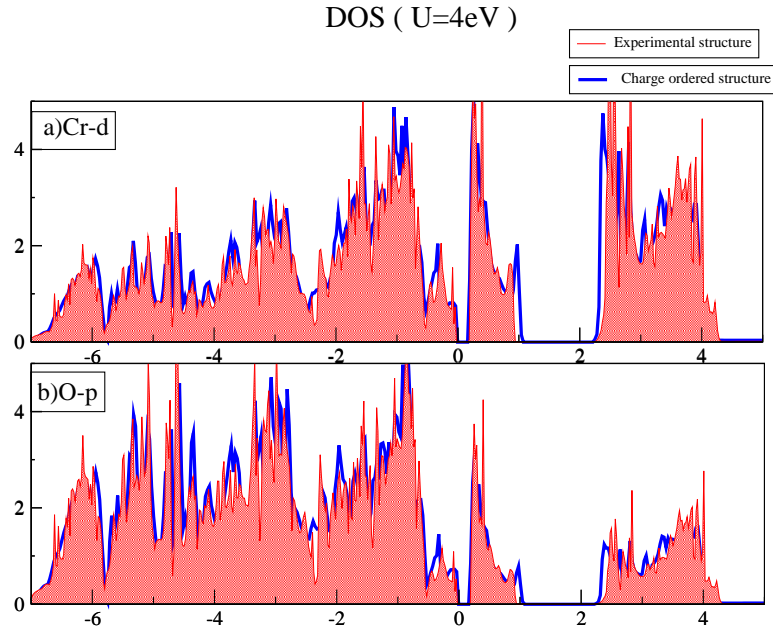
Figure 4.6 DOS-comparison between the Experimental and Charge-ordered Structure.

is is to distinguish between the two structures. Possibly a probe such as neutron diffraction can probe the magnetic moment differences and examine if one has charge ordering or not.

In further investigations we started with the experimental structure and tried to get charge-ordering in the $\sqrt{2} \times \sqrt{2} \times 1$ structure. For that we broke all the symmetries of the structure and find charge-ordering in the structure at U=4eV. The charge ordering pattern for the structure is slightly different from the previous report in this unit cell as shown in Fig.4.8. The charges are localized at the farthest sites within the tunnel formed by the 8 Cr to minimize the electrostatic repulsion between them as now there are more in-equivalent sites to localize the electrons. The charge ordered structure is again driven by the polaronic distortion as found in the previous charge-ordered structure. We find an elongation of one of the bondlengths for one of the Cr which results into enhancement of insulating gap. For U=4eV the energy of charge ordered solution for the $\sqrt{2} \times \sqrt{2} \times 1$ unit cell is 156 meV lower than the experimentally reported structure which has only tetramerization of four Cr ions connected through corner sharing oxygens. Further, we have calculated the total energies for the two structures, experimental P1121/a and the charge ordered structure for the larger unit cell $\sqrt{2} \times \sqrt{2} \times 1$. The total energies are
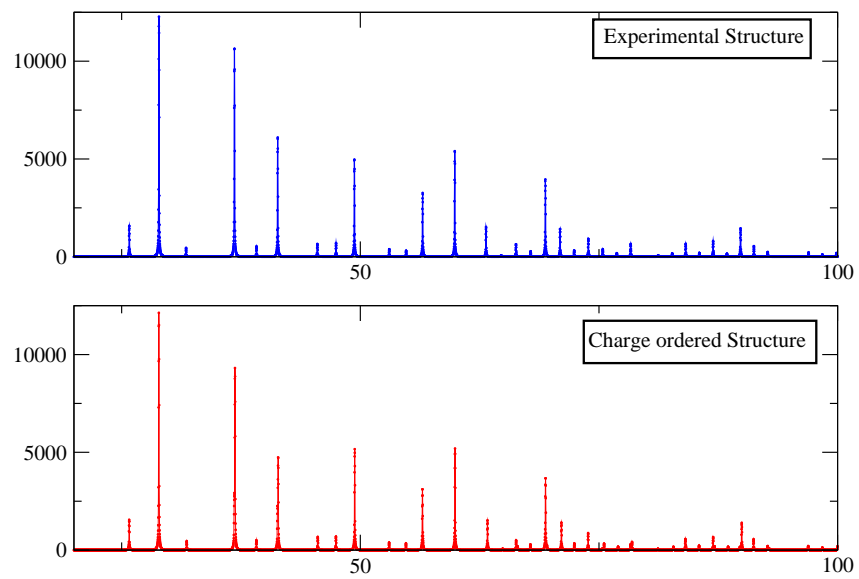
Figure 4.7 XRD for both Experimental and Charge-ordered Structure.
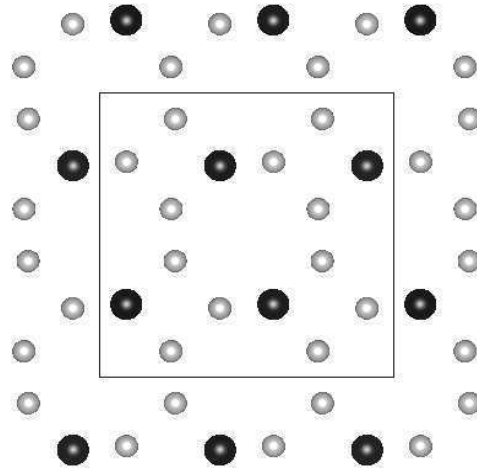
Figure 4.8 The network of Cr ions and the charge- ordering pattern in $\sqrt{2} \times \sqrt{2} \times 1$ unit cell. The blue circles represents the Cr^{3+} ions

shown in Table.4.3 and we can see the charge ordering is stabilized even in the larger unit cell for U > 3eV within our calculations.

We have also plotted the band gap variation as a function of U in Fig.4.9. We can see that the charge ordered solution has the larger gap than the experimental structure and the linear behavior of band-gap with U for the charge ordered structure suggests the gap has primarily d character. While in the case of the experimental structure the gap open ups at a higher value of U. It goes linear up to value U=3.5eV and then shows a constant behavior with U. This suggests the gap in this case has different origin.

To strengthen our results we have used a Hartree-Fock model and calculated the band gap for both the structures which are shown in Fig4.10. We again find the linear variation of band gap with U for the charge ordered structure. For the experimental structure, the band gap is linear upto U=2.25eV and then becomes constant upto U=2.75eV. This constant behavior of the band gap is similar to the GGA calculations but the value of U is smaller than the GGA calculations. The linear behavior of the band gap for higher values of U is similar to the charge ordered structure. We have calculated the occupancies of different Cr ions for these values of U. The occupancies are shown in Table.4.4. We have shown the occupancy of up spin channel only for different values of U. The Cr which has the

U(eV)	Total energies(in eV)	
	Experimental(eV)	Charge-ordered(eV)
2.00	-389.916	-389.817
2.25	-386.729	-386.654
2.50	-383.572	-383.523
2.75	-380.446	-380.423
3.00	-377.348	-377.356
3.25	-374.280	-374.320
3.50	-371.239	-371.315
3.75	-368.227	-368.341
4.00	-365.242	-365.398

Table 4.3 Total energies as a function of U(eV) for Experimental and Charge-ordered Structure.
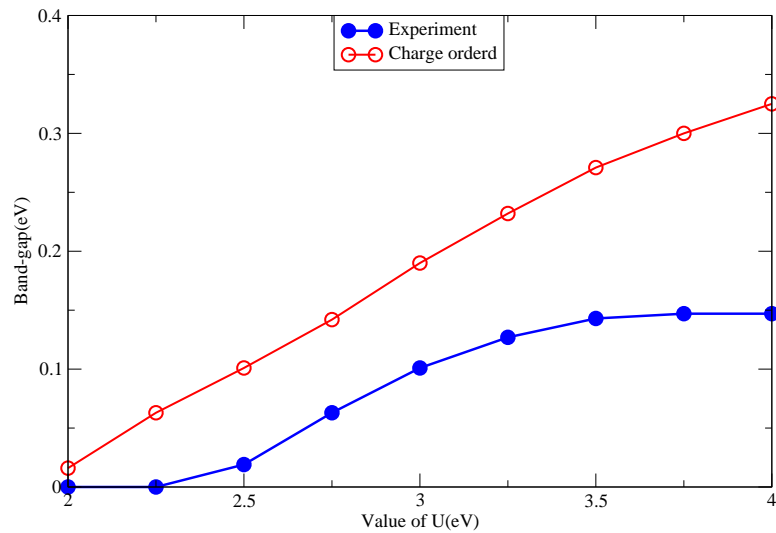
Figure 4.9 GGA band gap as a function of U for Experimental and Charge-ordered structure

highest occupancy has been labeled as Cr^{3+} and the Cr which has lowest occupancy labeled as Cr^{4+} in the table. We can see that the charge ordering is automatically setting in the experimental structure and the charge ordering getting more pronounced for higher values of U. The value of U at which charge ordering is established in the system is different for the two methods of calculations due to the different treatment of U in the two approaches. From a total energy comparison one finds that charge ordering is energetically favored at all values of U in the Hartree-Fock calculations. In Fig.4.11 we have shown the partial DOS for Cr^{3+} and Cr^{4+} at U=3eV for the experimental structure. The partial DOS clearly shows the charge ordering in the experimental structure.
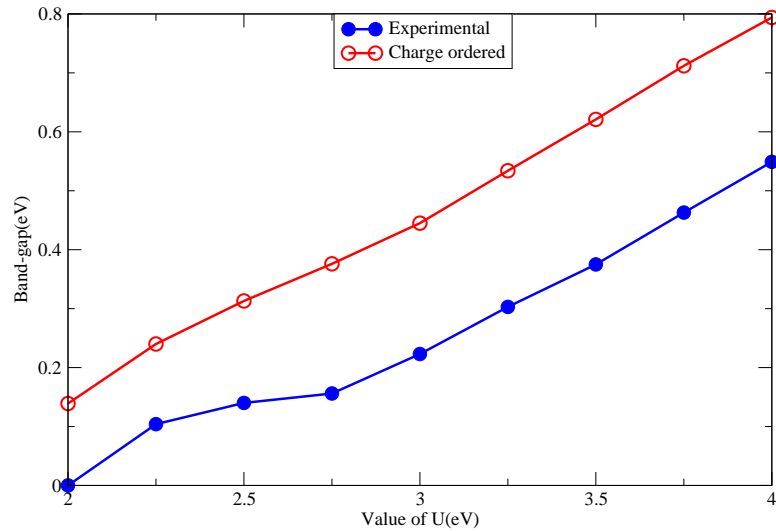
Figure 4.10 Hartree-Fock calculated Band gap variation as a function of U for Experimental and Charge ordered structure.
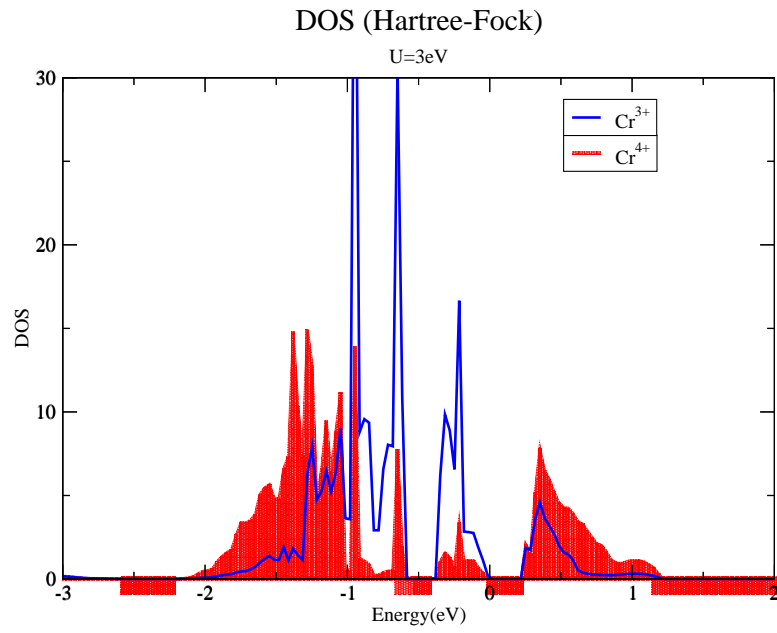
Figure 4.11 DOS calculated by Hartree-Fock calculation.

U(eV)	Occupancies	
	Maximum occupied Cr	Lowest occupied Cr
1.00	2.964	2.963
1.50	2.924	2.902
2.00	2.885	2.868
2.25	2.913	2.839
2.50	2.975	2.778
2.75	3.024	2.734
3.00	3.084	2.643
3.25	3.118	2.648
3.50	3.135	2.626

Table 4.4 Occupancies for maximum occupied and lowest occupied Cr ions as a function of U.

4.4   Comparison with $Rb_2Cr_8O_{16}$

$Rb_2Cr_8O_{16}$ is a holandite with a structure analogous to $K_2Cr_8O_{16}$. However it is reported to be a ferromagnetic semiconductor with magnetic transition at 295K and a insulator-metal transition at 300 K [13]. The higher ferromagnetic transition temperature compared to $K_2Cr_8O_{16}$ is surprising. $Rb_2Cr_8O_{16}$ has a slightly larger unit cell volume than $K_2Cr_8O_{16}$ which results in slightly longer Cr-O bond lengths. This increase in the transition temperature can not be explained by the increase in the Cr-O bond lengths. In this section we have studied the electronic structure of $Rb_2Cr_8O_{16}$ and tried to understand the microscopic interactions that are responsible for the higher T_c. We started with the experimental
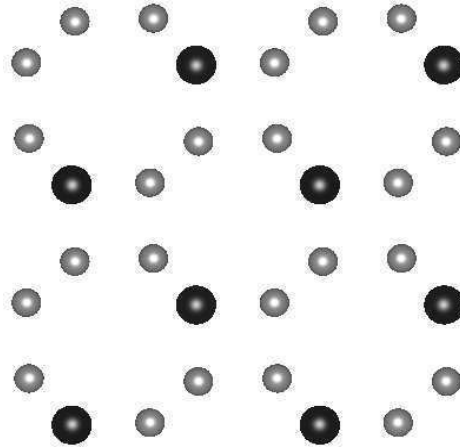
Figure 4.12 Charge ordering pattern found in $Rb_2Cr_8O_{16}$. Big black spheres represents the Cr^{3+} sites.

structure and examined for charge ordering. A similar pattern of charge ordering as found in $K_2Cr_8O_{16}$ is found here also and is shown in Fig.4.12. The charge ordered solution is 20 meV lower in energy than the non-charge ordered structure. The calculated partial density of states for the charge ordered structure is shown in Fig.4.13. The Rb states constitute in an energy interval far above the fermi level. Hence Rb behaves like a donor in the present system also. The Cr^{3+} and Cr^{4+} partial density of states are shown and one finds a higher weight in the Cr^{3+} t_{2g} states. One has significant admixture of the O

Compound	Ion	Moment(μ_B)	Charge	$n_d(up)$	$n_d(down)$
$Rb_2Cr_8O_{16}$	Cr^{3+}	2.385	3.443	2.796	0.427
	Cr^{4+}	2.142	3.407	2.650	0.522
$K_2Cr_8O_{16}$	Cr^{3+}	2.718	5.537	3.445	0.787
	Cr^{4+}	2.469	5.595	3.331	0.920

Table 4.5 Comparison of magnetic moments, total charge, occupancies for d(up) and occupancies for d(down).

p states in this energy window.
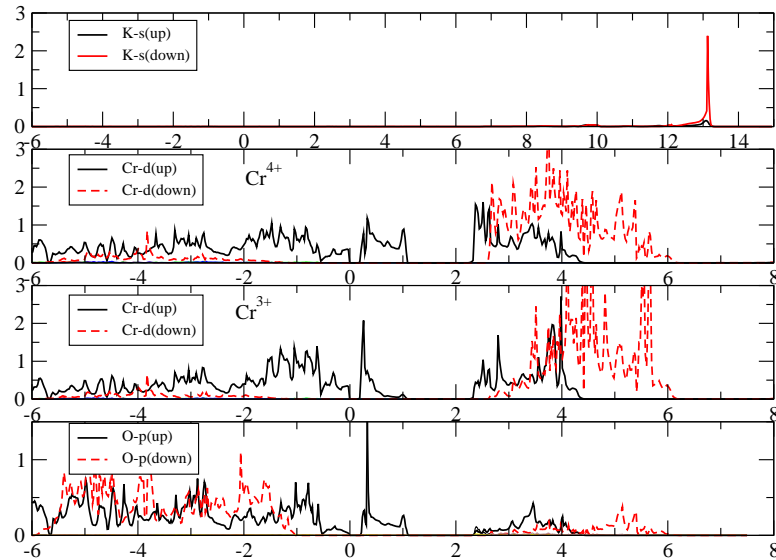
Figure 4.13 K-S, Cr^{3+}-d, Cr^{4+}-d and O-p partial DOS for Charge ordered $Rb_2Cr_8O_{16}$.

A comparison of the magnetic moments in the charge ordered structure is given in Table.4.5. One finds that the nominally Cr^{3+} atom has a magnetic moment of 2.385 in $Rb_2Cr_8O_{16}$ while that on Cr^{3+} in $K_2Cr_8O_{16}$ is 2.718μ_B. . The values for Cr^{4+} are also shown for the Cr^{4+} atom which is farthest from the Cr^{3+} atom.

In order to examine the stability of the ferromagnetic state, we calculate the energy for few repre-

Configuration	Energy(meV)
Ferromagnetic	0
AFM1	473
AFM2	272

Table 4.6 Energies in eV per formula unit for different magnetic configurations at U= 4eV

sentative antiferromagnetic configurations in the charge ordered state shown in Fig.4.14. The stability is more enhanced in the case of $K_2Cr_8O_{16}$ compared to the present system. This is contrary to what has been observed in the literature and possibly one must have a model which can describe the insulator-metal transition accurately.
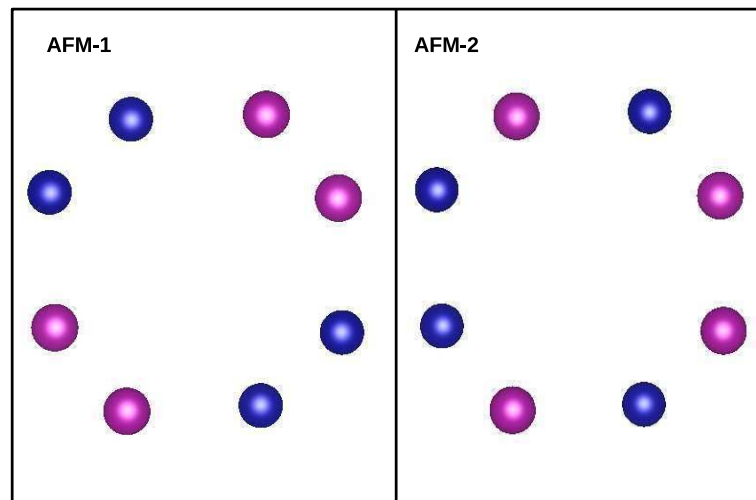
Figure 4.14 Anti-ferromagnetic configurations compared with ferromagnetic configuration.

We examine other aspects of the electronic structure of $Rb_2Cr_8O_{16}$ and compare the results with $K_2Cr_8O_{16}$. As the states contributing to the electronic structure are due to Cr d and O p, we map the ab-initio results calculated for U=0 to a tight binding model that includes Cr d - O p states in the basis. The comparison for $Rb_2Cr_8O_{16}$ is given in Fig.4.15 where the red dashed lines correspond to the ab-initio bands while the blue dashed lines represent the tight binding structure.

Atom(orbital)	Energies(eV)	
	$Rb_2Cr_8O_{16}$	$K_2Cr_8O_{16}$
Cr(d)	4.293	4.446
	4.110	4.219
	3.088	3.163
	2.915	3.005
	2.867	2.978
O1(p)	0.170	0.056
	-0.050	-0.108
	-0.094	-0.172
O2(p)	0.293	0.437
	-0.346	-0.178
	-0.647	-0.536

Table 4.7 On-site energies of various atoms for $Rb_2Cr_8O_{16}$ and $K_2Cr_8O_{16}$ from wannier calculations. O1 is edge-shared oxygen and O2 is corner-shared oxygen.

A comparison of the onsite energies are given in Table.4.7. One finds an almost rigid shift of the Cr d t_{2g} levels to lower energies in $Rb_2Cr_8O_{16}$ compared to $K_2Cr_8O_{16}$. A similar but opposite directional shift of the O p energies associated with the edge shared oxygens has been found in a reduction in the effective charge transfer energy in $Rb_2Cr_8O_{16}$ by 0.2 eV. However when one examines the corner shared oxygens, one finds an increase in the effective charge transfer energy by about 0.1-0.15 eV with the corner shared oxygens.

Further analysis is necessary to understand the microscopic origin of higher ferromagnetic transition temperature in $Rb_2Cr_8O_{16}$ compared to $K_2Cr_8O_{16}$.
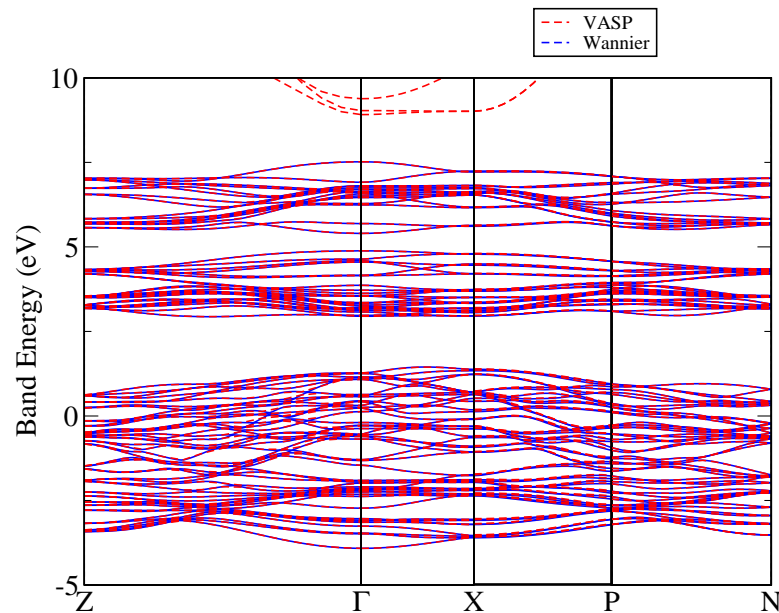
Figure 4.15 Comparison of band dispersions calculated from ab-initio and wannier calculations.

In this chapter we have have presented a microscopic model to capture various aspects of this charge ordering. A microscopic model has been constructed using Cr-d and O-p as its basis. We have also compared the analogous compound $Rb_2Cr_8O_{16}$ which has the same structure but the ferromagnetic transition temperature is 100 K higher than that of $K_2Cr_8O_{16}$

Bibliography

[1] Kunihiro Hasegawa et. al. PRL **103**, 146403(2009)

[2] P. Mahadevan, A. Kumar, D. Choudhury and D. D. Sarma, Phys. Rev. Lett. **104**, 256401 (2010).

[3] S. Nishimoto and Y. Ohta Phys. Rev. Lett **109**, 076401 (2012).

[4] S.Toriyama et. al. Rev. Lett **107**, 266402 (2011).

[5] G. Kresse, and J. Joubert,Phys. Rev. B **59**, 1758 (1999).

[6] G. Kresse, and J. Furthm$ü$ller, Phys. Rev. B. **54**, 11169 (1996); G. Kresse, and J. Furthm$ü$ller, Comput. Mat. Sci. **6**, 15 (1996).

[7] J. P. Perdew, Y. Wang Phys. Rev. B. **45**, 13244(1992)

[8] S.L. Dudarev et.al. Phy. Rev. B. **57**, 1505(1998)

[9] A. A. Mostofi, J. R. Yates, Y.-S. Lee, I. Souza, D. Vanderbilt and N. Marzari, wannier90: A Tool for Obtaining Maximally-Localised Wannier Functions, Comput. Phys. Commun., 178, 685 (2008)

[10] N. Marzari and D. Vanderbilt, Phys. Rev. B 56, 12847 (1997)

[11] Maximally localized Wannier functions for entangled energy bands, I. Souza, N. Marzari and D. Vanderbilt, Phys. Rev. B 65, 035109 (2001)

[12] P. Bhobe et. al (Unpublished).

[13] H. Okada, N. Kinomura, S. Kume and M. Koizumi Mat. Res, Bull. Vol. 13, pp. 1047-1053, 1978

Chapter 5

Cr doping in VO$_2$: Ferromagnetism in insulator.

5.1   Introduction

Metal to insulator transition in strongly correlated systems have been studied for decades due to the involvement of rich physics [1]. One such example that has been intensively studied is VO_2, which in the bulk form shows a metal to insulator transition at a temperature of 340K [2]. The high temperature phase is rutile phase(R) and the low temperature phase is monoclinic phase and has been denoted as M1 phase in the literature. In the monoclinic, M1 phase the V-V ions get dimerized along the c-axis all are tilted as well. Whether it is lattice distortion (Peierls mechanism) or the electron correlation (Mott-Hubbard) effects that drive the metal to insulator transition have been debated for decades with various evidence and arguments. The general view which is now accepted by theoreticians as well as experimentalists is that it is the cooperation between these two mechanisms which lead to a metal to insulator transition [3,4]. Both the mechanism contributes equally and so we can call it a Mott assisted Peierls transition or the vice versa. The non magnetic nature of the transition further complicates the understanding.

The temperature of metal-insulator transition can be reduced by strain or chemical doping *i.e.* we

can stabilize the rutile phase by applying strain or doping(W, Mo, Nb doping). The slight doping of Cr (up to 5 percent) leads to a transition to another monoclinic phase(M2) [5,6] in which only half of the V-V chains get dimerized and only half get tilted. This transition is identified as Mott-Hubbard type due to the antiferromagnetic nature of M2 phase. Pouget *et. al.* studied the relation between the dopants and structure. They applied uniaxial stress along the [110] direction to obtain the M2 phase [7]. At higher doping concentration $V_{1-x}Cr_xO_2$ shows room temperature ferromagnetism as well as insulating nature in the rutile phase [8]. Recent work by Piper *et.al.* [9] studied Cr doping in VO$_2$. They have used a combination of x-ray photo emission spectroscopy, resonant inelastic x-ray scattering, and resonant x-ray emission spectroscopy of the V $L_{3,2}$, O K, and Cr $L_{3,2}$ edges to study the electronic structure near the Fermi level of $V_{0.82}Cr_{0.18}O_2$. They find the formation of Cr^{3+}-V^{5+} pairs and they suggest that these may be responsible for the ferromagnetic insulating state. A theoretical investigation of electronic and magnetic properties of rutile $V_{1-x}Cr_xO_2$ was carried out by Williams *et. al.* [10] by using GGA and GGA+U calculations. They however found a ferromagnetic half-metallic ground state. They did not find the occurrence of Cr^{3+}-V^{5+} pairs in the system.

In this work we have studied the electronic structure of $V_{1-x}Cr_xO_2$ for x=0.125 and tried to understand the ground state properties of the system.

5.2   Methodology

The electronic structure for rutile VO_2 as well as $Cr_xV_{1-x}O_2$(x=0.125) is calculated using first principle electronic structure calculations within a plane-wave pseudo potential implementation of density functional theory within VASP [11] by constructing a $1 \times 1 \times 2$ supercell of VO$_2$. We have taken the high temperature experimental rutile structure and relaxed the structure to get the minimum energy solution. We have studied the electronic and magnetic properties for this relaxed structure. We have doped Cr by replacing one of the V atom by Cr. We have studied the effect of Cr doping without relaxation of the structure and with relaxation. The generalized gradient approximation (GGA) [12] was used for the exchange correlation functional and electron electron interactions were considered by including a

Hubbard U of 3.0 eV and 3.5 eV on V and Cr respectively within the GGA+U formalism [13]. A cutoff energy of 400 eV was used for the plane wave basis states. The calculations has been done for the ferromagnetic arrangement of spins on the metal sites. The density of states and magnetic moments were calculated within spheres of radii of 1.23, 1.37 and 0.8 for V, Cr and O respectively. The DOS has been calculated using the tetrahedron method. A gamma-centered k-points mesh of $4 \times 8 \times 8$ k-points is used for the k-space integrations and the solution for the electronic structure was carried out self-consistently till the energy difference between successive steps was better than 10^{-5} eV.

5.3 Results and discussion
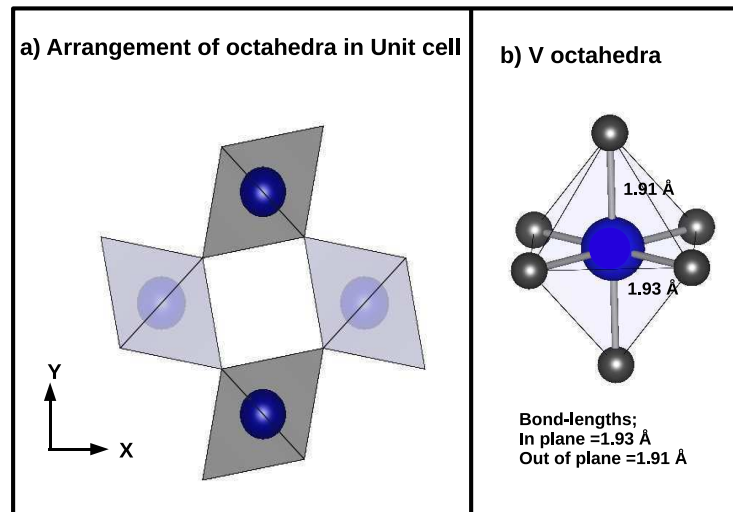
Figure 5.1 Structure of rutile VO_2. a)The unit cell has been shown in XY plane. b) VO_6 octahedra has been shown.

The rutile unit cell of VO_2 in the XY plane is shown in Fig.5.1. It consists of a network of four VO_6 octahedra as shown in Fig.5.1a. These octahedra units are rotated with respect to each other with two lighter shaded units lying in one plane and two other units consisting of darker shaded octahedra lying in the z=0.5 plane. These octahedra are rotated with respect to each other by 90° and are connected by corner shared oxygens. Each of the octahedra which are a part of this network consists of in plane
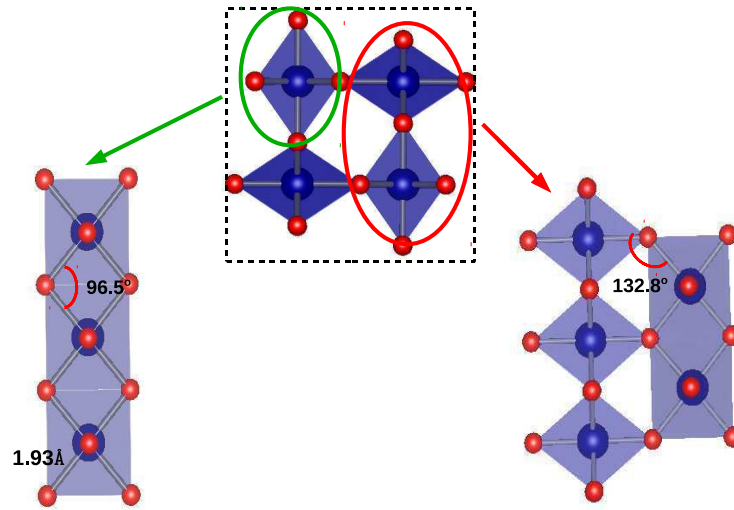
Figure 5.2 Connectivity of VO$_6$ octahedra within chain and between chains along z-direction has been shown.

bondlengths which are equal to 1.93Å while the out of plane bondlengths are reduced and equal to 1.91Å as shown in Fig5.1b. The connectivity of the octahedra in the z direction are shown in Fig.5.2. The network of the octahedra consists of edge shared octahedra in which the V-O-V bond angle is 96.5^o. The neighboring octahedra in the XY plane which are connected by corner shared oxygens have the V atoms making an angle of 132.8^o through the corner shared oxygens.

V in the VO$_2$ has a d^1 configuration. In an octahedral environment, the degeneracy of the fivefold degenerate d orbitals are lifted into into triply degenerate t$_{2g}$ levels and doubly degenerate e$_g$ levels. The single electron due to V goes to the t$_{2g}$ levels. Other degeneracies which are present such as the distortion of each VO$_6$ octahedron as well as the rotation with respect to neighboring octahedra are expected to result in a metallic ground state. This is clearly seen in the density of states shown in Fig.5.3 where both the V-d as well as O p partial density of states are shown. A half metallic ground state is found in the calculations with significant V-d character.

We then replaced one of the V atoms in the 8 V atom supercell of the VO$_2$ that we considered which translates into a doping percentage of 12.5%. The calculated density of states in the absence of any structural relaxation are shown in Fig.5.4. The Cr d partial density of states are shown in Fig.5.4
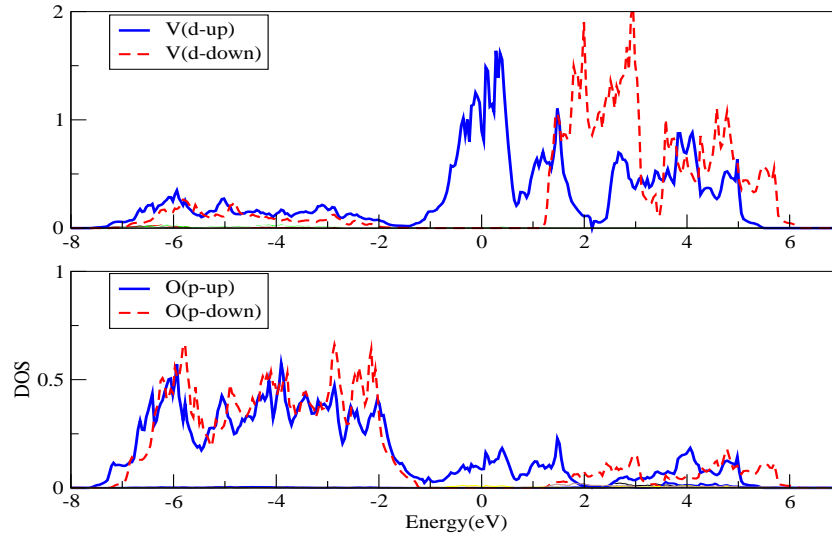
Figure 5.3 V-d and O-p partial DOS for VO$_2$ has been shown. Blue solid lines represents DOS for up spin and dashed red line for down spin.

where the up spin t$_{2g}$ states seen to be completely occupied with a very small weight above the Fermi level. The V atom just below the Cr in the z direction has very small weight of states below the fermi level. This atom seems to be behaving like a V^{5+} species. The V atoms which we denote as V^{4+} are also found to have a strongly depleted density of states at the fermi level. So the mere addition of the Cr seems to be bringing the system to the brink of metal-insulator transition. Cr seems to favor the 3+ configuration over the isovalent 4+ one. To achieve this it grabs electrons from the neighboring V atoms, with an electron being grabbed from the V atom with which it shares an edge shared octahedron more than the others. As a result the V which is a part of the edge shared octahedra network with Cr becomes V^{5+}, while Cr becomes Cr^{3+}. It is also surprising how the system is brought to the brink of a metal-insulator transition by the doping.

Allowing for structural relaxation, one finds the distortions as shown in Fig.5.5. The Cr-O bondlengths increase from the value 1.93Å found in undoped VO$_2$ to 1.98Å. Similarly there is a corresponding decrease in the V-O bondlengths of the V in the edge shared octahedron with Cr. These bondlengths become 1.85Å and we call these V^{5+}. In addition one finds a slight dimerization of the V^{4+} atoms as
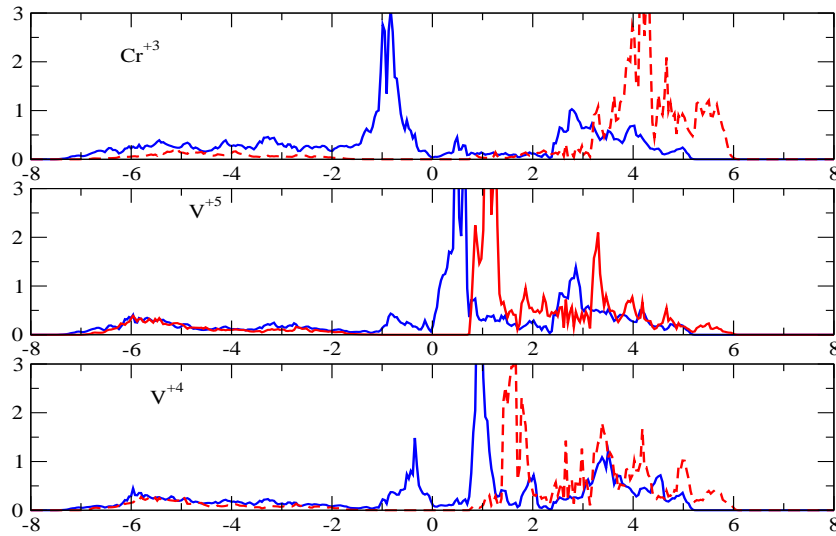
Figure 5.4 Cr-d, V-d and O-p partial DOS for Cr doped VO$_2$(not relaxed) has been shown. Blue solid lines represents DOS for up spin and dashed red line for down spin.

shown in the Fig.5.5. The network of the transition metal atoms in then XY plane are also shown.

The Cr-d as well as V-d partial density of states are shown in Fig.5.6. The few up spin states with t$_{2g}$ symmetry that were unoccupied in the case of Cr^{3+} vanish. Further V^{5+} becomes more so with a corresponding increase in the weight of V^{4+}. This is reflected in the magnetic moments of Cr^{3+} and V^{5+} which is 2.577 μ_B and 0.167 μ_B.

The main change due to relaxation is in the chain consisting of Cr^{3+} and V^{5+} ions. The effect of this distortion could be understood by Fig.5.7. The increased distance between oxygen and Cr reduce the hopping interaction between them which results in lowering of the antibonding levels as shown schematically in Fig.5.7a. The effect is opposite in the case of V where the bondlengths with oxygen have decreased which results in an upward shift of the antibonding levels. This further lowering of Cr levels favors the transfer of electrons from V to Cr. This further localization of electron on Cr opens up the gap results into insulating state. The other changes in the relaxed structure is the dimerization of V-V in the chain connected to the V-Cr chain. The distances between two V atoms in the chain which dimerized is shown in the Fig.5.5.
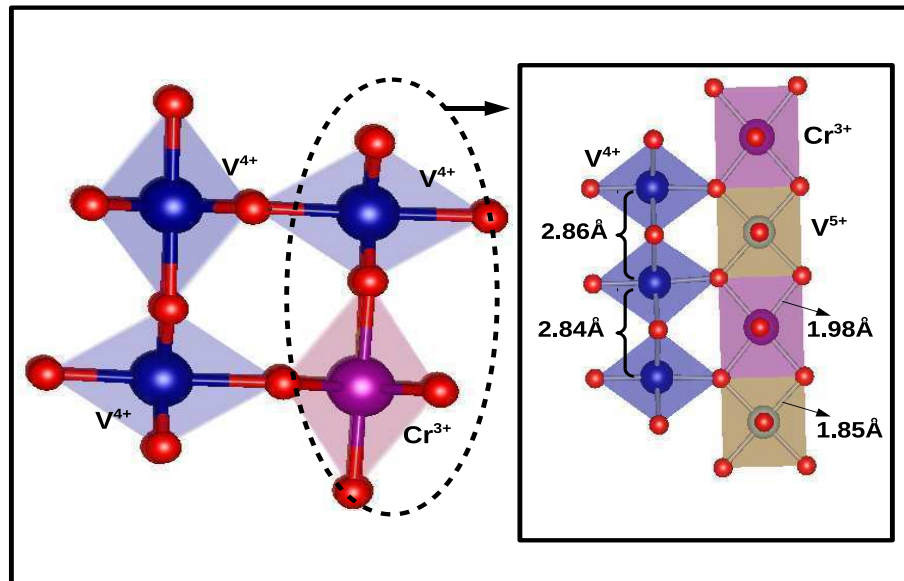
Figure 5.5 Relaxed structure for Cr doped VO_2 has been shown. Changed bondlengths have also been written.

The final question we asked was where does the additional stability for the charge ordering come from and why does the V atom from which Cr grabs an electron belong to the edge shared octahedra network. The answer to both the aspects are related. The metal-oxygen bonding is weaker in the case of the edge shared octahedra. Hence it is easier to localize the charge on Cr there. Additionally one gains from the attractive electrostatic interactions between the V^{5+}-Cr^{3+} ions. Part of the energy gain also comes from Hund's exchange energy associated with the d^3 configuration that is favored on the Cr site.

We have examined the ferromagnetic insulating state in Cr doped VO_2. The formation of Cr^{3+}-V^{5+} units are found which stabilize the ferromagnetic insulating state which is also charge ordered.
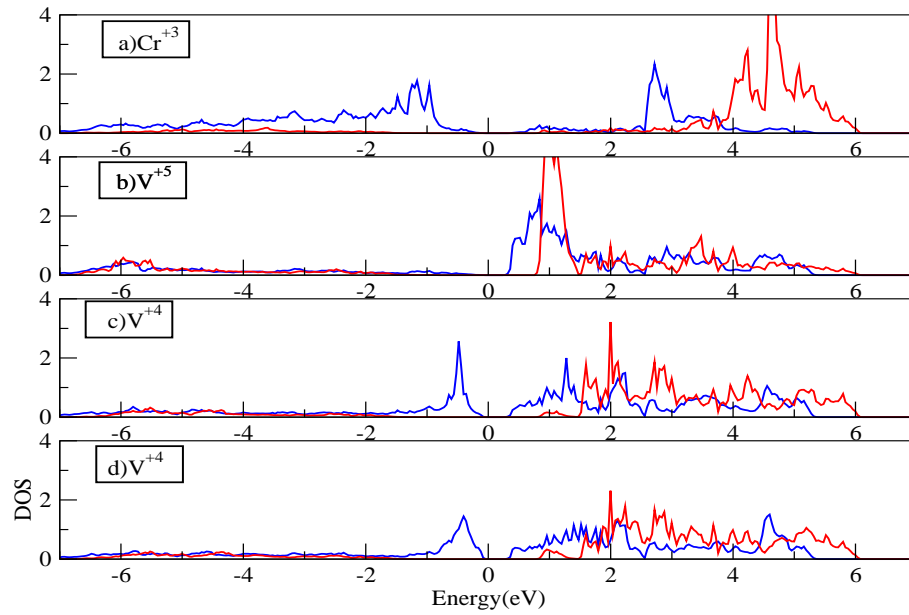
Figure 5.6 Cr-d, V-d and O-p partial DOS for Cr doped VO$_2$(relaxed) has been shown. Blue solid lines represents DOS for up spin and dashed red line for down spin.
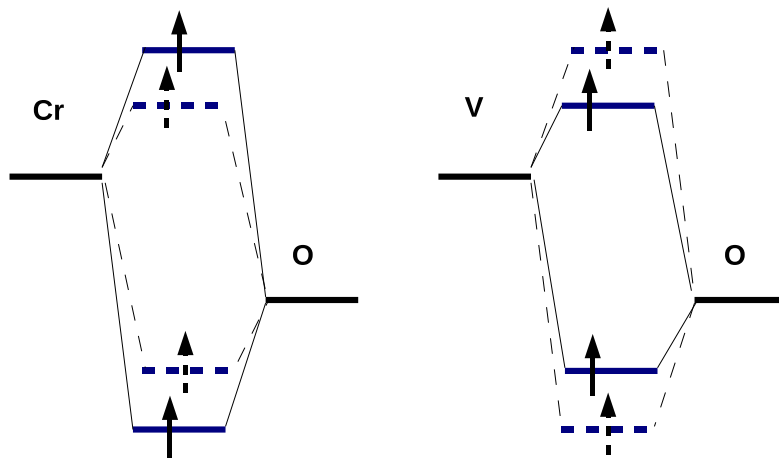
Figure 5.7 Effect of bondlength changes on bonding and anti bonding levels has been shown schematic for Cr and V. Blue solid lines and blue dashed lines represent the unrelaxed and relaxed cases respectively.

Bibliography

[1] M. Imada, A. Fujimori, and Y. Tokura, Rev. Mod. Phys. 70, 1039 (1998).

[2] F. J. Morin, Phys. Rev. Lett. 3, 34 (1959).

[3] M. W. Haverkort, Z. Hu, A. Tanaka, W. Reichelt, S. V. Streltsov, M. A. Korotin, V. I. Anisimov, H. H. Hsieh, H.-J. Lin, C. T. Chen, D. I. Khomskii, and L. H. Tjeng, Phys. Rev. Lett. 95, 196404 (2005).

[4] T. C. Koethe, Z. Hu, M. W. Haverkort, C. SchÃijÃ§ler-Langeheine, F. Venturini, N. B. Brookes, O. Tjernberg, W. Reichelt, H. H. Hsieh, H.-J. Lin, C. T. Chen, and L. H. Tjeng, Phys. Rev. Lett. 97, 116402 (2006)

[5] J. B. Goodenough and H. Y. P. Hong, Phys. Rev. B 8, 1323(1973).

[6] M. Marezio, B. Mcwhan, P. D. Dernier, and J. P. Remeika, Phys.Rev. B 5, 2541 (1972).

[7] J. P. Pouget *et. al.* Phys. Rev. Lett. 35, 873 (1975).

[8] West *et. al* J. Supercond.Novel Magn. 21, 87 (2008).

[9] L. F. J. Piper *et. al.* PHYSICAL REVIEW B 82, 235103 (2010)

[10] M. E. Williams, W. H. Butler, C. K. Mewes, H. Sims, M. Chshiev and S. K. Sarker, J. Appl. Phys. 105, 07E510 (2009).

[11] G. Kresse, and J. Furthm*ü*ller, Phys. Rev. B. **54**, 11169 (1996); G. Kresse, and J. Furthm*ü*ller, Comput. Mat. Sci. **6**, 15 (1996).

[12] J. P. Perdew, Y. Wang Phys. Rev. B. **45**, 13244(1992)

[13] S.L. Dudarev et.al. Phy. Rev. B. **57**, 1505(1998)

Chapter 6

Ferromagnetic insulator Bi_2NiMnO_6:

6.1 Introduction

Multifunctional materials have come into the forefront of modern day research owing to technological considerations. As the name suggests these are materials with more than one functional property and one such subcategory of materials that have received attention in this direction are multiferroics. These are compounds in which ferroelectricity and ferromagnetism coexist. The important members of this class of compounds are those in which there is a strong cross coupling between the magnetic and ferro-electric degrees of freedom *i.e.* the direction of magnetization can be switched by an external electric field and the direction of polarization can be switched by external magnetic field. It will reduce the thermal power of a magnetic memory. It will also provide extra degree of freedom in memory devices. Despite their usefulness there are very few ferromagnetic ferroelectrics. This is because non-zero d occupancy is needed for magnetism. However there seems to be tendency for off-centric displacements of the transition metal atoms to be disfavored in systems with finite d-occupancy. Even among the multiferroics that exist, most are antiferromagnetic [1]. Recently a new route to ferromagnetic ferro-electrics was chosen by Azuma *et al.* [2] They adopted an established design principle provided by Goodenough [3–5] to obtain a ferromagnetic insulator. The idea was to consider an ordered double perovskite oxide of the form $ABB'O_6$ with ordering at the B-site. Now the transition metal atoms form

an ordered rock salt structure. By the Goodenough rule if one transition metal atom had completely filled e_g levels in one spin channel (half filled e_g levels) and the neighboring transition metal atom had empty e_g levels then a ferromagnetic insulator would be realized. Now introducing an atom which has lone pair of electrons such as Pb or Bi [6, 7] at the A-site stabilizes a non centro symmetric structure which is pre-requirement for ferroelectricity. One such material which is stabilized by a high pressure synthesis was Bi_2NiMnO_6(BNMO) [2]. The system was found to be ferromagnetic upto a temperature of 140 K and although no ferroelectric polarization loops were measured, a dielectric anomaly was observed at 485K. Thin film of Bi_2NiMnO_6 [8, 9] grown on $SrTiO_3$ however shows clear evidence of ferroelectricity with hysteresis shows saturation polarization of about 5μC/cm^2.

6.2 Methodology

In this work we have studied the electronic structure of both the ferroelectric as well as the paraelectric phases of Bi_2NiMnO_6. The route to ferromagnetism as proposed by Goodenough and Kanamori which was used in this material to obtain a ferromagnetic state has been critically examined. In order to examine if ferromagnetism emerged, one chose *Ni* which had a formal valency of 2+ and consequently a d^8 configuration at the *Ni* site, and *Mn* which had a formal valency of 4+ and a d^3 configuration. These valencies at the *Mn* and *Ni* sites were confirmed by an analysis of the calculated density of states within the ab-initio calculations [10, 11].

   In order to calculate the electronic structure of Bi_2NiMnO_6, we have used first principle density functional theory as implemented in VASP simulation package [13]. We have used the projected augmented wave method [12]. We have used $4 \times 4 \times 4$ Monkhorst pack mesh and a plane wave cutoff of 400 eV for calculations.The generalized gradient approximation (GGA) [14] was used for the exchange and electron correlations were considered by including a Hubbard *U* within the GGA+U formalism [15]. The total energy was calculated self-consistently till the energy difference between successive steps was better than 10^{-5} eV. The total energy of the ferromagnetic configuration was compared with the energy of two competing configurations shown in Fig.6.1. In order to understand the results further we

constructed a multiband Hubbard model. The real structure was not taken but just the *Ni* and *Mn* atoms. The *Ni*-d and *Mn*-d levels were taken in the basis. Hopping was allowed between *Ni*-d and *Mn*-d states as well as between *Ni-Ni* and *Mn-Mn* states. The values of the hopping interaction strengths entering the model were chosen by a Wannier mapping of the ab-initio band structure onto a tight binding model with *Ni*-d and *Mn*-d states in the basis. Full multiplet Coulomb interactions were included on both *Ni* and *Mn* and these were parametrized in terms of the Slater-Condon parameters F^0, F^2 and F^4. The values of F^2 and F^4 which are related to the exchange splitting were varied to change the ordering of t_{2g}-e_g levels on *Mn* and explore the role of different level orderings on the ferromagnetic stability. A mean field decoupling scheme was used in order to decouple the four fermion terms, and the resulting Hamiltonian was solved self-consistently till the difference in energy between successive iterations was better than 10^{-5} eV. A k-points mesh of $10 \times 10 \times 10$ k-points was used for the calculations. We also examined if the ferroelectric structure was the ground state structure. This was done by calculating the energy of both structures as a function of volume as the two structures had different volumes.

There are some work done on Bi_2NiMnO_6 by such approach but they have not compared the non-ferroelectric and ferroelectric structures([10, 11]). Even the experiments on dielectric measurements shows only the variation of dielectric constant with variation of temperature they have not shown the P-E hysteresis curve for the sample. To check how stable the ferroelectric state is we have done similar calculations for non-ferroelectric structure([16]). Volume for both the structures are different so we have done the volume optimization and compared the stability of both the structure.

6.3 Results and discussion

The energies of different magnetic configurations considered for both the ferroelectric as well as the non-ferroelectric structure are given in Table.6.1. These are given for one formula unit. One finds that the energy of both the ferromagnetic as well as the type-2 antiferromagnetic configuration are quite close in energy for the ferroelectric structure. A similar conclusion is found for the non ferroelectric structure also. This implies that the Goodenough-Kanamori rule which was used as a design principle
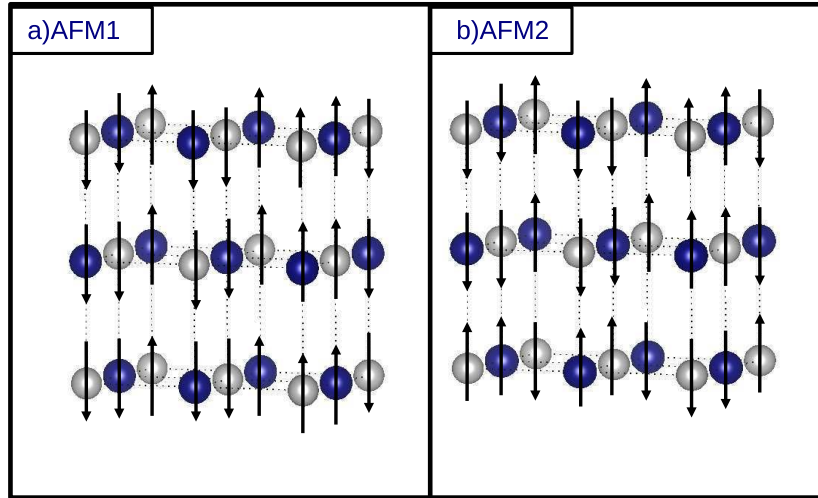
Figure 6.1 Two magnetic configurations which are compared with ferromagnetic configuration. The blue and white colored spheres are representing Ni and Mn respectively.

	Energies (in eV)	
	Ferroelectric	Non-ferroelectric
Ferro	-64.602	-64.718
Type-1	-64.547	-64.700
Type-2	-64.604	-64.714

Table 6.1 Energies of different magnetic configurations for ferroelectric structure and non ferroelectric structure at U=0eV

is failing in the present case. The origin of this could be that the second neighbor interactions between $Mn - Mn$ and $Ni - Ni$ could be sizable and therefore swamping the effect of nearest neighbor $Ni - Mn$ interactions. The second neighbor interactions are antiferromagnetic for both Ni and Mn as a result of half-filled e_g+ half-filled t_{2g} being involved. The experimental evidence in this system is conclusive and they have found ferromagnetic. They have shown temperature dependence of magnetic susceptibility which shows ferromagnetic transition at T=140 K.

	energies (in eV)	
	Ferroelectric	Non-Ferroelectric
Ferro	-60.650	-61.073
Type-1	-60.517	-60.978
Type-2	-60.570	-61.033

Table 6.2 Energies of different magnetic configurations for ferroelectric structure and Non-ferroelectric structure with U=4 eV

Hence we wondered if the failure to describe the ferromagnetic ground state was a consequence of the treatment of electron-electron interactions and so we examined the magnetic stability within GGA+U calculations using a U of 4 eV on both *Ni* and *Mn*. A comparison of the magnetic stabilization energies are given in Table.6.2 for both the ferroelectric as well as the non-ferroelectric structure. The ferromagnetic configuration is found to be strongly stabilized by 80 meV over the closely competing antiferromagnetic configuration which we have labeled as Type-2. A similar result is also obtained for the non-ferroelectric case though the ferromagnetic stabilization energy is reduced.

In order to understand this result, we examined the density of states. The density of states for U$=0$ is plotted in Fig.6.2. In both cases of *Mn* and *Ni*, the expected configuration of d^3 and d^8 are realized, resulting in the expected valencies of $+4$ and $+2$ respectively. The level ordering one gets is shown schematically in Fig.6.4a. On *Ni* one has the ordering $t_{2g}^{\uparrow}$, $t_{2g}^{\downarrow}$, $e_g^{\uparrow}$ all of which are occupied while $e_g^{\downarrow}$ is unoccupied. The $t_{2g}^{\downarrow}$ and $e_g^{\uparrow}$ levels are almost energetically degenerate. Examining the *Mn*-d partial density of states, one finds that $t_{2g}^{\uparrow}$ occupied as expected. However examining the unoccupied states one finds that the $t_{2g}^{\downarrow}$ spin states are below the $e_g^{\uparrow}$ spin states. This then complicates the design principles the $e_g^{\uparrow}$ states to which electrons on *Ni* can hop to are much higher in energy. Hence $Ni-Mn$ hopping is largely destabilized and hence ferromagnetism is not found at the U$=0$ limit. We then went on to examine the *Mn*-d and *Ni*-d partial density of states found in the U$=4$ calculation shown in Fig.6.3. Now one finds that the ordering is changed and Mn $e_g^{\uparrow}$ spin states are the lowest energy unoccupied states. This is the factor that brings back ferromagnetism being favored in this system. These results

are shown schematically in Fig.6.4.
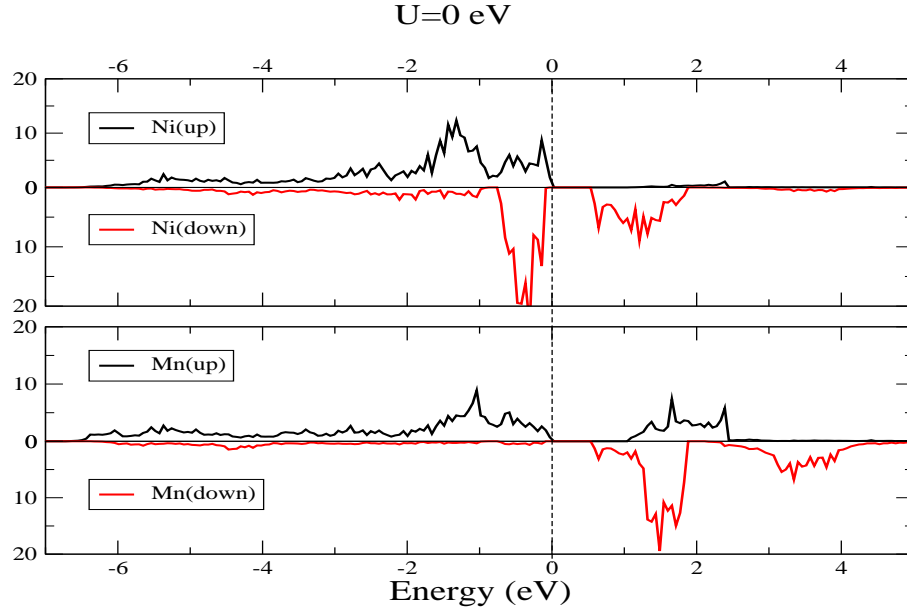
Figure 6.2 Ni-d and Mn-d Partial DOS has been shown at U=0eV.

An examination of the density of states and the total energies enabled us to construct a basic picture for the mechanism. However, to put the picture on firmer ground we decided to examine the results within a multiband Hubbard model which gave us more control on the parameters. Several calculations were performed and we present the result for two sets labeled case-1 and case-2. The calculated partial DOS has been shown in Fig.6.5. The difference in the two cases presented here are in the level ordering. Case-1 has Ni $e_g^\uparrow$ as highest occupied levels and Mn $e_g^\uparrow$ as the lowest unoccupied levels while case-2 has Ni $e_g^\uparrow$ as highest occupied levels and Mn $t_{2g}^\uparrow$ as the lowest unoccupied levels. The energies of the ferromagnetic configuration are compared with the competing antiferromagnetic configuration found within the ab-initio calculations. Case-1 has the ferromagnetic state strongly stabilized while case-2 has the ferromagnetic and antiferromagnetic configurations have similar energies.

In next part of our work we have compared the ferroelectric structure and nonferroelectric structure to check how stable is the ferroelectric structure. This has been calculated as a function of volume for
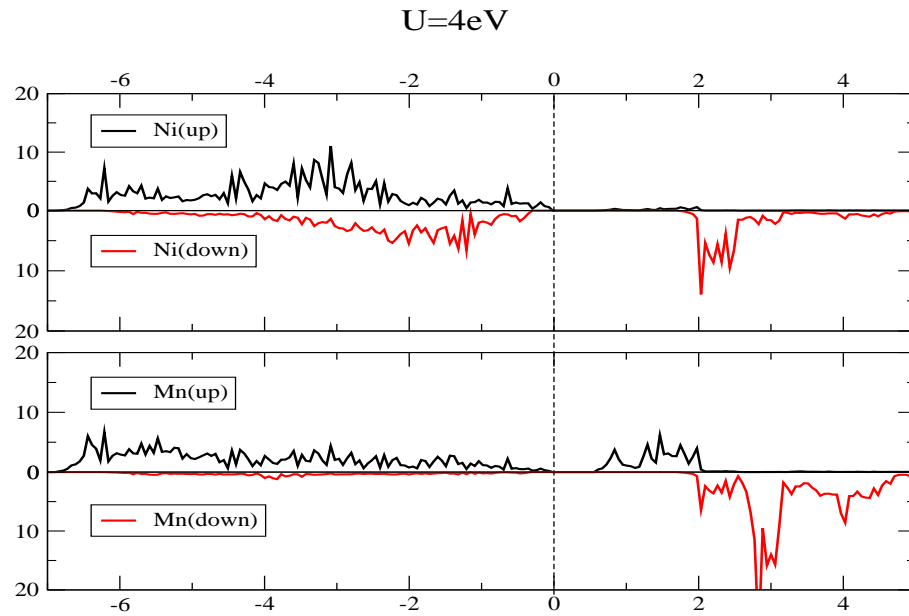
Figure 6.3 Ni-d and Mn-d Partial DOS has been shown at U=4eV.

both structures at U=4eV and ferromagnetic configuration. The continuous curve is for the Murnaghan equation of state which has been fitted to the data. The variation of energies with volume of unit cell has been shown in Fig.6.6 for both ferroelectric structure and nonferroelectric structure. The blue line is for nonferroelectric structure and red for ferroelectric structure. We found that the nonferroelectric structure is more stable for bulk Bi_2NiMnO_6. Thin films may be a route of stabilizing ferroelectricity in this system.

So we find that the electron correlations is necessary to describe the ferromagnetic ground state in Bi_2NiMnO_6 and within our calculations the compound is nonferroelectric contrary to the experiments.
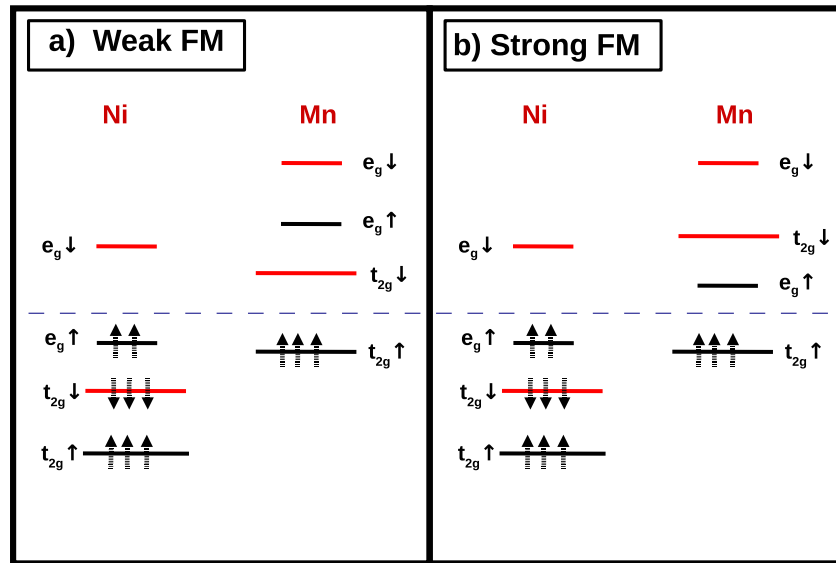
Figure 6.4 Schematic diagram to show level ordering in case of a) U=0eV b) U= 4eV.
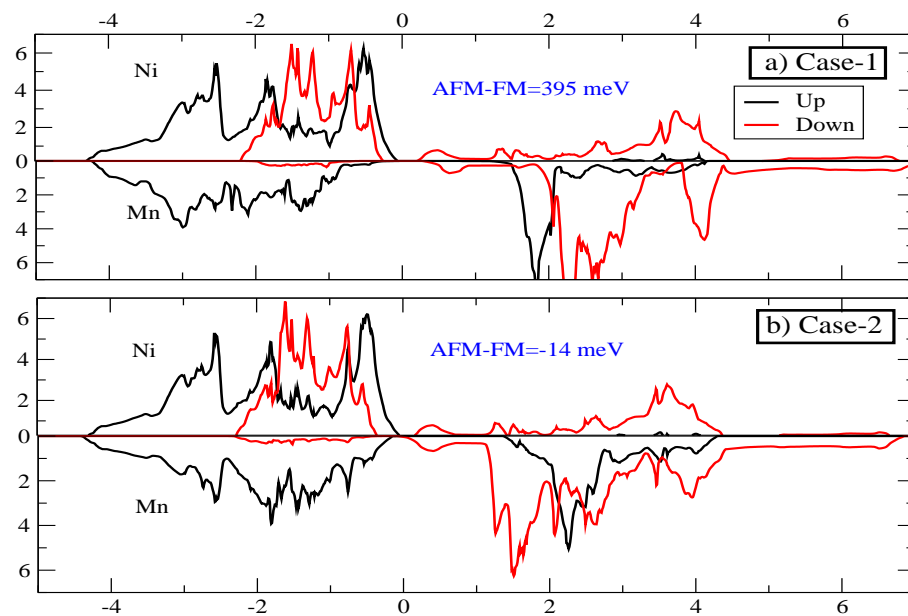
Figure 6.5 Ni-d and Mn-d Partial DOS calculated using multiband Hubbard model for case-1 and case-2. The energy difference between ferromagnetic and antiferromagnetic configuration has been written.
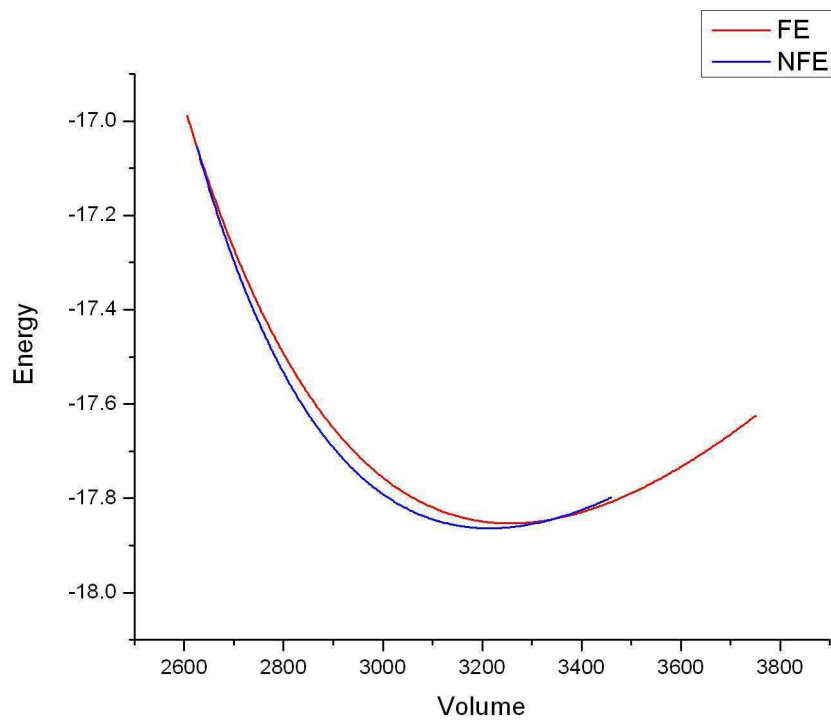
Figure 6.6 Volume optimization curve for ferroelectric and non-ferroelectric structures.

Bibliography

[1] Chiba et al. J. sol. St. chem. 145, 639

[2] Masaki Azuma, Kazuhide Takata, Takashi Saito, Shintaro Ishiwata, Yuichi Shimakawa and Mikio Takano J. AM. CHEM. SOC. 2005, 127, 8889-8892

[3] J. B. Goodenough, Phys. Rev. **100**, 564 (1955).

[4] J. B. Goodenough, J. Phys. Chem. Solids **6**, 287 (1958).

[5] J. Kanamori, J. Phys. Chem. Solids **10**, 87 (1959).

[6] Seshadri, R.; Hill, N. A. Chem. Mater. 2001, 13, 2892-2899.

[7] Kuroiwa, Y.; Aoyagi, S.; Sawada, A.; Harada, J.; Nishibori, E.; Takata, M.; Sakata, M. Phys. ReV. Lett. 2001, 87, 217601

[8] Maiko Sakai, Atsunobu Masuno *et. al.* APL 90 072903

[9] P Padhan1, P LeClair1, A Gupta1,3 and G Srinivasan J. Phys.: Condens. Matter 20 355003

[10] Hong Jian Zhao, Xiao Qiang Liu, and Xiang Ming Chena. AIP ADVANCES 2, 022115 (2012)

[11] Adrian Ciucivara,Bhagawan Sahu and Leonard Kleinman1 PHYSICAL REVIEW B 76, 064412 (2007)

[12] G. Kresse, and J. Joubert,Phys. Rev. B **59**, 1758 (1999).

[13] G. Kresse, and J. Furthm*ü*ller, Phys. Rev. B. **54**, 11169 (1996); G. Kresse, and J. Furthm*ü*ller, Comput. Mat. Sci. **6**, 15 (1996).

[14] J. P. Perdew, Y. Wang Phys. Rev. B. **45**, 13244(1992)

[15] S.L. Dudarev et.al. Phy. Rev. B. **57**, 1505(1998)

[16] Talata, K. Azuma, M. *et. al.* Journal of the Jap. Soc. of powder metallurgy, 52(12), 913(2005)

Chapter 7

A model for ferroelectricity in BaTiO$_3$

7.1   Introduction

Inspite of the first observation of ferroelectricity in BaTiO$_3$ in 1949, an understanding of the microscopic interactions that stabilize the ferroelectric state are still evolving. The seminal work by Cochran [1] pointed out using a shell model for lattice dynamics that short-range and long range coulomb forces compete and result in a cancellation of forces in BaTiO$_3$, resulting in some phonon modes going soft. This empirical model proposed within the framework of a shell model could explain the experimental observations of ferroelectric phase. The accepted view that has emerged since then has been that ferroelectricity emerges from a delicate balance between short-range repulsions that favor the cubic paraelectric phase and long-range electrostatic forces that favor the ferroelectric state [2, 3]. This picture of ferroelectricity was based on an ionic picture of the solid. The work by Cohen and Krakauer [4] showed within ab-initio calculations that if the Ti d states were moved high up in energy, ferroelectricity in tetragonal BaTiO$_3$ vanished, suggesting that the hopping interaction between Ti d and O p states played an important role in ferroelectricity. They considered the rhombohedral and tetragonal displacements of the Ti atoms and found the total energy variations with displacement led to a minimum away from the high symmetry centro-symmetric positions. The depth of this minimum was larger for the rhombohedral displacement than for the tetragonal displacement. Examining the various

contributions to the energy minimum, they found that the calculated electrostatic energy decrease was smaller for the tetragonal displacement than the rhombohedral displacement, suggesting that a significant part of the energy lowering came from a modification in the electrostatic energy. Later important work by Cohen [5] showed using all electron, full potential, linearized augmented plane wave method within LDA, that the Ti d-O p interactions were substantial in BaTiO$_3$ and played a major role in stabilizing ferroelectricity.

The first quantitative estimate of the role of various microscopic interactions was carried out by Ghosez *et al.* who carried out a separation of the interatomic forces within first principle calculations and extracted out the part emerging from dipole-dipole interactions [6]. This at a microscopic level depends on the Born effective charge as well as the dielectric tensor. As a result of the analysis they could quantify the balance of forces generating the unstable cubic phonon mode and they went on to investigate the role of the Born effective charges in driving the phonon softening. The analysis was extremely useful in distinguishing the role played by various microscopic interactions in the rhombohedral phase of BaTiO$_3$ subjected to isotropic pressure. This analysis again does not clearly separate out the role played by covalent interactions which enter in such a model through the renormalized Born effective charge.

In order to understand the microscopic interactions that determine if ferroelectricity is favored, we look at various contributions to the energy. Considering the ionic limit, Ba takes on the configuration Ba^{2+}, O becomes O^{2-} while Ti becomes Ti^{4+}. Treating the ions as a point charges we calculate the Ewald energy contribution to the total energy. The earlier discussion in the paper has pointed out the important role played by covalent interactions in stabilizing ferroelectricity and so the part of the energy emerging from covalent contributions is examined and is referred to as the band energy in the ensuing discussion. In addition the electrons have a charge distribution associated with them and so the mean field contribution associated with an electron interacting with other electrons is computed as the Hartree energy and we examine this contribution also. We now examine the various contributions to the total energy within this model considering the paraelectric structure of BaTiO$_3$ as well as the tetragonal structure which exhibits ferroelectric distortions. One finds a gain in the band energy of 340 meV for

the ferroelectric structure over the paraelectric structure. The Ewald energy is found to increase by 1116 meV as one goes from the paraelectric structure to the ferroelectric one. So, in contrast to the belief that long ranged Coulomb interactions stabilize the ferroelectric structure, one finds that this contribution to the total energy actually stabilizes the paraelectric structure. Indeed, the total energy for the ferroelectric structure is lower by 11 meV, and adding the band energy contributions as well as the Ewald energy contribution, one finds that the paraelectric structure is lower by 776 meV. So there must be some other contribution that stabilizes the ferroelectric structure. Surprisingly, the remaining part of the energy which emerges from the short range coulomb interactions is the one that stabilizes the ferroelectric state.

7.2 Methodology

The electronic structure for $BaTiO_3$ is calculated within a plane-wave pseudo potential implementation of density functional theory in the VASP [8, 9] code. We consider the experimental structure for ferroelectric tetragonal $BaTiO_3$ and while the lattice parameters are kept fixed at the experimental values, the internal positions are relaxed. The same unit cell parameters are also taken for the paraelectric unit cell though the atoms are put at high symmetry positions. The total energy is calculated in each case using GGA-PW91 [10] potentials, using a plane waves basis set with kinetic energies less than 500 eV. A gamma-centered k-points mesh of $8 \times 8 \times 8$ k-points is used for the k-space integrations and the solution for the electronic structure is carried out self-consistently till the energy difference between successive steps is better than 10^{-5} eV. The total energy is decomposed into the band energy and the Hartree energy and we examined these contribution in various scenarios.

In order to understand the role of various distortions in stabilizing the ferroelectric phase, we have started with the paraelectric structure and displaced one or more atoms and evaluated the total energy as well as various contributions to it. The changes in the microscopic interaction strengths have been computed by mapping the ab-initio band structure to a tight-binding model which includes Ti d and O p states in the basis. The radial part of the basis function are determined by the maximally-localized

wannier functions [11–13].

7.3   Result and discussion
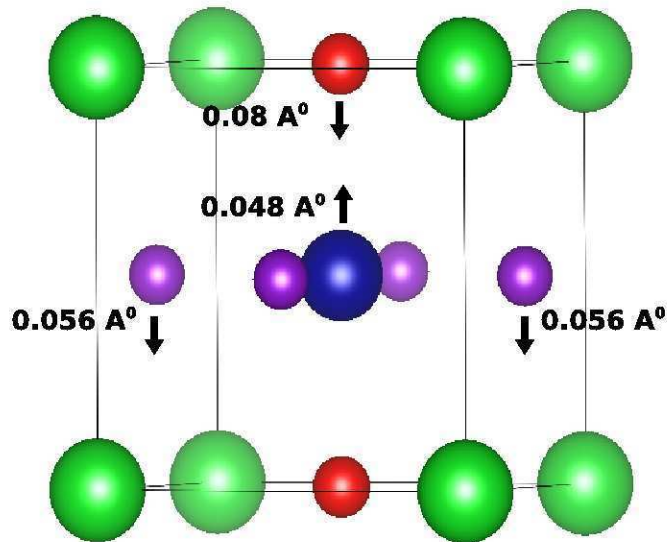
Figure 7.1 Comparison between ferroelectric structure and paraelectric structure has been shown. Displacement of various ions from its ideal position(paraelectric structure) is indicated. Green, blue, purple and red spheres indicates Ba, Ti, planner oxygens and apical oxygens respectively.

Ferroelectricity in the tetragonal phase of BaTiO₃ can be understood by examining the structure that is favored. Fixing the Ba position in the lattice, one finds that the Ti atom is displaced from its high symmetry position by 0.048 Å towards one of the apical oxygens. This decreases the Ti-O bondlength with one of the apical oxygens, while the other increases. The apical oxygens also moves towards the Ti atom by 0.08 Å. In addition one has a displacement of the in-plane oxygens by 0.056 Å in the direction opposite to the movement of the Ti atom. This leads to the setting up of a dipole moment per unit cell and the consequent observed ferroelectricity.
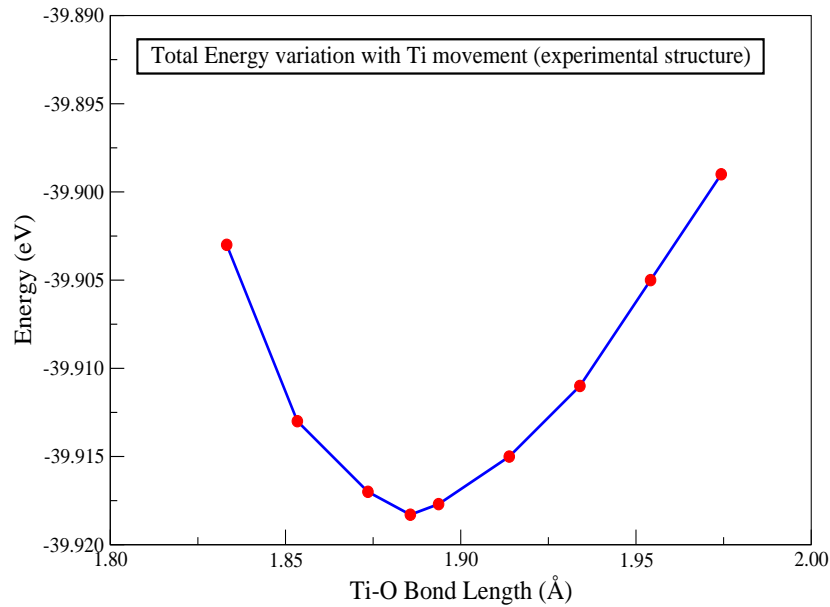
Figure 7.2 Total energy variation with Ti displacement in experimental structure.

A substantial component of the energy stabilizing the ferroelectric state is believed to come from the gain in band energy coming from a shorter Ti-O bond. This could be understood quite easily from a scaling of the relevant p-d hopping interaction strength with distance which varies as $\frac{1}{r^4}$ according to Harrison's scaling law. In order to examine this further, we have considered the ferroelectric structure of $BaTiO_3$ and moved the Ti atom, so as to vary the Ti-O bondlength. We have plotted the variation of the total energy with Ti movement in Fig.7.2. Indeed a minimum is found in the variation of the total energy as a function of the Ti-O bondlength. In order to examine this further, we have considered the paraelectric structure and displaced the Ti atom from its ideal position towards one of the apical oxygens. The variation of the total energy as a function of the Ti-O bondlength is shown in Fig.7.3. One finds an initial decrease of the energy and then a flattening off with no energy minimum founds, indicating the importance of the movement of the other atom also. Considering the movement of only the apical oxygen (Fig.7.4) one again finds no minima in the total energy variation. Further, unlike in
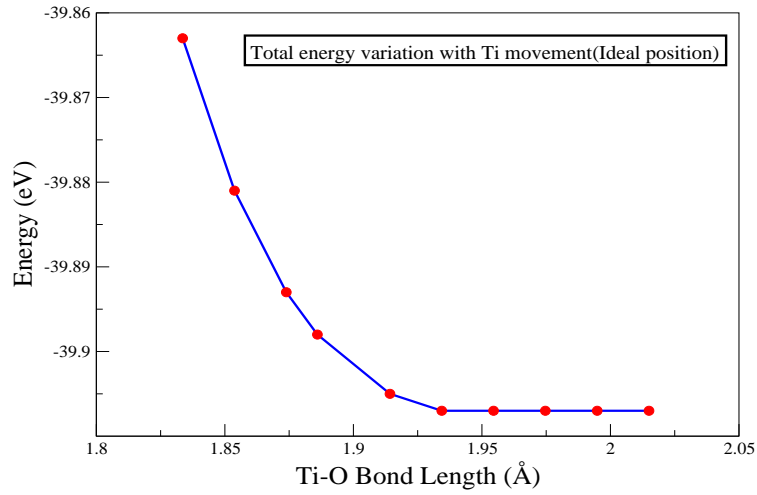
Figure 7.3 Total energy variation with Ti displacement in ideal structure.
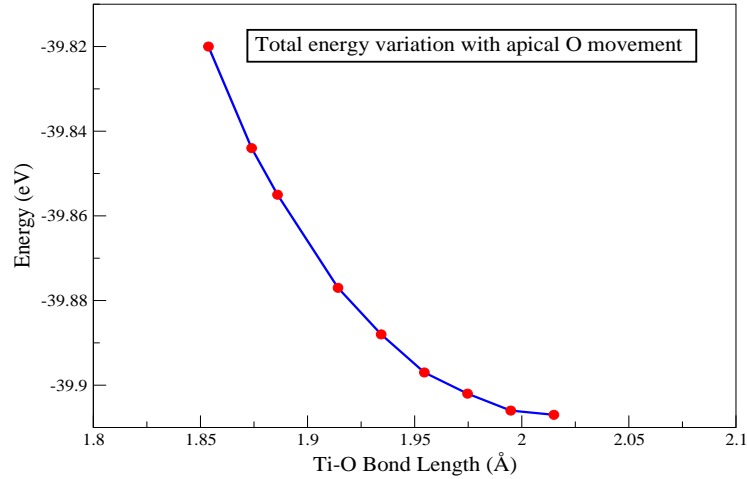
Figure 7.4 Total energy variation with apical oxygen movement in ideal structure.

the case of the Ti movement, one finds a more gradual decrease in the energy with no flattening off. The microscopic mechanism giving rise to ferroelectricity has been discussed in the literature [1, 7]

as arising from two dominant factors. The first was the gain in covalency arising from a shorter Ti-O bond. The second arose from long-range Coulomb interactions that arose from the presence of a non-vanishing dipole moment in the unit cell. Most approaches in the literature have used a form for this contribution to the energy that uses the Born effective charge rather than the bare charge in the expression for the dipole-dipole interaction. However, the born-effective charge represents the variation of the polarization with a displacement made in that direction. This can be related to the scaling of the hopping interactions with distance as the displacements are made, and is therefore related to the changes in covalency. The bare charge one should note are not drastically modified, while the Born effective charges could be as large as 7 for Ti^{4+}. We now go on to examine the changes in the Ewald energy associated with the displacements of Ti/O considered earlier. The Ewald energy contribution to the total energy for Ti displacement from its high symmetry position in the paraelectric structure has been plotted in Fig.7.5. This contribution is found to increase with the slightest Ti displacement from the high symmetry position. We examined various displacements of atoms as well as combinations of displacements and in every case we found an increase in the Ewald energy from the paraelectric structure. So in contrast to the belief that long range Coulomb interactions stabilize the ferroelectric structure, one finds that the trend is the opposite. While there is a gain in band energy of 340 meV in going from the paraelectric structure to the ferroelectric structure, the Ewald energy is found to increase by 1116 meV. So the role of the planar oxygens displacing in a direction opposite to that of the Ti displacement is not entirely clear. Further the fact that merely moving the Ti towards the apical oxygen or the apical oxygen towards the Ti atoms does not give us a minimum in the total energy with displacement. This indicates that the band energy gain alone is not enough to stabilize the ferroelectric structure.

In order to examine these aspects we examined the Hartree energy contribution in various scenarios - with just Ti displacement, with just apical oxygen displacement and the planar oxygen displacement in experimental structure. The variation of Hartree energies are shown in Fig.7.6, Fig.7.7 and Fig.7.8 respectively. In the first two cases, where we kept all other ions at ideal positions, we find that the Hartree energy increases as expected as the atoms come closer as a result of increased repulsion be-
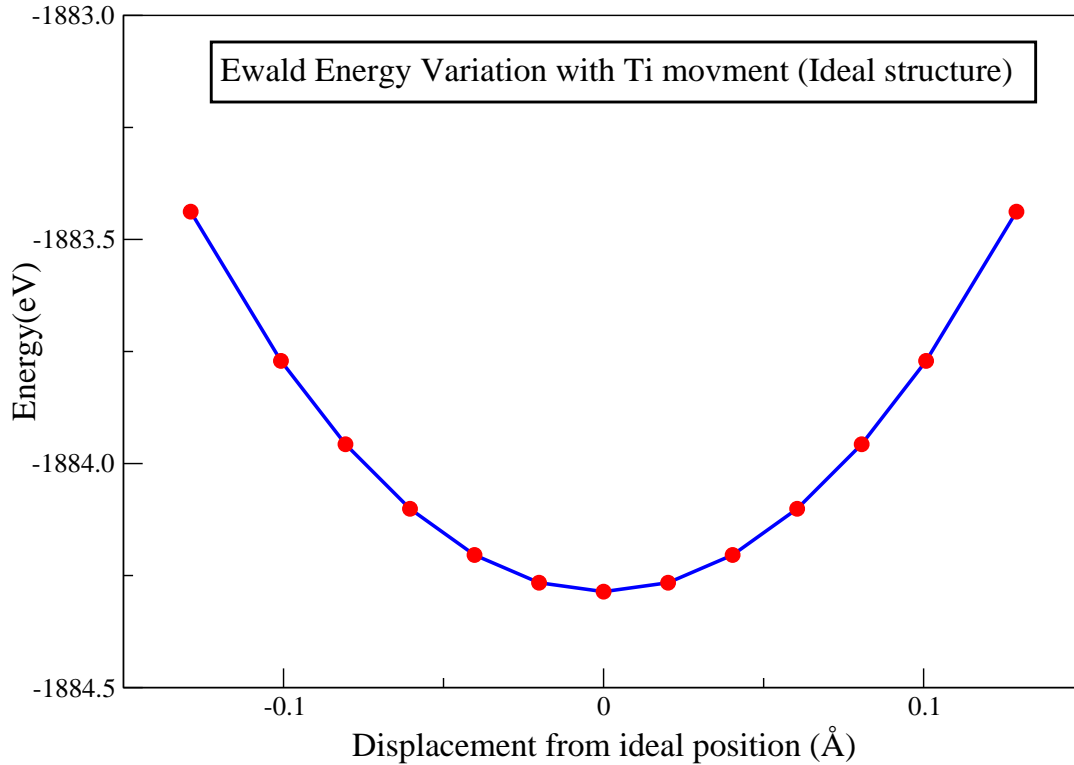
Figure 7.5 Ewald energy variation with Ti displacement in ideal structure.

tween the electrons on Ti and O. The last scenarios that we examined had all atoms at the experimental positions except the planner oxygens which were kept at the ideal positions. In this case we found that as the planar oxygens moved away from the Ti atoms, the Hartree contribution to the energy decreased. The large change in Hartree energy is partly because the O p orbitals are more extended and further that associated with four oxygens changes. So short ranged Coulomb interactions can be said to stabilize ferroelectricity.

In recent times a lot of effort has been placed towards the search for large polarization multiferroics. A route that has been realized so far has been considering band insulators such as $Ba_{1-x}Sr_xMnO_3$ [14]. This was proposed initially theoretically, and realized in experiments. A possible origin for the Mn off-
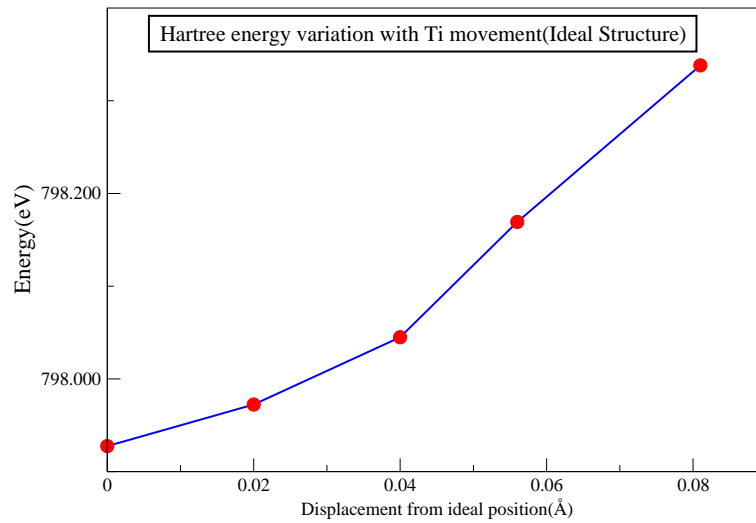
Figure 7.6 Hartree energy variation with only Ti displacement from ideal to experimental position.

centering was suggested to arise from the modified interactions of Mn with the planar oxygens [15]. In order to examine the role of various interactions in the case of $BaTiO_3$ we have set up a p-d tight
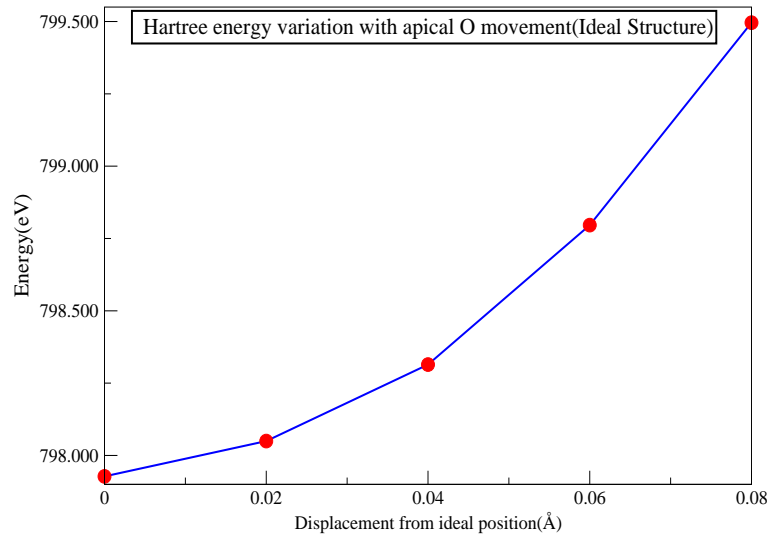
Figure 7.7 Hartree energy variation with only apical oxygen displacement from ideal to experimental position.
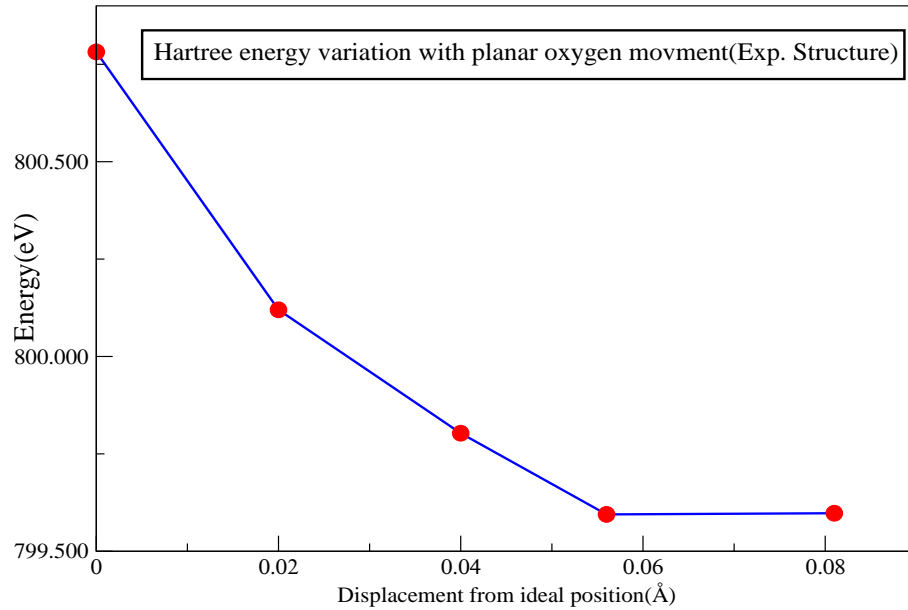
Figure 7.8 Hartree energy variation with planar oxygen displacement from ideal to experimental position(All other ions are at experimental position).

binding model for *BaTiO₃*. This model includes the d states on Ti and p states on oxygen and the tight binding parameters have been determined by mapping the ab-initio band structure to maximally localized Wannier functions.

The extracted on-site energies are given in Table.7.1. One finds an almost rigid band shift of the Ti d t_{2g} levels by 0.1 eV and an almost similar shift of the Ti d levels with e_g symmetry when one goes from the paraelectric structure to the ferroelectric structure. This could be understood as arising from the increased Ti-d contribution in the occupied levels arising from increased covalency in the ferroelectric structure. One finds a similar decrease in the energy of the orbitals which interact with the d states on the apical oxygens, while there is a small increase in the energies of the planar oxygens. The interaction strength between the Ti d and the O p orbitals can be discussed in terms of the Slater Koster parameters $pd\sigma$ and $pd\pi$. Using these parameters we set up a multiband Hubbard calculation for *BaTiO₃*. A mean field decoupling of the four fermions term is carried out. We then displace the Ti atoms toward an apical oxygens in the paraelectric structure, and examine the changes in the energy

Atom	Orbital	Onsite energies(in eV)	
		Ferroelectric structure	Ideal structure
Ti	d_{z^2}	6.046	5.975
	$d_{x^2-y^2}$	6.003	5.920
	d_{xy}	4.540	4.457
	d_{yz}	4.540	4.444
	d_{zx}	4.536	4.444
O(Apical)	p_x	0.977	1.077
	p_y	0.977	1.077
	p_z	0.569	0.624
O(In plane)	p_x	1.084	1.043
	p_y	0.627	0.589
	p_z	1.074	1.031

Table 7.1 On-site Energies for ideal and ferroelectric structure.

Energies(eV) with O-O interaction			
Ti-O bondlength(Å)	Ti movement	O(apical) movement	O(planner) movement
1.88(Exp)	7.897	11.447	14.720
1.92	8.088	11.397	14.999
1.96	8.206	11.365	15.174
2.01(Ideal)	8.259	11.351	8.259

Table 7.2 Band energies for Ti movement, O(apical) movement and O(planner) movement in ideal structure calculated using Hartree-Fock.

Energies(eV) without O-O interaction			
Displacement(Å)	Ti movement	O(apical) movement	O(planner) movement
0.00	8.402	8.402	8.402
0.02	8.352	8.339	8.414
0.04	8.239	8.197	8.444
0.06	8.056	7.969	8.467

Table 7.3 Band energies for Ti movement, O(apical) movement and O(planner) movement from their ideal positions in ideal structure calculated using Hartree-Fock.

which is related to the band energy obtained from the ab-initio calculations. The variation in energy with the displacement has been shown in Table.7.2. Inducing just the interactions between the Ti and the apical oxygens, one finds a decrease of 532 meV in band energy with the Ti off-centering in going from the Ti-O bondlengths in the paraelectric structure to that found in the ferroelectric structure. This can be understood as the dominant hybridization interactions involve the d orbitals with t_{2g} symmetry on Ti. Switching off the Ti and apical oxygen interactions we found a increase of energy by 96 meV. This is due to slightly reduced hybridization between Ti and planar oxygen. This suggests the interaction with the apical oxygens is on the significantly enhanced with the off-centering, and so the mechanism of the band energy stabilization of the Ti off-centering is captured microscopically.

To understand the role of Ti and apical oxygen interactions in band energy better, we have switched

off the oxygen oxygen interactions and moved Ti, apical oxygen, planar oxygen from their ideal positions. The energies are shown in Table.7.3. Results suggests that the interaction between Ti and apical oxygens are important in stabilizing the ferroelectric phase.

In this chapter we have analysis the role of displacements of various ions in $BaTiO_3$. We found that the band energy as well as Hartree energy contribute in stabilization of ferroelectric state.

Bibliography

[1] Cochran, W. (1960). Adu. Phys., 9, 387.

[2] Cohen, R. E. (1992). Nature, 358, 136.

[3] Zhong, W., Vanderbilt, D. and Rabe, K. M. (1995). Phys. Rev. B, 52, 6301.

[4] R. E. Cohen, H. Krakauer Phy Rev B 42,number 10, 6417

[5] R.E. Cohen ;Journal of Physics and Chemistry of Solids 61 (2000) 139âĂŞ146

[6] Ph. Ghosez, X. Gonze and J.P. Michenaud; Europhys. Lett., 33 (9), pp. 713-718 (1996)

[7] Gonze X., Charlier J.-C., Allan D. C. and Teter M. P., Phys. Rev. B, 50 (1994) 13035

[8] G. Kresse, and J. Furthm*ü*ller, Phys. Rev. B. **54**, 11169 (1996); G. Kresse, and J. Furthm*ü*ller, Comput. Mat. Sci. **6**, 15 (1996).

[9] G. Kresse, and J. Joubert,Phys. Rev. B **59**, 1758 (1999).

[10] J. P. Perdew, Y. Wang Phys. Rev. B. **45**, 13244(1992)

[11] A. A. Mostofi, J. R. Yates, Y.-S. Lee, I. Souza, D. Vanderbilt and N. Marzari, wannier90: A Tool for Obtaining Maximally-Localised Wannier Functions, Comput. Phys. Commun., 178, 685 (2008)

[12] N. Marzari and D. Vanderbilt, Phys. Rev. B 56, 12847 (1997)

[13] Maximally localized Wannier functions for entangled energy bands, I. Souza, N. Marzari and D. Vanderbilt, Phys. Rev. B 65, 035109 (2001)

[14] H. Sakai et. al., Phys. Rev. Lett. 107, 137601 (2011).

[15] Gianluca Giovannetti, Sanjeev Kumar, Carmine Ortix, Massimo Capone, and Jeroen van den Brink. arxiv:1202.2069v1 [cond-mat.mtrl-sci]